

# The Role of Defects During Precipitate Growth in a Ni-45wt% Cr Alloy

by

Jhewn-Kuang Chen

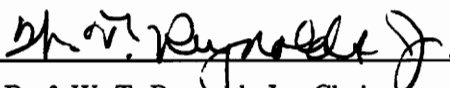
Dissertation submitted to the faculty of the  
Virginia Polytechnic Institute and State University  
in partial fulfillment of the requirements for the degree of

DOCTOR OF PHILOSOPHY

in

Materials Engineering Science

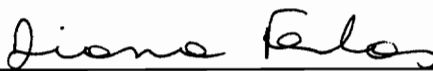
APPROVED:



Prof. W. T. Reynolds Jr., Chairman



Prof. S. B. Desu



Prof. D. Farkas



Prof. G. V. Gibbs (MSE/GEOL)



Prof. S. L. Kampe



Prof. J. M. Howe (Univ. Virginia)

September, 1995

Blacksburg, Virginia

**Keywords:** Precipitate morphology, Interfacial structure, Habit plane, Lattice  
correspondence, Atomic matching

C.2

2D  
5655  
V850  
1995  
C445  
C.2

# The Role of Defects During Precipitate Growth in a Ni-45wt% Cr Alloy

by

Jhewn-Kuang Chen

Committee Chairman: Prof. W. T. Reynolds Jr.

Materials Engineering Science Program

## (ABSTRACT)

The defect structure, atomic structure, and energy of the interphase boundaries between an fcc matrix and a lath-shaped bcc precipitate in Ni-45wt% Cr were investigated. The interfacial structure on the side facet of the precipitate consists of regular structural ledges and misfit dislocations. No regular defect structure can be found on the habit plane, or broad face, of the lath except for atomic-scale structural ledges. High resolution electron microscopy (HREM) observations show the  $(\bar{1}\bar{2}1)_f$  habit plane is coherent and is a good matching interface. Based upon conventional transmission electron microscopy (TEM) observations, the orientation of the habit plane results from advancing growth ledges on the conjugate plane of the Kurdjumov-Sachs orientation relationship. Using embedded atom method (EAM) simulations, the interfacial energy of the  $(\bar{1}\bar{2}1)_f$  habit plane is calculated and the simulated interphase structure is compared with the HREM observations. The simulated interface represents a major portion of the observed interface. The calculated interfacial energy of the  $(\bar{1}\bar{2}1)_f$  habit plane is  $210 \text{ mJ/m}^2$ , lower than typical grain boundary energies indicating this habit plane is a low-energy interphase boundary. A non-Bain lattice correspondence is identified and employed to predict the  $(\bar{1}\bar{2}1)_f$  habit plane successfully, although a Bain correspondence is more successful at predicting the elongation direction for the precipitate. Geometric matching is proposed to be responsible for determining the orientation of the precipitate habit plane and the growth direction. Lattice

correspondence-based approaches such as the invariant line model and the phenomenological theory of martensitic crystallography can mimic aspects of geometric matching, but they do not accurately reflect the transformation mechanism during precipitation of bcc laths from an fcc parent.

## ACKNOWLEDGEMENTS

When I was a undergraduate student studying physical metallurgy, I used to imagine atoms as a bunch of solid balls. The boundaries between different crystals develop facets when the atoms on either side of the boundaries match well. Being an atomic matching believer, I was not introduced to a more scientific interpretation of this concept until I came to Virginia Tech and started to work with Prof. W. T. Reynolds Jr. I thank Prof. Reynolds for his mentorship. He has not only helped me pursue my youthful dreams, but he also impressed and affected me by his dedication to science. His trust and confidence to a team that knows how to work together and work hard has provided some of the most important fertilizers to an excellent research group. Over the years in the phase transformation group, I also have had the pleasure of working with an outstanding peer, Dr. Gang Chen. Without his help, I could not have become an electron microscopist.

The scrupulous reviews of this manuscript by Prof. G. V. Gibbs, Prof. D. Farkas, Prof. J. M. Howe, Prof. S. B. Desu, Prof. S. L. Kampe, and Prof. A. O. Aning are graciously appreciated. I am also indebted to some of the most renowned workers in the related fields. Among them are Prof. G. C. Weatherly and Dr. C. P. Luo of McMaster University (neither of whom I have met in person) for providing Dr. Luo's dissertation on interfacial structure of precipitates in Ni-Cr, my grand-advisor Prof. H. I. Aaronson of Naval Research Laboratory for enlightening comments that influenced the direction of later parts of my thesis, Prof. D. Farkas for developing Cr potentials and for her help with the embedded atom method simulations used in Chapter 3, Prof. J. M. Howe of University of

Virginia for many discussions and help with conventional and high resolution transmission electron microscopy, Prof. C. W. Spencer for his encouragement during the Ag–Ga pearlite project, and Prof. T. Furuhashi of Kyoto University for generously sharing his thoughts and micrographs on precipitation in Ni–Cr before they were published. The financial support of National Science Foundation through grant DMR93–03518 is also gratefully acknowledged.

Gratitude should be extended as well to my friends and fellow students who gave me their friendship and delightfulness during my years at Virginia Tech. In particular, Prof. Reynolds' wife, Mariko Reynolds, Mr. Qiang Liang, Mr. G. Levon Fattal, Ms. Jan Doran, Mr. Harry Dudley, Mr. Chris Jones, Ms. Thobeka Pete, Ms. Batsirai Mutasa, Mr. Dave Teter, Dr. Yiwen Mou, Dr. Prabodh L. Ratnaparkhi, and Mr. Michael M. Y. Tsai are among the many to whom I owe my thanks for their help.

Finally, in addition to those mentioned, I wish to thank my family in Taiwan who supported me spiritually over the years. The honor of this accomplishment belongs to them.

# TABLE OF CONTENTS

<b>1</b>	<b>Introduction</b>	<b>1</b>
<b>2</b>	<b>Interfacial Structure and Growth Mechanisms of Lath-Shaped Precipitates in Ni-45wt% Cr</b>	<b>6</b>
2.1	Introduction . . . . .	6
2.2	Procedure . . . . .	7
2.2.1	Sample Preparation . . . . .	7
2.2.2	TEM Analysis . . . . .	8
2.3	Results . . . . .	11
2.3.1	Basic Parameters: Habit Plane and Side Facet . . . . .	11
2.3.2	Shapes of Precipitates and Ledges . . . . .	13
2.3.3	Observations of Defect Structure . . . . .	13
2.4	Discussion . . . . .	25
2.4.1	Atomic Density Difference in Between Matrix and Precipitate Crystals	25
2.4.2	Formation of $(1\bar{1}1)_f$ Slip-related Defects on The Habit Plane . . . . .	28
2.4.3	Stacking Faults and Formation of Ledges . . . . .	32
2.4.4	Defects Observed on The Side Facet . . . . .	33
2.5	Conclusion . . . . .	34
<b>3</b>	<b>Atomistic Simulation of Fcc:Bcc Interface in Ni-Cr Alloys</b>	<b>36</b>
3.1	Introduction . . . . .	36

## CONTENTS

3.2	Procedure and Results . . . . .	37
3.2.1	Interatomic Potentials for Simulations in Ni–Cr Alloys . . . . .	37
3.2.2	Configuration of the Simulation Block . . . . .	42
3.2.3	Evaluation of Interface and Strain Energy . . . . .	47
3.3	Discussion . . . . .	51
3.4	Conclusions . . . . .	57
<b>4</b>	<b>Determination of the Best-Matching Direction and Plane in Partially-Coherent Interfaces</b> . . . . .	<b>59</b>
4.1	Introduction . . . . .	59
4.2	Procedure . . . . .	60
4.3	Bcc/9R interfaces . . . . .	63
4.4	Discussion . . . . .	64
4.5	Summary . . . . .	66
<b>5</b>	<b>The Role of Atomic Matching and Lattice Correspondences in the Selection of Habit Planes</b> . . . . .	<b>68</b>
5.1	Introduction . . . . .	68
5.2	Procedure and Results . . . . .	70
5.2.1	Derivation of the Transformation Matrix . . . . .	71
5.2.2	Best-Matching Direction and Best-Matching Plane . . . . .	72
5.3	Discussion . . . . .	76
5.3.1	Comparison of the Bain Correspondence and Correspondence II . . . . .	76
5.3.2	Diffusional and Martensitic Transformations . . . . .	81
5.3.3	Summarized Procedure for the Derivation of the Smallest Near-Coincident Site Lattice Interface . . . . .	83

*CONTENTS*

5.4	Conclusions . . . . .	84
<b>6</b>	<b>Summary</b>	<b>86</b>
<b>A</b>	<b>Derivation of Crystallographic Orientation Relation with Double Tilt Holder</b>	<b>97</b>
<b>B</b>	<b>Derivation of Lattice Correspondences</b>	<b>100</b>
<b>C</b>	<b>Program List and Selected Computer Programs</b>	<b>105</b>
C.1	List of programs . . . . .	105
C.2	Codes . . . . .	112

## LIST OF FIGURES

2.1	(a) Cross section of a bcc precipitate formed by aging Ni-45wt% Cr at 950°C for 4200 seconds, (b) a schematic of the precipitate lath cut by the foil nearly perpendicular to the elongated direction. The arrows indicate the directions of ledge growth migration. (c) The corresponding diffraction pattern of the precipitate in this orientation ( $[\bar{1}01]_f \parallel [\bar{1}\bar{1}1]_b$ ), and (d) the indices for (c). . . . .	9
2.2	The poles of the habit plane, the side facet and the line direction of dislocations lying in the habit plane. . . . .	12
2.3	Two-beam bright field (a) and weak-beam dark field (b) micrographs of the $(\bar{1}\bar{2}1)_f$ habit plane using $\mathbf{g} = 111_f$ . (c) and (d) are two-beam bright field and weak-beam dark field micrographs of the same interface using $\mathbf{g} = 1\bar{1}1_f$ . “L” represents ledges . . . . .	15
2.4	(a) and (b): Bright field and WBDF microstructure of habit plane using $\mathbf{g} = 1\bar{1}1_f$ . (c) and (d): Bright field and WBDF microstructure using $\mathbf{g} = 111_f$ . “SF” represents stacking faults. . . . .	18
2.5	(a) and (b) show the side facet structures using WBDF technique. (c) Schematic of atomic structure of the $(313)_f$ side facet. . . . .	21
2.6	(a) Irregular defects on the habit plane. (b) Schematic of all defects observed on the habit plane and side facet and their orientations. . . . .	24
2.7	(a) HREM observation of the $(1\bar{2}1)_f$ habit plane. (b) Calculated atomic structure of the habit plane for lattice parameter ratio $a_f/a_b = 1.255$ . . . . .	26

LIST OF FIGURES

2.8	HREM observation of $[111]_f$ Shockley faults at the $(\bar{1}\bar{2}1)_f$ habit plane. . .	27
2.9	A 1.1 nm growth ledge in the $(\bar{1}\bar{2}1)_f$ habit plane. Interface matching on the left and the right sides of the ledge is essentially the same. . . . .	31
3.1	Effective pair potentials ( $\phi_{\text{Ni}[1]}$ , $\phi_{\text{Cr}[2]}$ and $\phi_{\text{NiCr}}$ ) for Ni–Cr alloys employed in the present study. . . . .	38
3.2	Dependence of the lattice parameters on composition of fcc alloys obtained from the simulations (represented by dots in the plot). The solid line is Equation 3.2. . . . .	43
3.3	Change of fcc and bcc cohesive energy versus composition. . . . .	44
3.4	(a) High resolution electron microscopy image of the $(\bar{1}\bar{2}1)_f$ habit plane of a bcc precipitate formed during aging of Ni–45wt%Cr at 950°C. (b) Atomic structure of the simulated interface. . . . .	45
3.5	Ni–Cr phase diagram [3]. . . . .	48
3.6	The linear relationships between excess energy and the thickness of bcc crystal (expressed as the number of 42 atom modules) in the simulation block for (a) fcc crystals containing 0 at% Cr; the intercept of the line at zero bcc thickness corresponds to interface energy of 216 mJ/m <sup>2</sup> and the slope corresponds to a strain energy of $3.9 \times 10^7$ J/m <sup>3</sup> , and (b) fcc crystals containing 25 at% Cr, the interface energy and strain energy are 211 mJ/m <sup>2</sup> and $3.2 \times 10^7$ J/m <sup>3</sup> , respectively. . . . .	50

*LIST OF FIGURES*

3.7 The strain energy of the bcc crystal as a function of the Cr concentration in the fcc crystals. The solid line represents a fitted curve for strain energy determined from the simulations. The dashed line represents the analytical strain energy calculated from elasticity using homogeneous coherency strains in the initial simulation block. . . . . 52

3.8 The change of interface energy with the compositions of fcc crystals. . . . . 53

3.9 Two views of: (a) the relaxed structure of a simulation block with pure Ni fcc crystals and pure Cr bcc crystals, and (b) the relaxation structure of a simulation block when the composition of the fcc crystals is 25 at% Cr. Different shapes (square, triangle, and circles) are used to represent atoms on different planes parallel to the paper ( $(20\bar{2})_f$  and  $(22\bar{2})_b$ ). The final positions of Ni and Cr atoms are represented by empty and filled shapes, respectively. The relative relaxations (represented by lines attached to the atoms) are enlarged 10 times to show their directions. . . . . 54

4.1 Representation quadric for the matrix M. . . . . 62

5.1 The representative ellipsoids for (a) the Bain correspondence and (b) correspondence II (neither ellipsoid is drawn to scale.) . . . . . 75

5.2 The sketch is a top view of one atomic layer of  $(1\bar{2}1)_f$ , and the outlined rectangle describes the  $\Sigma 3$  near-CSL. The filled circles represent fcc atoms and the open ones are bcc atoms. The vectors  $d_1$  and  $d_2$  (not drawn but connecting the indicated pairs of atoms) are the shuffle vectors required for the two atoms inside the unit cell of correspondence II. Their magnitudes are  $[\bar{0}.18 \bar{0}.17 0.15]_f$  and  $[0.15 0.15 \bar{0}.20]_f$ , respectively. . . . . 79

*LIST OF FIGURES*

- B.1 A schematic of lattice correspondence II. The bcc crystal (top) and fcc crystal (bottom) are in the Kurdjumov-Sachs orientation relationship and the  $[\bar{1}01]_f$  and  $[\bar{1}\bar{1}1]_b$  directions are perpendicular to the plane of the projection. Two of the three sets of correspondence vectors are shown:  $[\bar{1}54]_b$  and  $[333]_f$ ;  $[010]_b$  and  $[\frac{1}{2}\frac{1}{2}0]_f$ ; the third set is perpendicular to the projection:  $[\frac{\bar{1}}{2}\frac{\bar{1}}{2}\frac{1}{2}]_b$  and  $[\frac{\bar{1}}{2}0\frac{1}{2}]_f$ . . . . . 103

## LIST OF TABLES

3.1	Experimental and calculated results of elastic constants for pure bcc Cr (units in GPa). . . . .	41
3.2	Parameters obtained for the NiCr mixed interaction potential (Equation 3.1.) $A$ is dimensionless and the distances $a$ through $f$ are in nm. . . . .	41
4.1	Calculation and experimental results on different interfaces . . . . .	65
5.1	Comparison of eigenvalues and eigenvectors for Bain correspondence and lattice correspondence II. Eigenvector 1 represents the best-matching direction, and eigenvector 3 is the best-matching plane normal in each correspondence.	74

# Chapter 1

## Introduction

The morphology of precipitates is an important factor that controls the mechanical and physical properties of alloys. In many alloy systems, precipitates adopt a rod-shape [4, 5, 6, 7], plate-shape [8, 9, 10, 11, 12], or lath-shape [13, 14, 15]. In these cases, the parameters needed to specify precipitate morphology are the direction of elongation, the broad face orientation (habit plane), and the aspect ratio of the precipitate. An understanding of these factors thus is an important area that may eventually enable materials engineers to manipulate precipitate morphology. Though precipitation is a diffusional process, theories for diffusionless martensitic transformations have been borrowed to explain some of the phenomena associated with precipitation [16, 17]. To explore the implications of this apparent dichotomy, such theories for two major transformation mechanisms [18, 19], martensitic and diffusional precipitation, are introduced briefly here [20].

Following Wechsler, Lieberman and Read [21] and Bowles and Mackenzie [22, 23, 24], the phenomenological theory of martensitic crystallography (PTMC) describes a martensitic transformation by a homogeneous strain. This strain is generally described in terms of two components: one that deforms the parent (or matrix) crystal lattice to the product lattice and a shear (lattice invariant deformation) that produces an invariant, or macroscopically undistorted, plane between the parent and product phases. The invariant plane is the habit plane on which martensitic plates or laths develop. The homogeneous deformation implies an atomic correspondence between the parent and product phases, i.e., each atom

undergoes the same strain [18]. Within the constraints of the atomic correspondence, atoms migrate in a military fashion and the transformation proceeds athermally, and as Wayman has noted [25], there is no change in composition or order. As long as the shear direction and lattice correspondence are known, the martensite habit plane, orientation relationship between parent and product phases, and the magnitude of shear can be calculated using the PTMC. Except for the magnitude of shear, these parameters can be checked by experimental observations [26, 27]. However, it is important to note that there is no simple procedure to derive either the shear direction or lattice correspondence required by the PTMC. In some cases, especially for ferrous martensite with a  $\{252\}_f$  habit plane [28], these parameters have been based upon educated guesses or trial and error [29]. For the most commonly considered fcc-bct martensitic transformation in ferrous alloys, an atomic correspondence identified by Bain [30] is generally assumed [31, 25].

During diffusional precipitation transformations, atomic rearrangements not only have to change the crystal structure, but they also have to redistribute solute and solvent atoms. This requires uncoordinated motion of individual atoms by thermally activated diffusional jumps. For this case, Aaronson proposed a general theory of precipitate morphology [32, 33] that explained precipitate shape during growth in terms of the orientation dependence of the boundary. Boundary orientations with high mobility were suggested to grow out leaving behind facets composed of lower mobility, coherent or partially coherent boundaries. Good matching, which means atoms on either side of the boundary lie close to the positions they would occupy if the boundary were not present, is implicit at these coherent and partially coherent boundaries.

Transmission electron microscopy (TEM) observations and computer simulations made during the '70 and '80s for precipitate habit planes in ferrous, Al, and Cu alloys [4, 11, 34, 35, 36, 37] demonstrated that the interphase boundaries were indeed good matching. The

predominant growth direction of precipitates (the elongated directions of laths and rods and radial directions of plates) was also shown by Bywater and Dyson [38] and Dahmen et al. [17, 39] to include a good matching direction. Dahmen and his coworkers used invariant line theory [17, 40, 39] to predict the perfect matching direction between parent and product phases and succeeded in predicting the growth direction of precipitates in various alloys [7, 13, 15]. Like the PTMC, a lattice site correspondence is required to apply the invariant line theory [41]. However the correspondence only applies to lattice sites rather than individual atoms in the case of precipitation reactions to allow the compositions of the parent phase and the precipitate to differ.

One of the missing pieces in understanding the formation of precipitate morphology is the prediction of good matching boundary orientations, i.e., the precipitate habit plane. The invariant line theory only yields a single good matching direction and a second criterion is needed to predict a habit plane. There are several criteria [42, 43, 44] for this purpose, but their success is very limited especially for the fcc/bcc system. Part of the problem in habit plane prediction is whether or not atomic matching can be represented by a lattice site correspondence. It is the goal of this dissertation to propose a way for predicting the fcc/bcc precipitate habit plane based upon the atomic mechanisms implied by the defect and atomic structures observed at an interface.

The discussions are made from four different points of view: interfacial structure (Chapter 2), interfacial energy (Chapter 3), the best-matching direction and plane derivation (Chapter 4), and lattice correspondence and atomic matching (Chapter 5). These chapters are prepared as papers for the open literature. They thus contain the basic elements required by technical papers including introduction, procedure, results, discussion, and conclusions sections. References to the chapters are made to the papers listed as follows: Chapter 2 is Reference [45], Chapter 3 is Reference [46], Chapter 4 is Reference [47], Chapter 5 is

Reference [48], Appendix A corresponds to the Appendix section in Reference [45], and Appendix B is the Appendix for Reference [48].

In Chapter 2, the interfacial structure and defects associated with the growth or precipitates in Ni-45wt% Cr alloy are described. The chapter builds upon the earlier work of Luo and Weatherly [13, 49] on the same alloy. A large number of precipitates and defects are analyzed to determine the statistical importance of the defects observed and their role in the precipitate growth process.

Chapter 3 employs atomistic simulations to estimate the interfacial energy of the precipitate habit plane in Ni-Cr to confirm that the good matching boundary is a low energy interface. The boundary structure used in the embedded atom method simulations is also compared for consistence with high resolution electron microscopy (HREM) observations [45] on the precipitate habit plane.

Chapter 4 proposes an analytical method to determine the best-matching direction and plane based upon a specified lattice correspondence. The method employs an eigenvalue technique to find the least and the largest misfit directions between two crystal structures arranged in an arbitrary orientation relationship. Results of evaluations using this method are compared with the growth directions and habit planes observed in precipitation reactions between bcc/9R, fcc/bcc, and bcc/hcp crystal structures.

Chapter 5 demonstrates a procedure for selecting precipitate facet planes and important lattice correspondences. The approach is based upon finding interphase boundaries with a high density of near-coincident sites. Such near coincident site boundaries are identified by analyzing computer-generated lattice correspondences. The questions are addressed of whether lattice correspondences other than the Bain correspondence [30] are appropriate and whether a correspondence obtains at all between the fcc and bcc phases in Ni-Cr.

Appendix A describes a tool developed to obtain crystallographic information from TEM

diffraction data. The relation between a TEM double-tilt specimen holder and crystallographic orientation is derived. Using the angle readings from a double tilt holder and more than three diffraction patterns, a translation matrix between the crystal coordinate system and a lab frame of reference can be obtained. The primary application of this tool is to help unambiguously index the crystallographic orientations for trace analysis and for orientation relationship determinations used in Chapter 2.

In Appendix B, a procedure is described following Jaswon and Wheeler [31] for deriving the lattice correspondences that meet the least deformation criterion [25]. The procedure is implemented in a computer program and used to analyze  $\sim 2000$  sets of correspondences in Chapter 5.

A number of computer programs were developed during the course of this thesis. The programs consist of more than 10,000 lines of C, FORTRAN, or Mathematica [50] code. Appendix C provides a short description of each program. Four of the programs are included with the dissertation: a crystallographic analysis tool box (*VectorAnalysis.ma* used in Chapter 2), the best-matching direction and plane determination procedures (*BMDBMP.ma* used in Chapter 4 and 5), an algorithm for fcc/bcc lattice correspondence determinations (*CORRfinder.ma* used in Chapter 5), and the diffraction zone finder program for general crystal structure diffraction pattern indexing (*ZoneFinder.ma* used in Chapter 2 and Reference [51, 52]).

## Chapter 2

# Interfacial Structure and Growth Mechanisms of Lath-Shaped Precipitates in Ni-45wt% Cr

### 2.1 Introduction

The fcc/bcc interface is one of the most important interphase boundaries in metallic alloys [32]. It plays an important role in ferrous phase transformations and has been studied in steels [53, 54], Ni-Cr [13, 49], Fe-Cu [6, 7], Cu-Cr [4, 15], and dual phase stainless steel [55]. Bcc laths generally precipitate from an fcc matrix in all these systems. There are many similarities among the crystallographic characteristics of the precipitates in these systems, such as the growth direction, habit plane, and morphology.

The bcc precipitates hold an exact or near Kurdjumov-Sachs orientation relationship (K-S OR) [56] with the matrix fcc crystals<sup>1</sup>, and the ratio of the fcc and bcc lattice parameters,  $a_f/a_b$ , falls between 1.25 and 1.26 in these alloys [6, 15, 55, 57, 58]. The precipitates elongate along a direction  $\sim 5.5^\circ$  from  $[\bar{1}01]_f$ , the conjugate direction of the K-S OR. This elongated or predominant growth direction has been predicted successfully by the invariant line theory developed of Dahmen and coworkers [17, 39]. Since the precipitates have a lath-shape, their broad face or habit plane is parallel to this growth direction. The precipitate habit plane is a

---

<sup>1</sup> The indexing of crystallographic directions for the precipitates depends upon the choice of orientation relationship variant. The K-S variant used throughout this study is that used by Luo and Weatherly [13]:

$$(\bar{1}\bar{1}1)_f \parallel (101)_b \quad \text{and} \quad [\bar{1}01]_f \parallel [\bar{1}\bar{1}1]_b$$

where the “*f*” and “*b*” subscripts indicate coordinates for the fcc and bcc lattices, respectively.

$(\bar{1}\bar{2}1)_f$  plane tilted  $\sim 19^\circ$  from the parallel conjugate planes of the orientation relationship.

Among these alloys, Ni-Cr is the most extensively characterized. Detailed studies of the interfacial structure of bcc precipitates in Ni-45 wt%Cr have been reported by Luo and Weatherly [13, 49] and Furuhashi et al. [59], and the kinetics of growth ledge formation have been measured by Chen and Reynolds [60]. The current study employs this alloy system to characterize defects in the fcc matrix associated with the precipitate growth process. The defects, which include dislocations and stacking faults, are related to the fcc/bcc interfacial structure and the precipitate growth mechanism. An attempt is also made to assess the variation in the type of defects and the interfacial structure from one precipitate to another.

## 2.2 Procedure

### 2.2.1 Sample Preparation

A 400 gram ingot of the Ni-45wt%Cr alloy was made by arc-melting 99.99% pure Ni and Cr metals. A section of  $10 \times 10 \times 100$  mm was cut from the ingot, encapsulated in a quartz capsule, evacuated to a pressure of  $< 10^{-5}$  torr, and sealed under  $\frac{1}{3}$  atm argon. A titanium powder compact was included within the capsule to getter oxygen. Homogenization was then performed at  $1300^\circ\text{C}$  for three days before quenching into ice brine. The homogenized material was cold rolled to 0.5 mm thick coupons. These coupons were again evacuated, flushed with argon, and resealed in a quartz capsule under  $\frac{1}{3}$  atm argon atmosphere. The coupons were solutionized for 4 hours at  $1300^\circ\text{C}$  and quenched in ice brine. The samples were then aged at  $950^\circ\text{C}$  for 4200 seconds in evacuated capsules. At this aging time, precipitates were still in the growth stage and have a uniform shape [60].

TEM foils were prepared by mechanically grinding the aged samples to approximately  $100 \mu\text{m}$  and punching 3 mm diameter disks. The disks were jet polished with a solution of

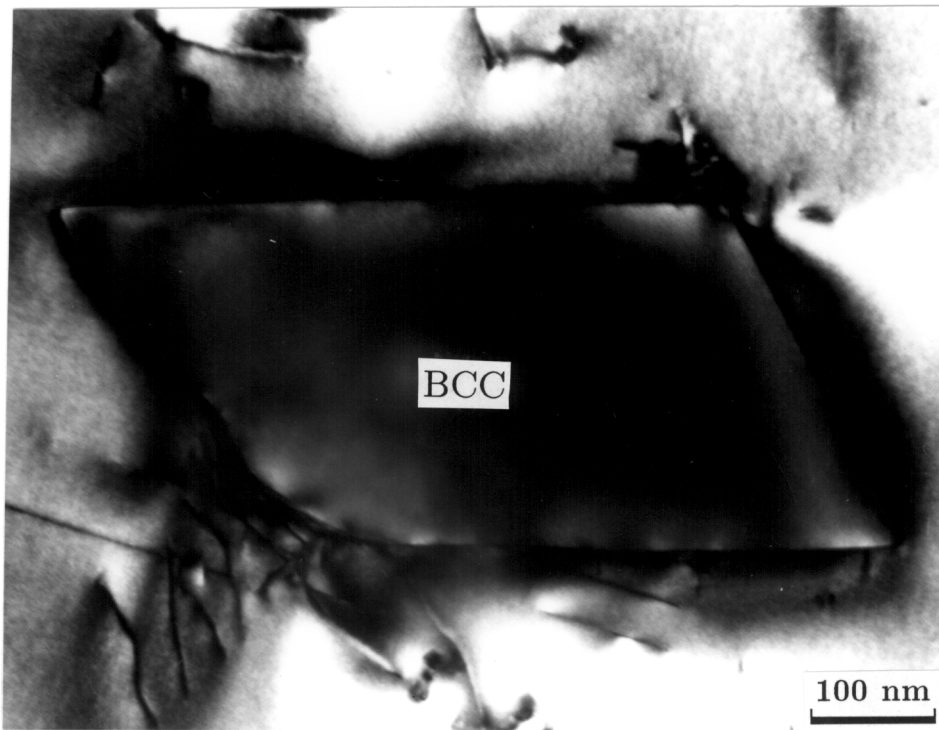
7% perchloric acid, 11% Butyl-Cellosolve, 31% 1-Butanol, and 51% Ethanol [61], at  $-30^{\circ}\text{C}$ , and 150–200 V [60]. The thin foils were examined using a Philips EM420 transmission electron microscope (TEM) operated at 120 kV and a JEOL 4000X operated at 400 kV.

### 2.2.2 TEM Analysis

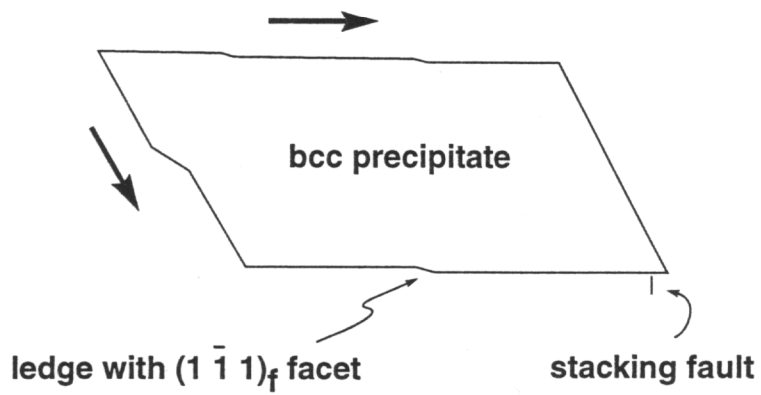
The long axis of the precipitates lies close to the conjugate  $[\bar{1}01]_f$  and  $[\bar{1}\bar{1}1]_b$  directions, so a precipitate sectioned by the foil perpendicular to their long axis (Figure 2.1) produces diffraction patterns that reveal the K–S OR directly. The zone axis of such patterns corresponds to the conjugate directions of the K–S OR and the patterns contain  $\mathbf{g}$  vectors of the conjugate planes ( $(\bar{1}\bar{1}1)_f$  and  $(101)_b$ , see Figure 2.1(c)-(d)). Because both the habit plane and side facet of the precipitates are almost parallel to the elongated direction, these boundaries are nearly edge-on for precipitates in cross section (Figure 2.1(a)). The sample preparation procedure produced textured foils with foil normals close to a  $\langle 110 \rangle_f$  direction, so it was relatively easy to obtain edge-on precipitates.

Each precipitate was indexed individually following the chosen K–S OR variant. When the parallel  $[\bar{1}01]_f$  ( $\parallel [\bar{1}\bar{1}1]_f$ ),  $[1\bar{1}1]_f$  ( $\parallel [101]_f$ ), or  $[121]_f$  ( $\parallel [\bar{1}21]_f$ ) zones could be obtained within the specimen holder's range of tilt, the indexing was straightforward since two sets of patterns from fcc and bcc crystals could be indexed. In cases where these parallel zones were unreachable, the tilt angle readings corresponding to each observed zone were recorded. A more detailed description of the procedure is provided in Appendix A. The locations of Kikuchi lines from the fcc and bcc phases were then compared with the corresponding stereographic projections arranged in the chosen variant of the K–S OR to index the zone axis. A set of unique indices was accordingly assigned.

For trace analysis, at least three non-coplanar zones were used. Up to nine different diffracting  $\mathbf{g}$  vectors were used to analyze the defects in each precipitate using the  $\mathbf{g} \cdot \mathbf{b} = 0$

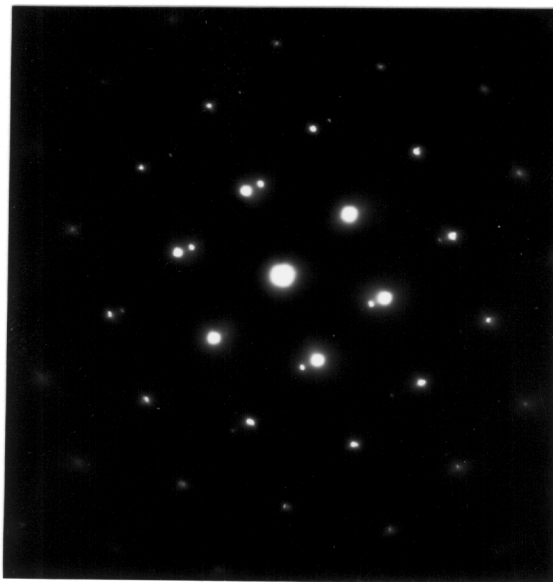


(a)

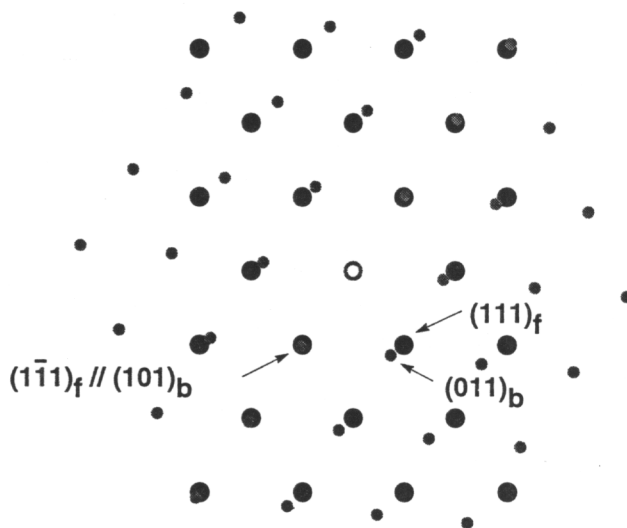


(b)

Figure 2.1: (a) Cross section of a bcc precipitate formed by aging Ni-45wt% Cr at 950°C for 4200 seconds, (b) a schematic of the precipitate lath cut by the foil nearly perpendicular to the elongated direction. The arrows indicate the directions of ledge growth migration. (c) The corresponding diffraction pattern of the precipitate in this orientation ( $[\bar{1}01]_f \parallel [\bar{1}\bar{1}1]_b$ ), and (d) the indices for (c).



(c)



(d)

Figure 2.1(c) and (d)

invisibility criterion [62, 49] and two-beam bright field micrographs. TEM contrast simulation [63, 64] was applied when the Burgers vectors could not be identified uniquely. The weak-beam dark field (WBDF) technique was used whenever possible to resolve the defects and to allow more accurate quantitative measurements [65, 66]. For many of the precipitates investigated, WBDF images using  $\mathbf{g} = \{111\}_f$  and  $\mathbf{g} = \{200\}_f$  yielded good resolution and, in some cases, a clear distinction between ledges and dislocations in the interfaces.

## 2.3 Results

### 2.3.1 Basic Parameters: Habit Plane and Side Facet

Fifty precipitates were analyzed, twenty three of them could be tilted and viewed along the cross-section (along the near-invariant line direction). In some of the precipitates tilted to the  $[\bar{1}01]_f$  zone axis, the orientation relationship was close to, but not exactly, the K-S OR. In these cases, the  $(1\bar{1}1)_f$  was parallel to the  $(101)_b$ , but the  $[\bar{1}\bar{1}1]_b$  direction was not exactly parallel to  $[\bar{1}01]_f$ . The largest deviation found between these two directions was  $\sim 0.9^\circ$ . Two out of the fifty precipitates studied deviated substantially from a K-S OR; these were ascribed to the influence of a heterogeneous nucleation site [67] and were not studied further.

Figure 2.2 shows the orientations of the habit planes and side facets determined by trace analysis on the fifty precipitates. The average orientation of the fifty habit planes is  $\sim (1\ \bar{2}.05\ 1.17)_f$ . The largest deviation from this average is approximately  $10^\circ$ . The side facet orientation ranges from  $(212)_f$  to  $(10\ 1\ 10)_f$  and averages  $(3.78\ 1\ 3.96)_f$ . These are both consistent with values reported by Luo and Weatherly [13].

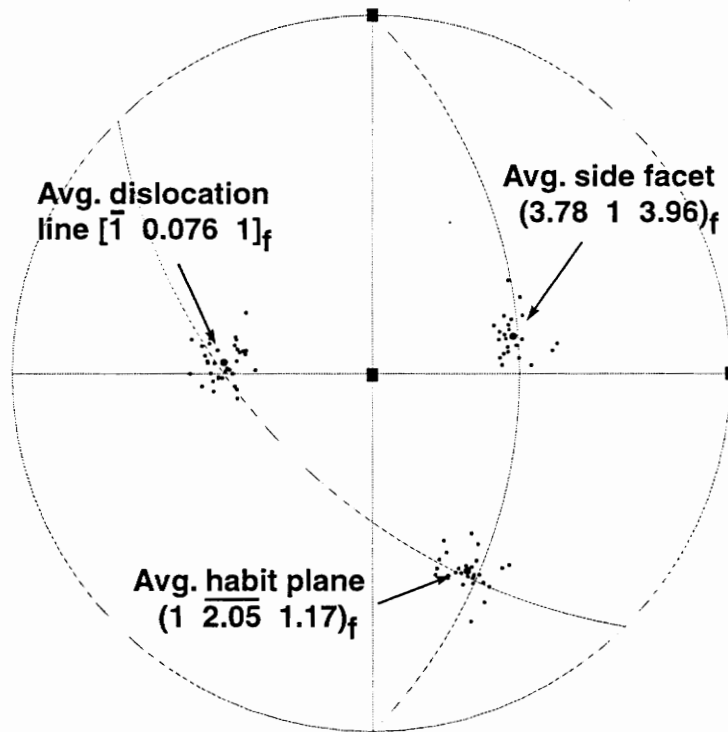


Figure 2.2: The poles of the habit plane, the side facet and the line direction of dislocations lying in the habit plane.

### 2.3.2 Shapes of Precipitates and Ledges

From the twenty three precipitates viewed along  $[\bar{1}01]_f$ , the real width and thickness of the precipitates could be measured directly, since the precipitates are oriented in edge-on cross-section. The widths of precipitates fell between 330 and 700 nm, and their thicknesses were between 170 and 400 nm. Due to the small probability of sectioning precipitates parallel to the elongated direction, the length of precipitates were not measured accurately. The precipitate aspect ratio (width to thickness) ranged from 0.9 to 3.5 with an average of 2.01.

The orientations of the habit plane and side facet do not change with aspect ratio. However, the precipitates with a higher aspect ratio tended to have a below-normal thickness, i.e., these precipitates appear to have a higher aspect ratio because thickening was restricted. The precipitates with lower aspect ratio tended to be the ones that deviated most from the exact K-S OR.

Growth ledges on the habit plane have a facet parallel to  $(1\bar{1}1)_f$ , which is the conjugate close-packed plane of the K-S OR, and it is at an angle of  $19^\circ$  to the habit plane (Figure 2.1(b)). These ledges have an average height of  $\sim 1.0\text{nm}$  [49, 60].

For ledges on the side facets, no major planes seem to dominate, and they sometimes coalesce into a larger size step with a facet of  $\sim (\bar{3}1\bar{3})_f$  [68]. The  $\sim (\bar{3}1\bar{3})_f$  was calculated as the best-matching plane in this system using the Bain correspondence [47].

### 2.3.3 Observations of Defect Structure

#### Parallel defects on habit plane

Parallel but irregularly spaced dislocations and ledges are found in the habit planes lying approximately parallel to  $[\bar{1} 0 1]_f$ . Examples of both are shown in Figure 2.3. The

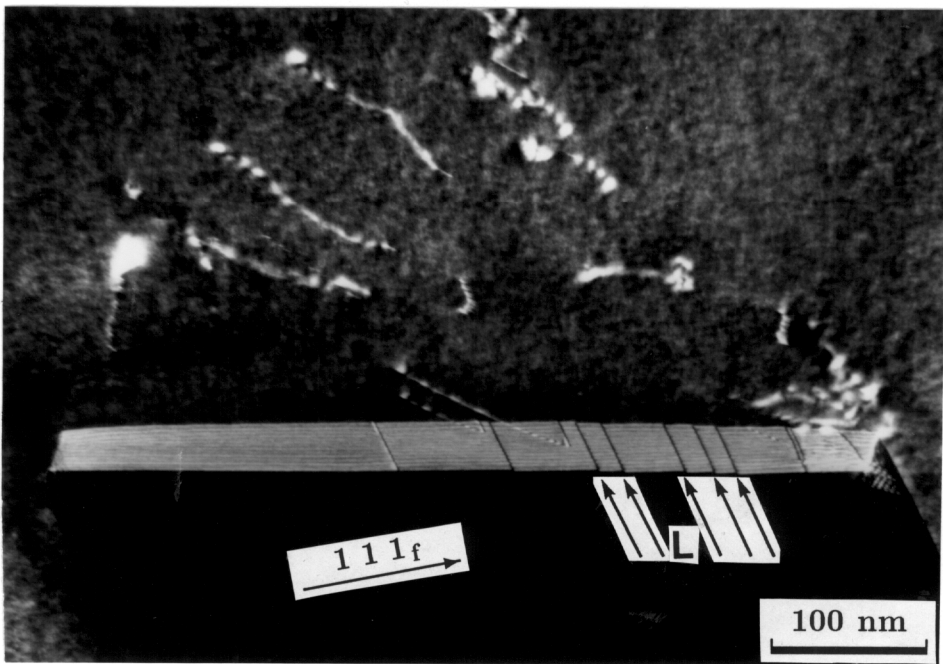
average dislocation line direction is  $[\bar{1} 0.076 1]_f$  (Figure 2.2). WBDF contrast can be used to distinguish dislocations and ledges in the broad face (Figure 2.3(a)-(b)). In the  $\mathbf{g} = 1 1 1_f$  WBDF micrograph of Figure 2.3(b), five isolated ledges with dark contrast can be seen on right side of the interface (indicated by arrows and “L” in Figure 2.3(b)), two ledges terminated by dislocation lines in the middle of the interface are also seen with a bright contrast. (The growth ledges proceed from left toward right in this interface [60].) The dislocation lines lose contrast with a  $\mathbf{g} = 1 \bar{1} 1_f$  (Figure 2.3(c) and (d)). The Burgers vectors of the two dislocations lie in the  $(1 \bar{1} 1)_f$  plane and have a Burgers vector a  $\mathbf{b} = \frac{1}{2}[110]_f$ . These two dislocations have departed from the interface and leave no ledge contrast in the interface.

The isolated ledges lose contrast using a  $\mathbf{g} = 1 \bar{1} 1_f$  (Figure 2.3(c) and (d)), but they have different contrast from the dislocations in bright field and in WBDF observations. The effective Burgers vector of the ledges identified by contrast analysis is  $\mathbf{b} = \frac{1}{2}[\bar{1}01]_f$ ; this direction lies in the habit plane. The different Burgers vectors of the dislocations and the ledges indicate a dislocation–ledge reaction. Because these dislocation or ledges all have Burgers vectors parallel to the  $(1 \bar{1} 1)_f$ , none of them can be seen in the interface in Figure 2.3(c)-(d), although the defects are present as shown in Figure 2.3(a) and (b). However, it has to be noted that not all of the dislocations and ledges have the same Burgers vectors as those shown in Figure 2.3, i.e., their Burgers vectors may differ in one defect from the other.

Of the 62 dislocations in the habit plane that were analyzed using the  $\mathbf{g} \cdot \mathbf{b} = 0$  technique, the Burgers vectors were distributed as follows: 34% had  $\mathbf{b} = \frac{1}{2}[110]_f$ , 42%  $\mathbf{b} = \frac{1}{2}[011]_f$ , 11%  $\mathbf{b} = \frac{1}{2}[10\bar{1}]_f$ , 8%  $\mathbf{b} = \frac{1}{2}[101]_f$ , and 5%  $\mathbf{b} = \frac{1}{2}[1\bar{1}0]_f$ . The first three Burgers vectors lie in the conjugate  $(1\bar{1}1)_f$  plane and account for more than 85% of the defects associated with the habit plane.

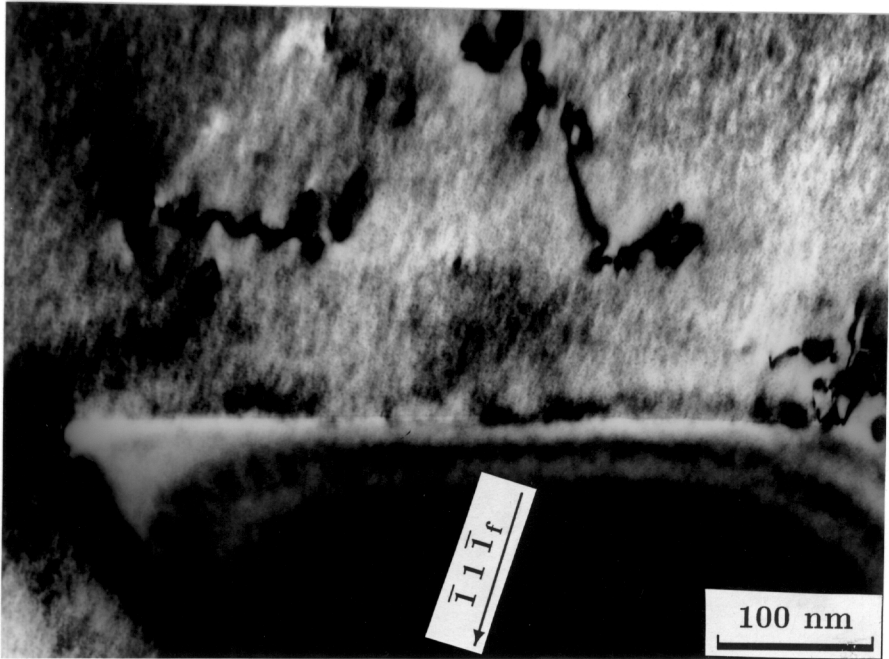


(a)

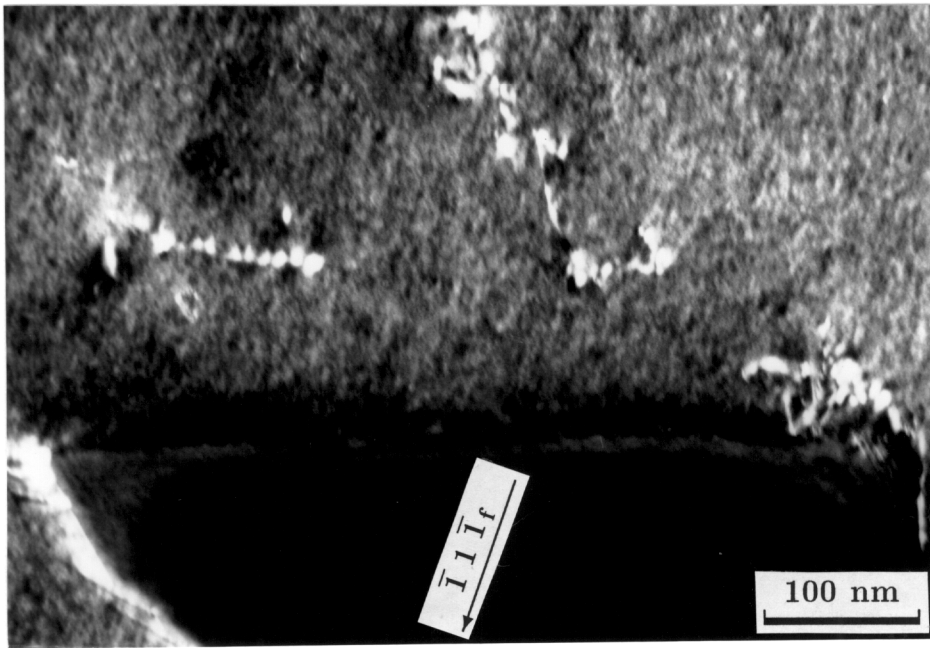


(b)

Figure 2.3: Two-beam bright field (a) and weak-beam dark field (b) micrographs of the  $(1\bar{2}1)_f$  habit plane using  $g = 111_f$ . (c) and (d) are two-beam bright field and weak-beam dark field micrographs of the same interface using  $g = 1\bar{1}1_f$ . “L” represents ledges



(c)



(d)

Figure 2.3 cont.

### Stacking faults on the starting tip of broad face

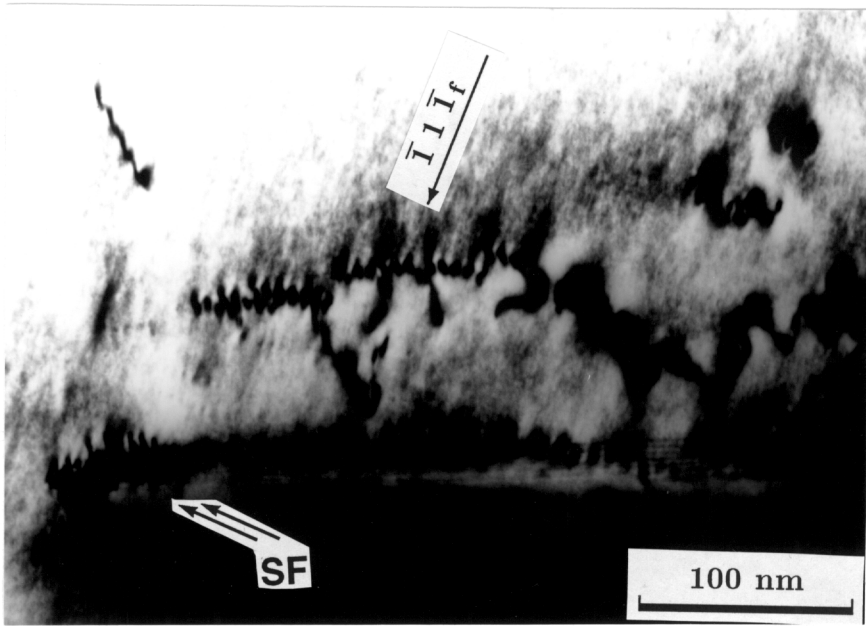
Shockley type stacking faults lying in the  $(111)_f$  plane were observed to extend from the habit plane  $\sim 12$  nm into the fcc matrix on 65% of the precipitates analyzed. Several stacking faults spaced approximately 14 nm apart were often found on a given habit plane near the acute corner between the habit plane and the side facet (where growth ledges often originate [60], see schematic of Figure 2.1(b) and Figure 2.4(a) and (b)). The stacking faults lie in the  $(111)_f$  plane and have a fault vector ( $\mathbf{R}_F$ ) of  $\pm\frac{1}{3}[111]_f$ . All the stacking faults observed had the same fault vector.

These faults were identified as Shockley type by using  $\mathbf{g} = 111_f$  to remove the contrast from both the stacking fault and the two bounding partials at the same time (Figure 2.4(c) and (d)). The partial dislocation lying in the habit plane was observed in one case to be emitted into the matrix leaving behind a ledge behind in the interface [68].

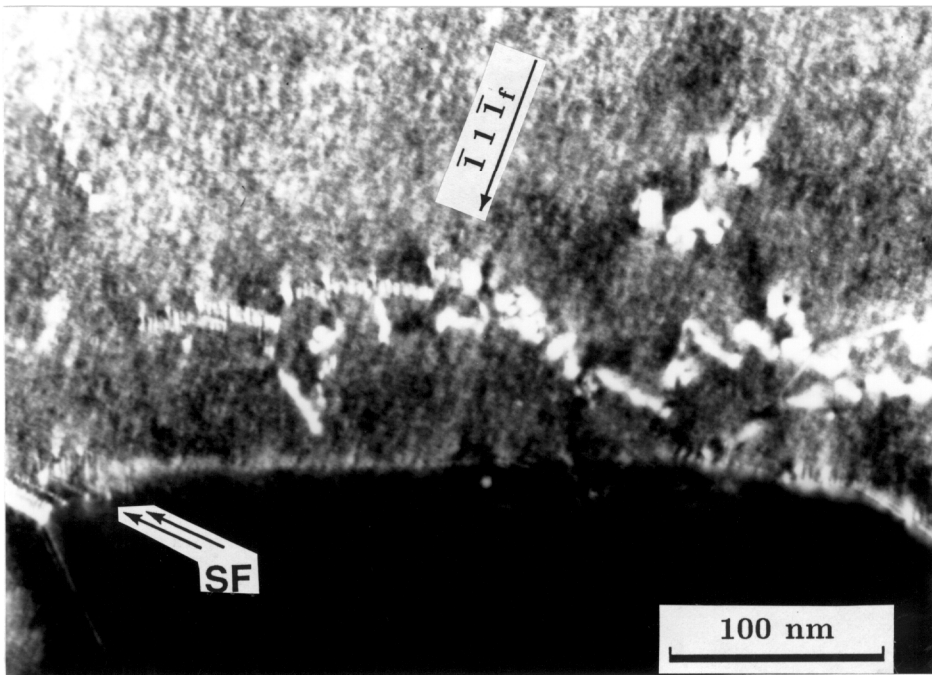
### Defects in the matrix

Arrays of dislocations are found in the fcc matrix adjacent to most precipitates. The dislocation lines are usually aligned almost parallel to the habit plane. Most of these dislocations lose contrast when imaged with  $\mathbf{g} = 1\bar{1}1_f$  or  $\mathbf{g} = 111_f$  (Figure 2.3(c) and (d) and Figure 2.4(c) and (d)). Their Burgers vectors must therefore lie in either the  $(1\bar{1}1)_f$  or  $(111)_f$  plane. The dislocations that have Burgers vectors parallel to  $(1\bar{1}1)_f$  may be related to the  $\sim 85\%$  of dislocations in the habit plane.

On the other hand, a group of dislocations are visible using  $\mathbf{g} = 1\bar{1}1_f$  but invisible using  $\mathbf{g} = 111_f$  indicating that their Burgers vectors are parallel to the  $(111)_f$  plane (Figure 2.4(a)-(d)). These dislocations separate from the habit plane by a distance of  $\sim 75$  nm and are probably related to the  $(111)_f$  stacking fault discussed previously.

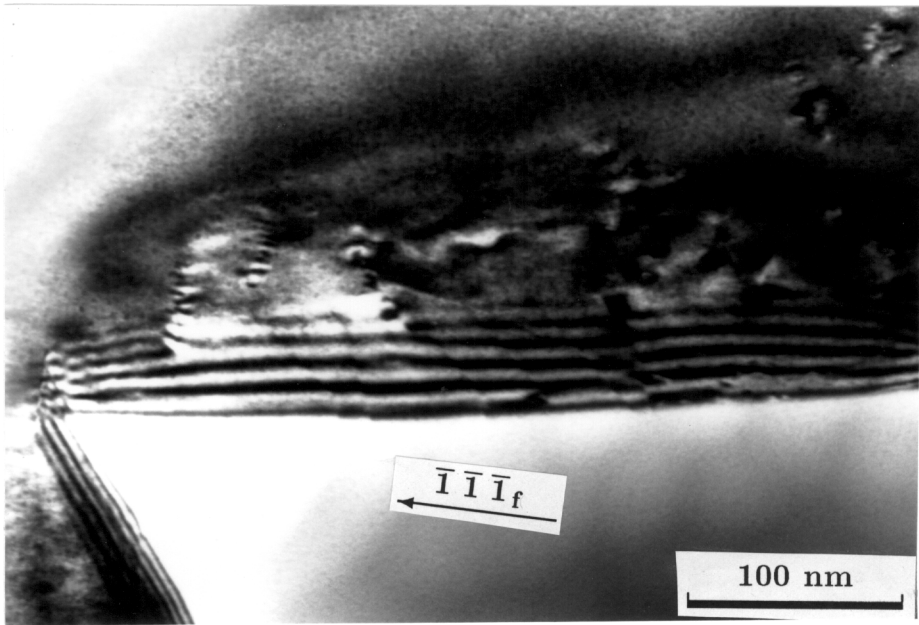


(a)

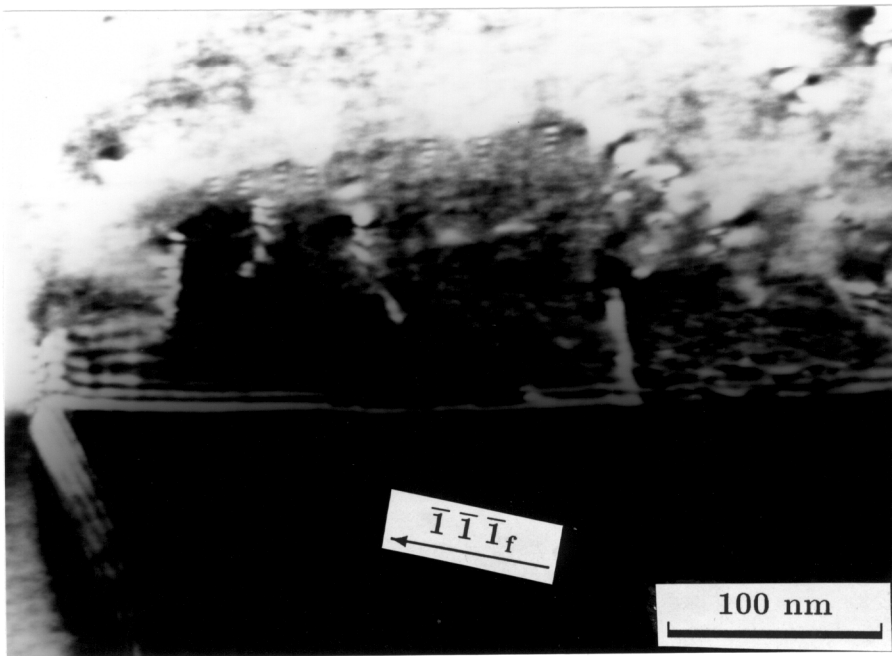


(b)

Figure 2.4: (a) and (b): Bright field and WADF microstructure of habit plane using  $g = 1\bar{1}1_f$ . (c) and (d): Bright field and WADF microstructure using  $g = 1\bar{1}1_f$ . "SF" represents stacking faults.



(c)



(d)

Figure 2.4 cont.

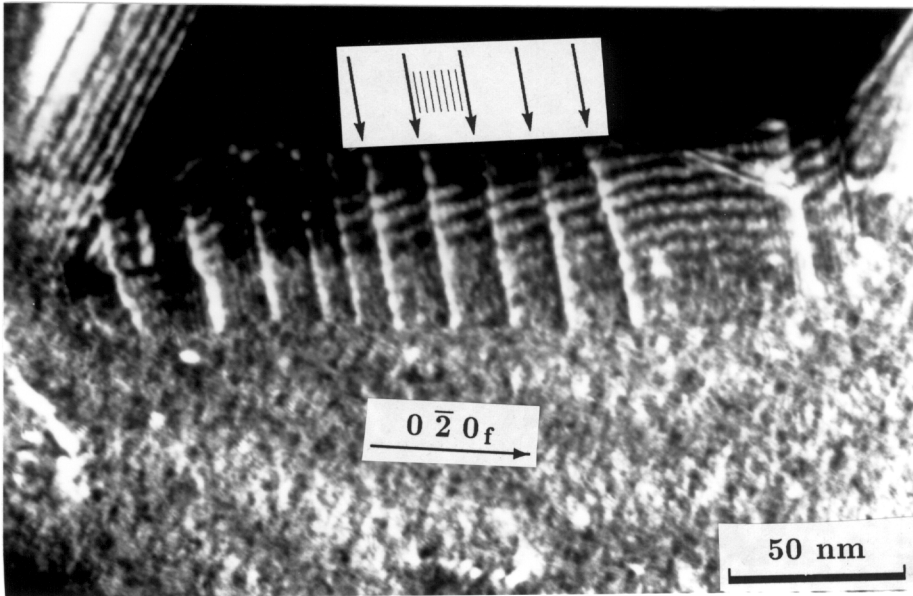
Groups of dislocations are also emitted from the edge of the precipitate at the obtuse junction of the habit plane and side facet. These dislocation lines generally lie along the  $[\bar{1}01]_f$  direction and they lie in a common  $(121)_f$  plane. Their Burgers vectors were found to be either  $\frac{1}{2}[110]_f$ ,  $\frac{1}{2}[011]_f$ , or  $\frac{1}{2}[\bar{1}01]_f$  (all of which lie out of the  $(121)_f$  plane). These dislocations thus cannot move conservatively in the  $(121)_f$  plane; they must climb to maintain the planar array. This appears to be the case during lath growth.

The 135 dislocation lines in the matrix that were analyzed had the following distribution of Burgers vectors: 35%  $\mathbf{b} = \frac{1}{2}[110]_f$ , 22%  $\mathbf{b} = \frac{1}{2}[011]_f$ , 26%  $\mathbf{b} = \frac{1}{2}[1\bar{1}0]_f$ , and 9%  $\mathbf{b} = \frac{1}{2}[0\bar{1}\bar{1}]_f$ . The first two Burgers vectors account for 57% of the dislocations and lie in the  $(1\bar{1}1)_f$  conjugate plane of the K-S OR. The latter two Burgers vectors lie in the  $(111)_f$  slip plane and account for 35% of dislocations.

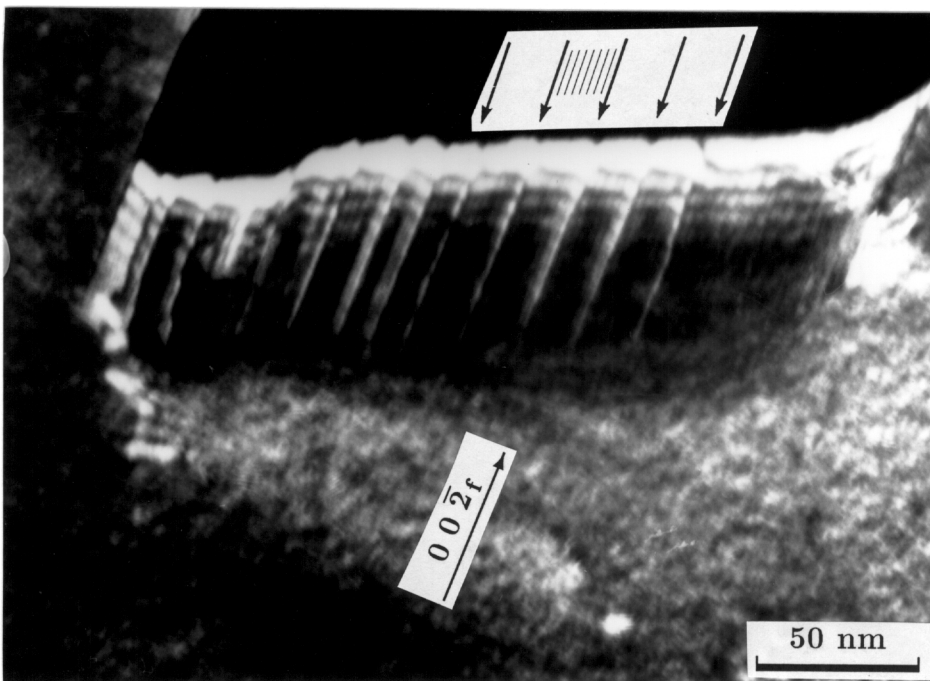
### Parallel dislocation lines in the side facet

Figure 2.5(a) and (b) show the structure observed on the side facet. An array of parallel, finely spaced features appear with weak contrast between regularly-spaced features with strong contrast. The strong contrast features are about 10 – 15 nm apart, whereas the faint features have a spacing of  $\sim 1.5$  nm. The same faint features were reported recently by Weatherly and Zhang [69] to be misfit dislocations. These faint features are best seen in WBDF with  $\mathbf{g} = 020_f$  or  $\mathbf{g} = 002_f$  (Figure 2.5(a)-(b)). No such fine features are observed, however, in the habit plane.

The stronger contrast dislocations on the side facet have a Burgers vector of  $\mathbf{b} = \frac{1}{3}[1\bar{1}1]_f$  and have been identified previously as misfit dislocations by Luo and Weatherly [49]. It can also be seen that there are comparatively fewer defects adjacent to the side facet than to the habit plane. Very few dislocations appear to be emitted during growth by defect reactions at the side facet.

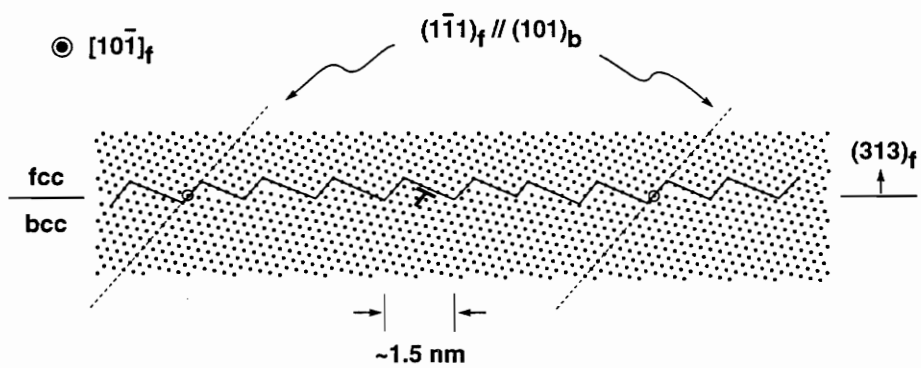


(a)



(b)

Figure 2.5: (a) and (b) show the side facet structures using WBDF technique. (c) Schematic of atomic structure of the  $(313)_f$  side facet.



(c)

Figure 2.5 cont.

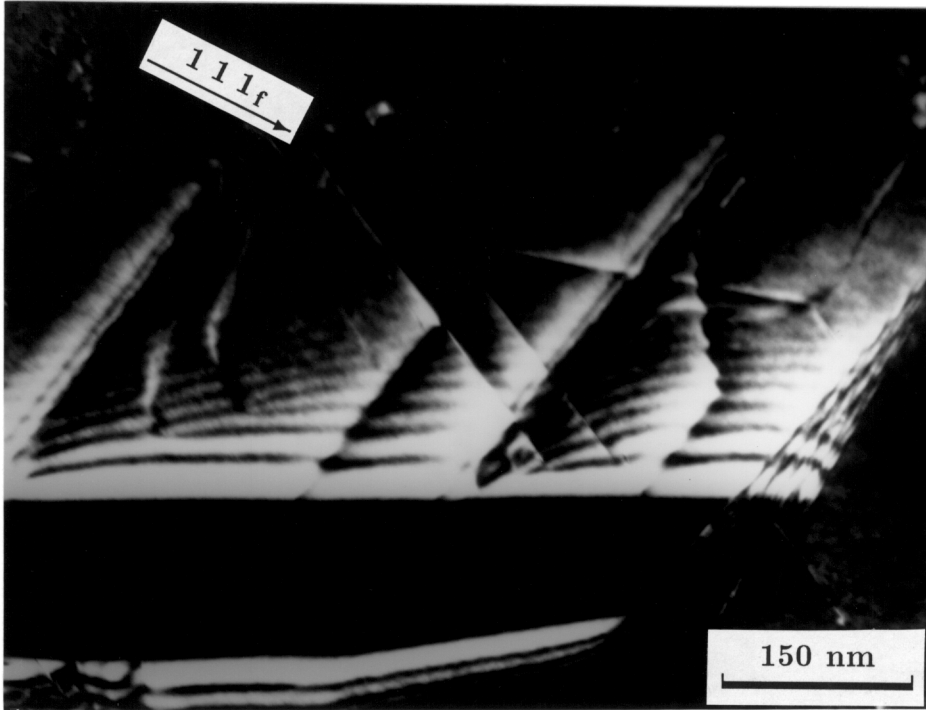
## Irregular defects

In addition to the dislocations and ledges in the habit plane oriented parallel to  $[\bar{1}01]_f$ , dislocation lines or steps are observed lying along  $[123]_f$  and  $[321]_f$  directions (Figure 2.6). These features are probably related to slip in the  $(11\bar{1})_f$  and  $(\bar{1}\bar{1}1)_f$  matrix planes since the  $[123]_f$  and  $[321]_f$  directions are the respective intersections of these slip planes with the  $(1\bar{2}1)_f$  habit plane. The lines are difficult to observe and characterize because the habit plane has to be inclined almost parallel to the foil surface in order to capture a significant length of the lines. Such orientations of the habit plane are rarely found in the foils due to the elongated shape of the precipitates. Figure 2.6(b) summarizes the observed defect structures in the habit plane and the side facet. Some ledges also shown in Figure 2.6(a) curve irregularly and do not have any specific low-index direction. The curved sections of these ledges contain a high density of kinks, and are believed to be relatively mobile portions of the growth ledge.

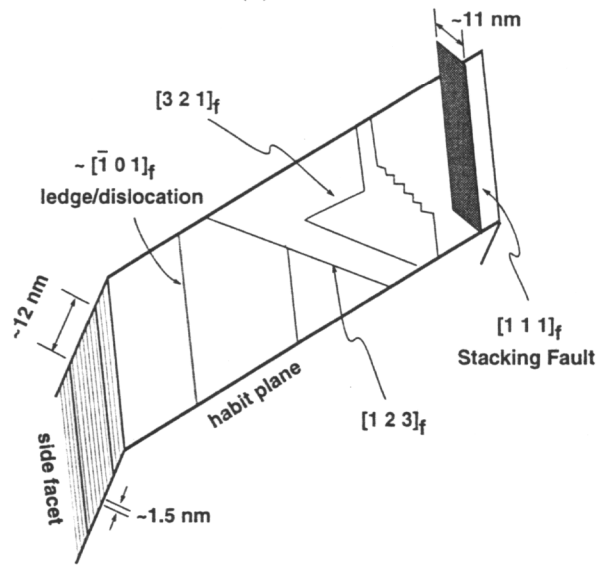
## HREM observations of the habit plane

The main purpose of the HREM observations is to observe the degree of matching between the fcc and bcc planes along the  $(1\bar{2}1)_f$  habit plane. Since the  $[\bar{1}01]_f$  direction allows one to view the precipitates edge-on, it is a convenient zone for resolving the atomic structure of the interface.

Figure 2.7 shows a region of  $\sim 20$  nm along the  $(1\bar{2}1)_f$  interface; a similar image of the same interface has been shown by Furuhashi et al. [59]. No misfit compensating defects can be seen in the interface when the micrograph is viewed along the conjugate  $(\bar{1}\bar{1}1)_f$  planes. Although some small disregistry is expected between the conjugate planes based upon the lattice parameter ratio  $a_f/a_b = 1.255$  (Figure 2.7(b)), the atomic planes are continuous



(a)



(b)

Figure 2.6: (a) Irregular defects on the habit plane. (b) Schematic of all defects observed on the habit plane and side facet and their orientations.

across the interface, and the habit plane appears to be coherent. In fact, the continuity of the conjugate atomic planes across this interface persists over a width of at least 50 nm.

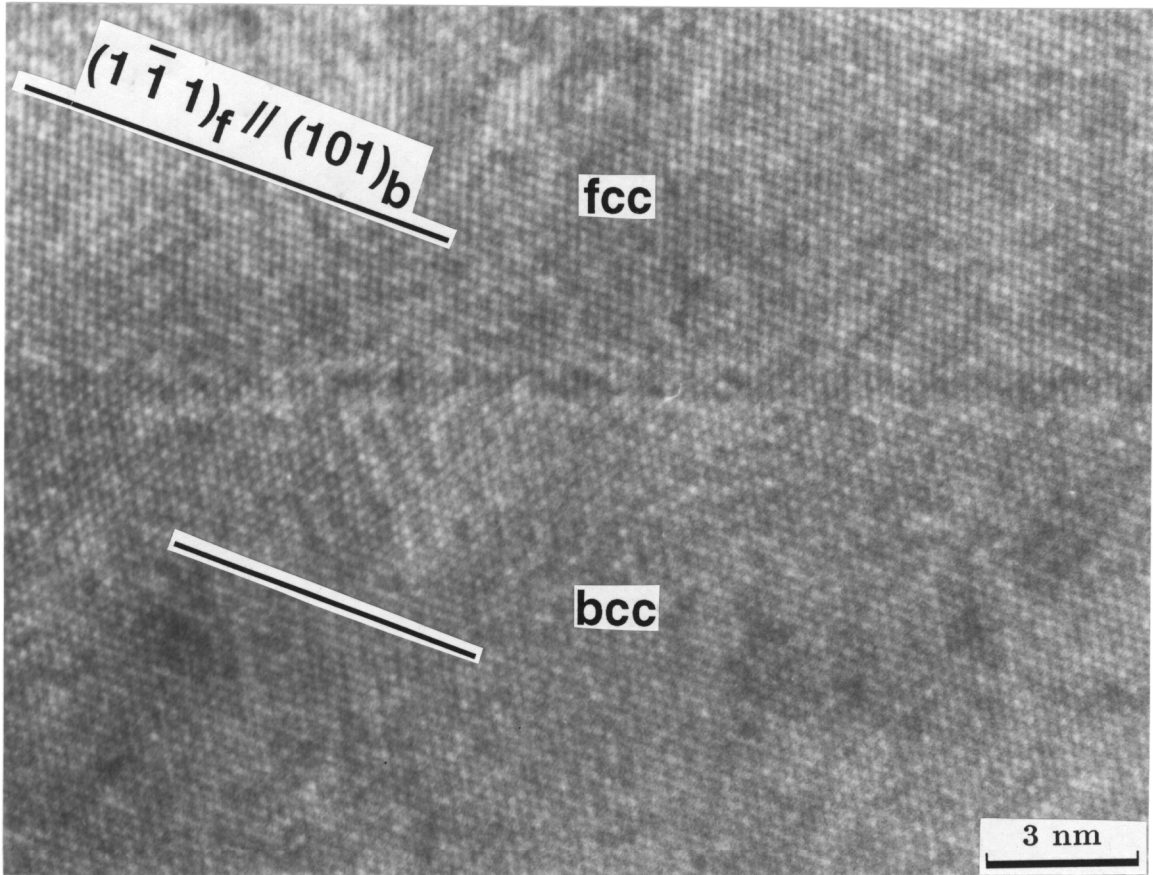
The  $(111)_f$  stacking faults located close to the edges of the precipitates can also be observed with HREM. Figure 2.8 shows two parallel faults in contact with the precipitate habit plane. The spacing between the two stacking faults is 14.4 nm, and the width of each faults is 11 nm.

## 2.4 Discussion

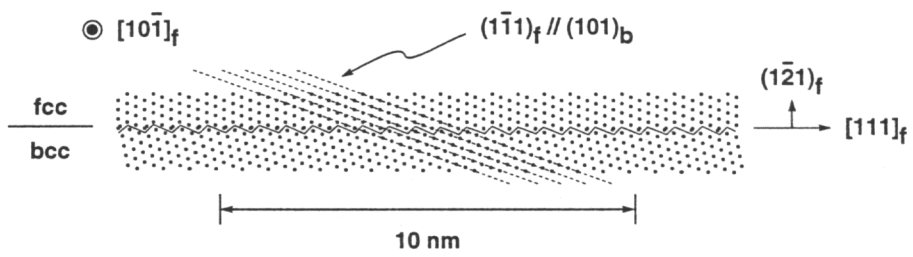
The formation of the observed defects in the interphase boundary and in the matrix near the precipitates can be considered based upon three possible functions: (1) they may accommodate dilatational strain resulting from the difference between the atomic volumes of the precipitate and the matrix, (2) they may accommodate interfacial misfit dislocations in an epitaxial interface [70, 71] if no lattice correspondence is operative, and (3) they may accomplish a homogeneous lattice deformation if a lattice correspondence is operative [16, 72]. While a regular array of dislocations were not found on the habit plane [69], the Bain correspondence is not operative [48]. The discussion will thus emphasize on the compensation of volume misfit and the roles of the observed defects in compensating the structural difference and in ledge formation.

### 2.4.1 Atomic Density Difference in Between Matrix and Precipitate Crystals

A possible explanation for the array of dislocations that appear to be climbing in the  $(121)$  plane from the obtuse corner of precipitate laths is that they accommodate dilatational misfit between the bcc and fcc phases. However, in most of the precipitates, such climbing



(a)



(b)

Figure 2.7: (a) HREM observation of the  $(1 \bar{2} 1)_f$  habit plane. (b) Calculated atomic structure of the habit plane for lattice parameter ratio  $a_f/a_b = 1.255$ .

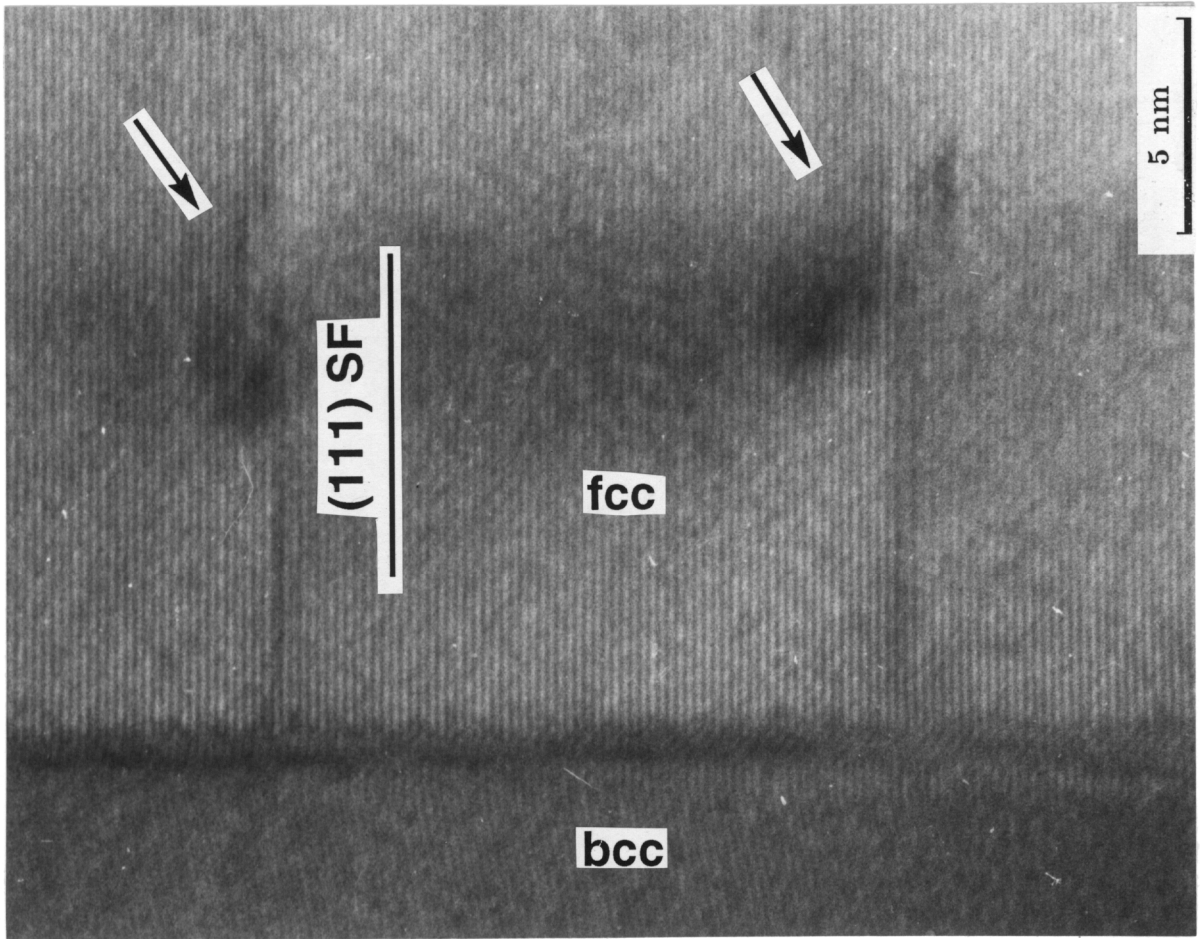


Figure 2.8: HREM observation of  $[111]_f$  Shockley faults at the  $(\bar{1}\bar{2}1)_f$  habit plane.

mechanism was not observed.

To have zero volume change during an fcc:bcc transformation, the lattice parameter ratio must be  $1.258(= 2^{\frac{1}{3}})$ . The lattice parameter ratio in Ni-Cr at 1100°C is 1.255 [57, 58]. The difference between these values leads to an atomic density difference of 1.18%. That is, 85 atoms of the precipitates occupy the same volume as 86 atoms in the matrix phase. For a typical-sized precipitate as observed in Section 2.3.2, this density difference is equivalent to 60 edge dislocation in the matrix each climbing a distance of about 100 nm. This density of dislocations is not observed, although the dislocation density does increase with continued growth of the precipitate laths [49, 60]. The absence of a sufficient number of climbing dislocations suggests the volume misfit is being accommodated by other mechanisms. Elastic strain is one possibility, the consumption of vacancies at the precipitate and matrix interface is another.

#### 2.4.2 Formation of $(1\bar{1}1)_f$ Slip-related Defects on The Habit Plane

In addition to the dilatational misfit, the  $a_f/a_b$  ratio of 1.255 also implies a substantial misfit of 2.4% between the d-spacings of the  $(1\bar{1}1)_f$  and  $(101)_b$  conjugate planes, i.e., an extra  $(101)_b$  should be seen every 27 nm along the habit plane. However, the absence of misfit dislocations and the one to one matching of these planes over a substantial portion of the habit plane indicates the interface must be elastically strained at the aging temperature. Indirect evidence for this is obtained from lattice parameter ratios measured from HREM images of the precipitate/matrix interface. The d-spacings determined from 80  $(1\bar{1}1)_f$  and 100  $(101)_b$  atomic planes (parallel planes) at the habit plane in Figure 2.7(a) yields a lattice parameter ratio of 1.24. The same procedure employed on 190  $(111)_f$  and 130  $(011)_b$  (planes in Figure 2.8) also gives a lattice parameter ratio of 1.24. However, the lattice parameter ratio increases to between 1.26 and 1.27 when calculated from  $\{111\}_f$  and

$\{110\}_b$  planes adjacent to the side facet. The misfit dislocations in the side facet presumably relieve a large portion of the misfit across this interface, so the lower lattice parameter ratio across the habit plane must be due to elastic strain. Few dislocations in the habit plane with Burgers vector out of  $(1\bar{1}1)_f$  plane are apparently because this misfit is accommodated elastically.

On the other hand, most (85%) of the dislocation associated with the habit plane have Burgers vectors that lie in the conjugate planes. These dislocations cannot accommodate the misfit resulting from the different spacings of the  $(1\bar{1}1)_f$  and  $(101)_b$  planes, but they may accommodate misfit within a common  $(1\bar{1}1)_f \parallel (101)_b$  plane. Mahon et al. [73, 59] proposed that each structural ledge in this habit plane consists of a transformation dislocation with  $\mathbf{b} = \frac{1}{12}[121]_f$ . Accumulation of these structural ledges may be fully accommodated by forming the same number of dislocations with  $\mathbf{b} = \frac{1}{2}[110]_f$  and  $\mathbf{b} = \frac{1}{2}[011]_f$  in the habit plane ( $[110]_f + [011]_f = [121]_f$ ). This may account for the similar frequency of finding dislocations with  $\mathbf{b} = \frac{1}{2}[110]_f$  (34%) and  $\mathbf{b} = \frac{1}{2}[011]_f$  (42%), whereas the other  $\mathbf{b} = \frac{1}{2}[\bar{1}01]_f$  occurs only in 11% of the defects on the habit plane. These dislocations may be emitted from the habit plane if the ledge proceeds to interact with another ledge (Figure 2.3(a) and (b)). These appear to account for 57% of the dislocations (35%  $\mathbf{b} = \frac{1}{2}[110]_f$  and 22%  $\mathbf{b} = \frac{1}{2}[011]_f$ ) that are found in the matrix.

The directions of ledges and dislocations oriented along  $[\bar{1}01]_f$  or the good matching elongated direction are explained by Luo and Weatherly [13, 49]. This elongated direction has the lowest misfit compared to any other direction in the habit plane; the directions perpendicular to this direction must have large misfit. To accommodate the accumulated misfit most efficiently, the dislocation lines are likely formed parallel to the good matching direction along which the direction and magnitude of the misfit to be compensated are similar.

As for the height of growth ledges, it is likely to depend upon the strain field around the ledges. Figure 2.9 shows a calculated structure that contains a 1.1 nm growth ledge with a  $(1\bar{1}1)_f$  facet. Such a ledge height (15 layers of  $(1\bar{2}1)_f$ ) maintains coherency both in front of and behind the advancing growth ledge by pattern advancing one basis vector. That is, the structural ledges at the base and top of the growth ledge match well. This should help alleviate the strain around the ledge. The estimated 1.1 nm ledge height is perhaps within the experimental error of the 1.0 nm measured height in this study and Luo and Weatherly's 0.9 nm [49, 60]. The structure of the ledge could not be observed directly with HREM because the ledges could not be viewed edge-on in the  $[\bar{1}01]_f$  zone axis.

One might get the impression from the schematic of Figure 2.9 that the growth ledge migrates to the right by successive motion of the smaller structural steps across the  $(1\bar{1}1)_f$  facet from bottom to the top. In this simple interpretation, each growth ledge would contain a Burgers vector of  $\frac{1}{2}[121]_f$ . There are, however, difficulties with this interpretation. The Burgers vector of the structural ledge (or transformation dislocation) is chosen following an arbitrary choice of the lattice correspondence. As is discussed in Reference [48], the observable interface characteristics are not consistent with any single lattice correspondence. The presence of kinks in growth ledges (right side of the interface in Figure 2.6) suggests strongly that the growth ledge in Figure 2.9 may not be the moving front of the transformation. The kink facets nearly perpendicular to the predominant growth direction of the precipitate could move forward and accommodate misfit along  $[\bar{1}01]_f$  direction by forming dislocations with Burgers vectors  $\frac{1}{2}[\bar{1}01]_f$ . This could account for the 11% of  $\frac{1}{2}[\bar{1}01]_f$  of defects (ledges or dislocations) that are found in the habit plane.



### 2.4.3 Stacking Faults and Formation of Ledges

The stacking faults found extending into the matrix from the habit plane on ~65% of the precipitates studied (Figure 2.4(a) and (b), Figure 2.8) were first observed by Chen et al. [68]. Other workers [49, 59] did not observe these faults in samples aged for longer times (up to 36,000 sec compared with 4200 sec in this study) which suggests the faults have a tendency to disappear as the precipitates grow.

Since the  $(111)_f$  stacking faults are perpendicular to the  $(1\bar{2}1)_f$  habit plane, they cannot travel parallel to the interface. Three observations provide clues as to their function. First, in several cases, a fault appeared to be rejected into the matrix and leaving behind a step in the habit plane [68]. It seems plausible that the stacking faults help form growth ledges, since a disconnection is left behind after the stacking fault is ejected into the matrix [74, 75]. The disconnection may help the nucleation of multiple-height growth ledge.

Second, the width of the stacking fault connected with the interface (~11 nm) is far wider than stacking faults in pure Ni [76, 77] (~3 nm) and in matrix a distance away from the precipitate. A wider fault can result if the fault energy is reduced or if an elastic interaction of the precipitate with the partial dislocations bounding the faults drives them further apart than their equilibrium spacing in the matrix. As suggested by Chen et al. [78], the strain energy favors ledge formation at the acute edge of the precipitate. This is where the stacking faults are usually found. The existence of these stacking faults could relieve the strain at the locations they are formed. This reduction of strain energy would contribute to the interaction between the two partials and increase the stacking fault width.

The possibility of segregation is supported by a study on the composition dependence of stacking fault energy in Ni–Cr alloys [79]. The stacking fault energy was measured to be

128 mJ/m<sup>2</sup> for pure Ni and 40 mJ/m<sup>2</sup> for Ni– 20 wt% Cr [80]. It drops even further as the concentrations of Cr increases. The higher Cr concentration on the fault may be combined with a higher diffusion path (the fault itself) to help develop the disconnection into ledges on the Cr-rich phase.

Once the ledge is formed and the faults are pushed away from the interface. Most of the faults collapse into single dislocation lines, since the faults do not appear to be stable in the matrix crystal. These faults and the dislocations are thus aggregated in groups at distance away from the interface. These defects should have Burgers vectors lying in the (111)<sub>f</sub> slip planes and account for the second largest population of defects found in the matrix (35%).

#### 2.4.4 Defects Observed on The Side Facet

Two types of linear defect contrast are observed on the side facets [49, 59]. The first type has bright contrast and a spacing of 10 – 15 nm. Finer faint contrast in between the parallel bright lines have an average  $\sim 1.5$  nm spacing (Figure 2.5). Such faint features with 1.5 nm spacing were proposed by Weatherly and Zhang [69] to be misfit dislocations (1.3 nm as predicted).

Figure 2.5(c) is a schematic of the calculated atomic structure for the side facet. The calculated atomic structure was constructed by combining the fcc and bcc crystals cleaved along the (313)<sub>f</sub> plane in K–S OR. A coincident site is placed at left hand side of the plot, and the structural ledges are plotted to show the 1.5 nm space with near-coincident sites on the corners of the ledges. Two close-packed planes ( $2(111)_f + 1(\bar{1}\bar{1})_f = (313)_f$ ) are chosen as the facets of the structural ledges [35]. These ledges have a  $\frac{1}{4}[121]_f$  projected Burgers vector in the plane of Figure 2.5(c) which suggests they could be either  $\mathbf{b} = \frac{1}{2}[110]_f$  or  $\mathbf{b} = \frac{1}{2}[011]_f$ . However, their contrast under two-beam conditions is considerably weaker than simulated images of interfacial dislocations with either of these Burgers vectors. On

the other hand, these structural ledges are visible whereas the ones on the habit planes are not (Figure 2.7(b)). Possible explanations for this difference are the ledge facets on the side facet do not match as well as those on the habit plane, and their ledge height is characteristically larger. HREM observations of the structural ledges in the side facet were attempted, but this facet plane was not exact edge-on orientation in the  $[\bar{1}01]_f$  zone.

In Figure 2.5(c), one extra layer of  $(1\bar{1}1)_f$  plane can also be found every 12 nm in the fcc matrix as suggested by Luo and Weatherly and by Furuhashi [49, 59]. This extra  $(1\bar{1}1)_f$  plane represents a dislocation with Burgers vector of  $\frac{1}{3}[1\bar{1}1]_f$ , i.e., these dislocations are misfit dislocations and are formed to compensate the misfit between the two structures on side facet. The side facet thus has a sessile dislocation structure than can only be displaced normal to itself if the  $\frac{1}{3}[1\bar{1}1]_f$  dislocations climb.

The other characteristic of the side facet is that the dislocation density in the matrix near the side facet is not as high as that near the habit plane. This suggests that most of the defects climb with the interface and are not ejected into the matrix when the interface advances. The lower dislocation density also suggests that the accommodation of volume change may be achieved by consumption of vacancies at the interface rather than the emission of climbing dislocations. The poorer matching at the side facet and thus the more open interface structure compared to the habit plane probably provides more sites to accommodate vacancies during growth.

## 2.5 Conclusion

TEM and HREM observations of the structure of the fcc:bcc precipitate boundaries in Ni-45 wt% Cr alloy and of defects related to precipitate growth were made. The following conclusions were drawn:

1. Misfit in the habit plane of the precipitates is very small and is compensated by, occasionally, irregularly-spaced dislocations with Burgers vectors lying in the conjugate planes of the orientation relationship, i.e.,  $(1 \bar{1} 1)_f \parallel (101)_b$ . These dislocations compensate structural misfit within the conjugate planes.
2. HREM observations of the habit plane confirm that  $(1\bar{2}1)_f$  is a good matching plane. The  $(1 \bar{1} 1)_f$  and  $(101)_b$  conjugate planes are found to have a one-to-one matching across matching for a region of at least 50 nm along the  $[111]_f$  direction. The d-spacing difference between  $(1 \bar{1} 1)_f$  and  $(101)_b$  is compensated by elastic strain.
3. Stacking faults on  $(1 1 1)_f$  plane bounded by Shockley partials extend from the habit plane into the matrix on 65% of the precipitates. The partial lying in the habit plane is ejected into the matrix during precipitate growth leaving a growth ledge in the interface. Once freed from the interphase boundary, the stacking fault and its bounding partials collapse into a unit dislocation on the  $(1 1 1)_f$  plane in the matrix.
4. The fine 1.5 nm spaced features found on the side facet appear to be structural ledges. In agreement with previous reports [49, 59], the strong contrast parallel to these fine features with a spacing of  $\sim 12$  nm is from misfit dislocations with Burgers vectors  $\mathbf{b} = \frac{1}{3}[1 \bar{1} 1]_f$ .
5. It is proposed that the volume change during precipitate growth is accounted for by the climb of matrix dislocations from the obtuse edges of the habit plane and by consumption of vacancies from the matrix.

# Chapter 3

## Atomistic Simulation of Fcc:Bcc Interface in Ni–Cr Alloys

### 3.1 Introduction

The embedded atom method (EAM)[81] is a convenient method for investigating the atomic structure [82] and energy of defects in crystals from a knowledge of interatomic potentials. It is particularly effective for studying aspects of defects that are difficult to measure experimentally. The structure and energy of the boundary between two phases is one such example [83]; interphase boundary structure and energy is important in the context of precipitate nucleation, growth, and coarsening, yet these remain difficult to obtain from experiment. The objective of this study is to evaluate the atomic structure and energy of an fcc:bcc interphase boundary in Ni–Cr alloy using molecular statics with EAM potentials.

A number of alloys [7, 15, 55] in which fcc:bcc transformations occur exhibit  $(1\bar{2}1)_f$ <sup>1</sup> precipitate habit plane when the two phases are in a Kurdjumov-Sachs orientation relationship (K–S OR)[56] :  $(1\bar{1}1)_f \parallel (101)_b$  and  $[\bar{1}01]_f \parallel [\bar{1}\bar{1}1]_b$ . Both structure calculations [48] and high resolution electron microscopy (HREM) observations[59] have demonstrated this interface to be coherent.

To calculate the structure and energy of this boundary, the EAM is applied to a simulation block consisting of a bcc crystal oriented in the K–S OR between two fcc crystals.

---

<sup>1</sup>an “f” or “b” subscript indicates the lattices of the plane or direction for fcc and bcc crystals, respectively.

The bcc crystal is separated from the fcc crystals by two boundaries parallel to the  $(1\ \bar{2}\ 1)_f$  plane. The atoms are located initially in sites corresponding to bulk crystals. The internal energy of the simulation block is calculated from EAM interatomic potentials, the atom positions are relaxed until the atoms in the simulation block reach a configuration with a minimum energy. The interfacial energy is obtained by subtracting the strain energy and internal energy of perfect fcc and bcc crystals from the energy of the simulation block. By changing the Cr concentration in the fcc crystals, the interface stability and energy can be studied as a function of fcc composition.

## 3.2 Procedure and Results

### 3.2.1 Interatomic Potentials for Simulations in Ni–Cr Alloys

A description of the embedded atom method can be found in Reference[81]. The total energy  $E_{tot}$  for a collection of atoms is expressed as:

$$E_{tot} = \sum_i F_i(\rho_{h,i}) + \frac{1}{2} \sum_{i,j(i \neq j)} \phi_{ij}(R_{ij}) \quad , \quad \text{where } \rho_{h,i} = \sum_{j(\neq i)} \rho_j^a(R_{ij})$$

The  $F_i$ 's are the embedding functions,  $\rho_{h,i}$  is the total host electron density of atom  $i$  with a  $\rho_j^a$  contribution from atom  $j$ , and  $\phi_{ij}$  is the pair potential between atoms  $i$  and  $j$ . The DEVIL code [84] was employed to optimize the configuration of atoms in the simulated block and find a minimum in the total energy of the block. This provides the relaxed positions of the atoms relative to the positions assumed before energy minimization.

The pair part of the potentials used in the simulations are shown in Figure 3.1. The Ni potential was originally developed by Voter and Chen [1]. The Cr potential was developed by Pasianot et al. [2] with the addition of angular terms using an “embedded defect” technique. For the present work, we chose this Cr potential without the addition of angular terms. This

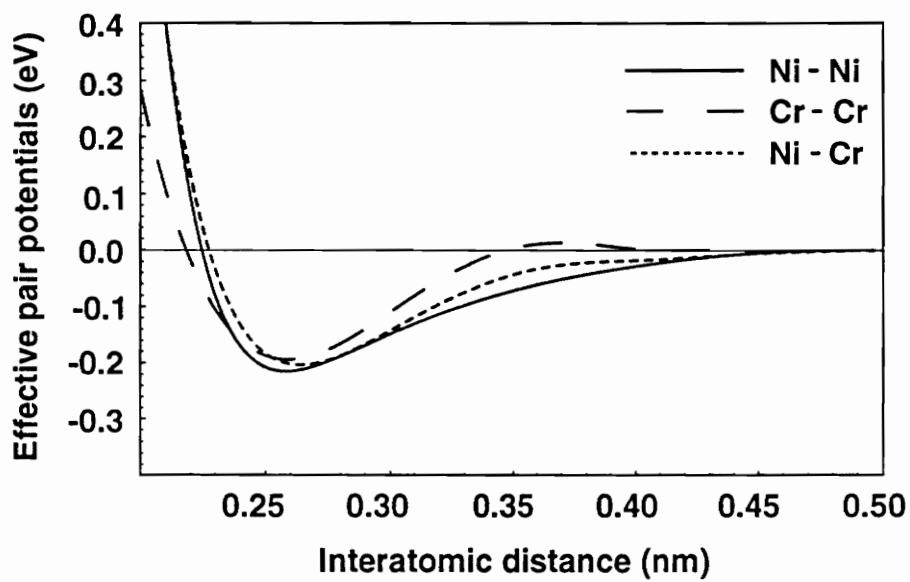


Figure 3.1: Effective pair potentials ( $\phi_{\text{Ni}[1]}$ ,  $\phi_{\text{Cr}[2]}$  and  $\phi_{\text{NiCr}}$ ) for Ni-Cr alloys employed in the present study.

reproduces the lattice parameter, cohesive energy, and bulk modulus for Cr correctly but does not fit the elastic constants ( $C_{11}$ ,  $C_{12}$ , and  $C_{44}$ ) with the same accuracy since chromium has a negative Cauchy pressure and cannot be modeled using the standard embedded atom technique (Table 3.1). However, the Cr potential was deemed accurate enough for the purpose of calculating the interfacial energy in Ni-rich Ni–Cr alloys.

The Ni potential of Reference [1] is not in the effective pair scheme; that is, the first derivative of the embedding function,  $F'(\rho)$ , is not equal to zero at the electronic density in the perfect lattice of a pure metal ( $\rho_0$ ). To be consistent with the Cr potential, we transformed the Ni potential to the “effective pair scheme” [86] as described by Farkas et al. in Ni–Al [87]. The transformation applied is as follows:

$$F^{eff}(\rho) = F(\rho) - \rho F'(\rho_0)$$

$$\phi^{eff}(R) = \phi(R) + 2\rho(R)F'(\rho_0)$$

In addition to this transformation to an effective pair scheme, the electronic density for the perfect Cr lattice was normalized to 0.34 (that of pure Ni was kept at 0.38 [1]). The similar electronic densities for pure Ni and Cr permit the development of a mixed Ni–Cr potential. The embedding functions and pair potentials yield a lattice parameter of 0.352 nm for fcc Ni and 0.287 nm for bcc Cr. The cohesive energies modeled by these potentials are  $-4.10$  eV/atom for Cr and  $-4.45$  eV/atom for Ni.

Since the embedding functions can be developed based upon the pure metals, the only function needed for the mixed interaction is the mixed pair function ( $\phi_{\text{NiCr}}$ ). For the mixed Ni–Cr potential, the EAM scheme used by Voter and Chen [1] to develop the Ni–Al potential was followed. The Ni–Cr interaction potential was expressed empirically as a linear combination of the Ni and Cr pair potentials (Figure 3.1):

$$\phi_{\text{NiCr}}(a + bx) = A[\phi_{\text{Cr}}(c + dx) + \phi_{\text{Ni}}(e + fx)] \quad (3.1)$$

where  $x$  has a value between zero and unity and represents the fraction of interatomic distance between the initial point ( $a$ ,  $c$ , and  $d$  for  $\phi_{\text{NiCr}}$ ,  $\phi_{\text{Cr}}$ , and  $\phi_{\text{Ni}}$ ) and the final point ( $a + b$ ,  $c + d$ , and  $e + f$  for  $\phi_{\text{NiCr}}$ ,  $\phi_{\text{Cr}}$ , and  $\phi_{\text{Ni}}$ ) of the range of interest. The parameters,  $A$  and  $a$  through  $f$ , are fitted to experimental enthalpies of mixing and Vegard's law (linear dependence of lattice parameters on composition) using a series of Ni–Cr solid solutions. The disordered fcc solid solutions were simulated using at least ten cell blocks with random distributions of Cr and Ni atoms. The best fit values obtained for these parameters are given in Table 3.2. In Figure 3.1, the interatomic distances that give rise to the minimum potentials are similar for the three pair potentials. Because Ni–Cr interaction potential is a linear combination of Ni and Cr pair potentials, the Ni–Cr interaction potential lies in between Ni and Cr pair potentials as interatomic distance is larger than 0.25 nm. In the region of 0.2-0.25 nm interatomic distance, the Ni–Cr interaction potential does not lie in between Ni and Cr pair potentials, because the initial and final points of the range of interest are somewhat different for three potentials. The Ni–Cr interaction potential appears to be closer to the Ni pair potential in this region.

Using the parameters of Table 3.2, the predicted fcc lattice parameter of the equiatomic disordered solid solution (50 Ni – 50 Cr) is 0.360 nm, and the cohesive energy of the mixed solution is  $-4.22$  eV. This implies a heat of mixing of 0.06 eV/atom; the value given by Hultgren et al. [88] at 1550°K is 0.07 eV/atom.

The stability of the Ni<sub>2</sub>Cr and Ni<sub>3</sub>Cr phases[89, 90, 91] was also evaluated. Neither of these are stable using the current atomic and pair potentials. The disordered fcc has a lower cohesive energy at these stoichiometric compositions.

To obtain the lattice constant of the fcc solid solution as a function of Cr concentration, multiple simulations were performed with a fixed number of Cr atoms located randomly in an fcc block of 108 Ni atoms. Figure 3.2 shows the simulated fcc lattice parameters at

Table 3.1: Experimental and calculated results of elastic constants for pure bcc Cr (units in GPa).

	$C_{11}$	$C_{12}$	$C_{44}$	bulk modulus ( $C_{11} + 2C_{12}$ )
experimental [85]	391.0	89.6	103.2	570.2
calculated	234.2	149.8	130.1	533.8

Table 3.2: Parameters obtained for the NiCr mixed interaction potential (Equation 3.1.)  $A$  is dimensionless and the distances  $a$  through  $f$  are in nm.

$A$	$a$	$b$	$c$	$d$	$e$	$f$
0.50	0.100	0.400	0.099	0.397	0.100	0.379

several Cr concentrations. These results can be represented by the following equation:

$$a_f(\text{nm}) = 0.352 + 0.0178X_{Cr} - 5.97 \times 10^{-3}X_{Cr}^2 \quad (3.2)$$

where  $X_{Cr}$  represents the mole fraction of Cr and  $a_f$  is the optimized fcc lattice parameter. It has to be noted that the coefficient in the quadratic term contributes little to the lattice parameter, therefore the lattice constants behave close to Vegard's law as assumed in the develop of the potentials. However, the quadratic term is used to improve the accuracy for simulating fcc structures at different composition in later simulations.

The composition dependence of the fcc and bcc cohesive energy are shown in Figure 3.3. It is noted that the cohesive energy of fcc and bcc intersects at a Cr concentration of 51 at%. The bcc becomes more stable than the fcc structure for  $X_{Cr} > 0.51$ , whereas fcc is stable for  $X_{Cr} < 0.51$ . The bcc curve in Figure 3.3 is interrupted at  $X_{Cr} \approx 0.5$ , because the bcc blocks of lower Cr concentration relax to other structure.

### 3.2.2 Configuration of the Simulation Block

The  $(1\bar{2}1)_f$  habit plane of a bcc precipitate formed during aging of a Ni-45 wt% Cr alloy at 950°C is shown in Figure 3.4(a). The parallel planes of the K-S OR can be seen by comparing the image with the schematic of Figure 3.4(b), which also shows the initial positions of atoms in the interface region used in the simulation block. At the atomic level, the  $(1\bar{2}1)_f$  habit plane is coherent and consists of structural ledges  $[35]$  with the  $(1\bar{1}1)_f$  and  $(0\bar{2}0)_f$  facets. The positions of these structural ledges were chosen at which the  $(111)_f$  close-packed plane (perpendicular to the habit plane) and  $(022)_b$  plane intersects ( $79^\circ$  from the habit plane).

The DEVIL computer code [84] was used, and the simulation block was constructed with periodicity in three orthogonal directions. The  $x$ ,  $y$ , and  $z$  directions were chosen to

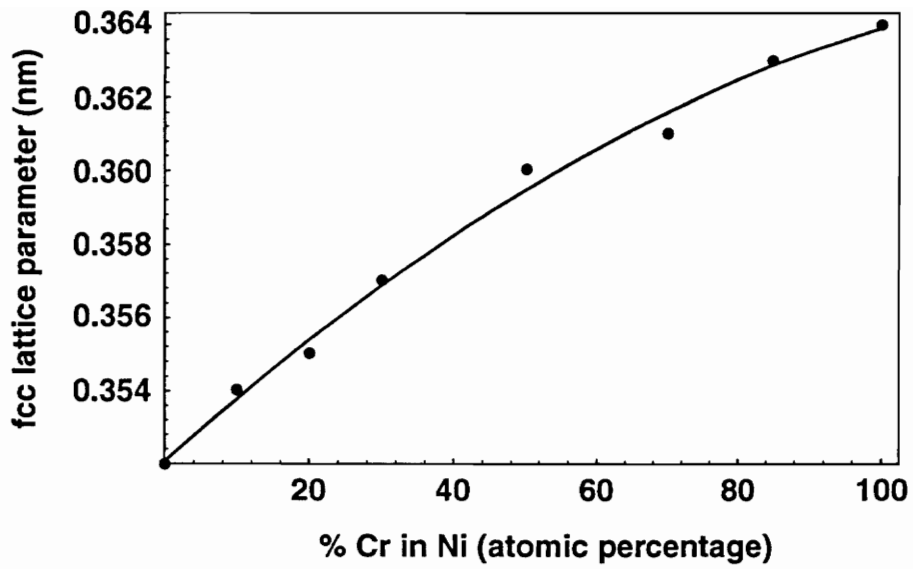


Figure 3.2: Dependence of the lattice parameters on composition of fcc alloys obtained from the simulations (represented by dots in the plot). The solid line is Equation 3.2.

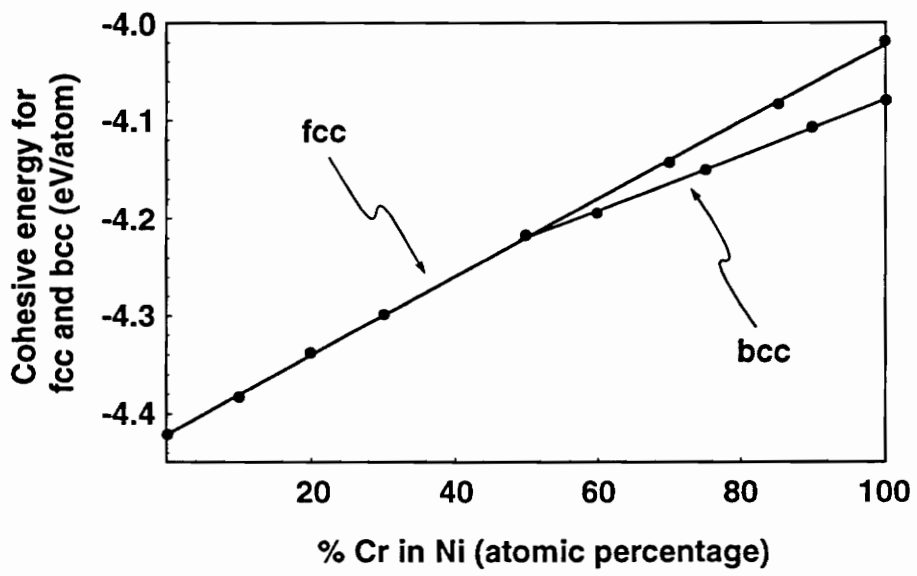
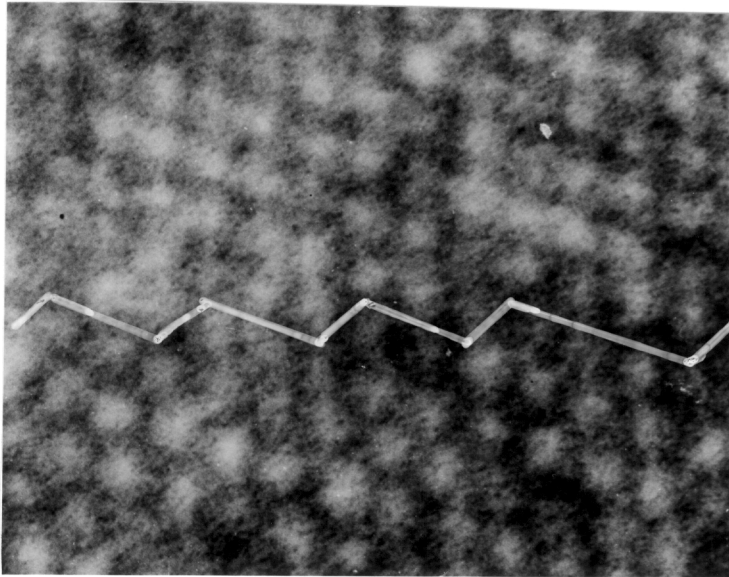
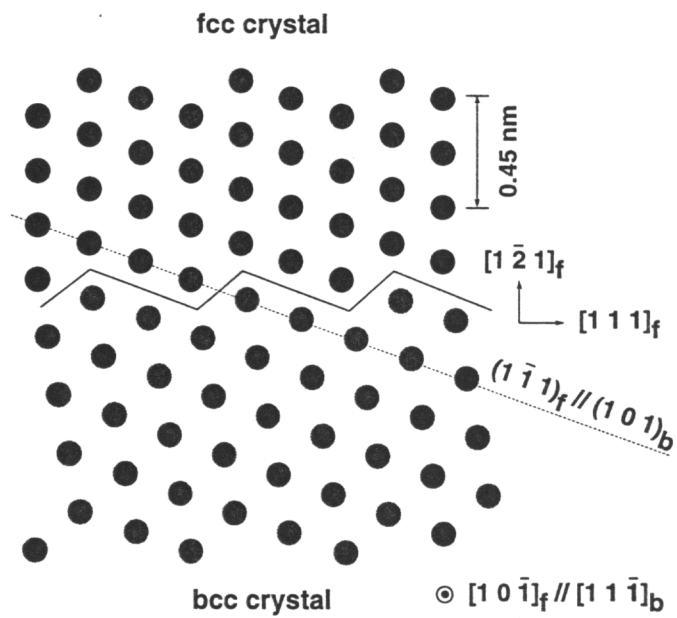


Figure 3.3: Change of fcc and bcc cohesive energy versus composition.



(a)



(b)

Figure 3.4: (a) High resolution electron microscopy image of the  $(1\bar{2}1)_f$  habit plane of a bcc precipitate formed during aging of Ni-45wt%Cr at 950°C. (b) Atomic structure of the simulated interface.

be  $[111]_f$ ,  $[\bar{1}\bar{2}1]_f$ , and  $[10\bar{1}]_f$  directions, respectively. This coordinate assignment placed the  $y$ -direction perpendicular to the interface plane. The size of each fcc crystal along the three directions was:  $3[111]_f$  or  $3\sqrt{3}a_f$  for  $x$ ,  $2[\bar{1}\bar{2}1]_f$  or  $2\sqrt{6}a_f$  for  $y$ , and  $\frac{1}{2}[10\bar{1}]_f$  or  $\sqrt{2}a_f/2$  for  $z$  direction for a total of 72 atoms in each fcc crystal.

The periodicity values in the  $x$ - and  $z$ -directions for the bcc crystal were chosen such that they were close to those of the fcc crystals to ensure coherency. According to the K-S OR, the  $x$ -dimension of the fcc crystal,  $[333]_f$ , is close to  $[\bar{1}\bar{5}4]_b$ , so the periodicity of the bcc crystal in the  $x$ -direction was chosen to be  $\sqrt{42}a_b$ . Similarly, the fcc  $z$ -direction,  $\frac{1}{2}[10\bar{1}]_f$ , is parallel to  $\frac{1}{2}[11\bar{1}]_b$ , so the  $z$ -periodicity of the bcc crystal was selected to be  $\sqrt{3}a_b/2$ . The periodicity of the bcc crystal along the  $y$ -direction, or the thickness of the bcc precipitate varied in the simulations, but was always an integer multiple of  $[3\bar{1}2]_b$  (or  $\sqrt{14}a_b$ ) to maintain periodicity along the parallel  $[\bar{1}\bar{2}1]_f$  direction in the fcc crystal. The minimum size of the bcc crystal (and each increment in size) was 42 atoms, and a bcc crystal of this size is hereafter termed a bcc module.

The bcc crystal was strained elastically to force coherency at the interface. Because the fcc lattice parameter changes with Cr concentration, the bcc strain required to force coherency varied with the Cr concentration in the fcc crystals. The strains applied to the bcc crystal in the  $x$ - and  $z$ -directions (parallel to the interface) were determined from the ratios of the periodicities of the bcc and fcc crystals in these directions. For the  $x$ -direction, this ratio was  $(3\sqrt{3}/\sqrt{14})a_f/a_b$  which ranged from  $-1.7\%$  to  $1.6\%$  for the Cr concentrations considered. The strain in the  $z$ -direction was between  $0.09\%$  and  $3.5\%$ .

A range of bcc strains in the  $y$ -direction (perpendicular to the interface) was tested. It was found that the lowest energy corresponds to the  $y$ -strain which, together with the aforementioned  $x$ - and  $z$ -strains, produces a zero volume change in the bcc crystal. That is, stretching the bcc crystal in the plane of the interphase boundary causes a contraction

perpendicular to the boundary just enough to maintain a constant bcc volume. The same conclusion was reached in an equivalent study using Fe EAM potentials [92].

According to the Ni–Cr phase diagram (Figure 3.5), the equilibrium fcc composition for a two phase alloy at 950°C is 38 at% Cr and the equilibrium bcc composition is 95 at% Cr. The composition of the bcc crystal in the simulations was chosen for convenience to be 100 at% Cr. The Cr concentration in the fcc crystals was varied systematically. Since the fcc structure is disordered, there are many ways of placing Cr atoms in the lattice. For each Cr concentration, at least ten random configurations of the Cr atoms were used to obtain the average block energy. Since the fcc crystals were found to be stable for Cr concentrations up to 51 at%, the concentrations considered are between 0 and 51 at%.

In addition to the fcc lattice constant and the bcc strains, the rigid body translation between the fcc and bcc crystals also had to be optimized to yield the lowest energy. Simulations at three fcc compositions, 0 at%, 20 at%, and 40 at% Cr, were made to obtain a parabolic dependence of the optimum rigid body translation on the Cr concentration in the fcc crystals. The optimized rigid body translation in the  $x$ -direction is  $(-0.026 + 0.0688X_{Cr} - 0.231X_{Cr}^2)$  nm, and the translation in the  $y$ -direction was  $(0.0115 + 0.00846X_{Cr} + 0.0456X_{Cr}^2)$  nm. The final simulation blocks included all of the optimized parameters aforementioned to derive the most stable relaxed structures.

### 3.2.3 Evaluation of Interface and Strain Energy

The excess energy was obtained by subtracting the cohesive energy of the fcc and bcc portions of a simulation block from the total energy of a simulation block. It is composed of two terms, the elastic strain and the interface energy [92]. The interface energy contribution does not change with the size of the block as long as the area of the interface stays constant. On the other hand, the strain energy is proportional to the volume of the bcc crystal,

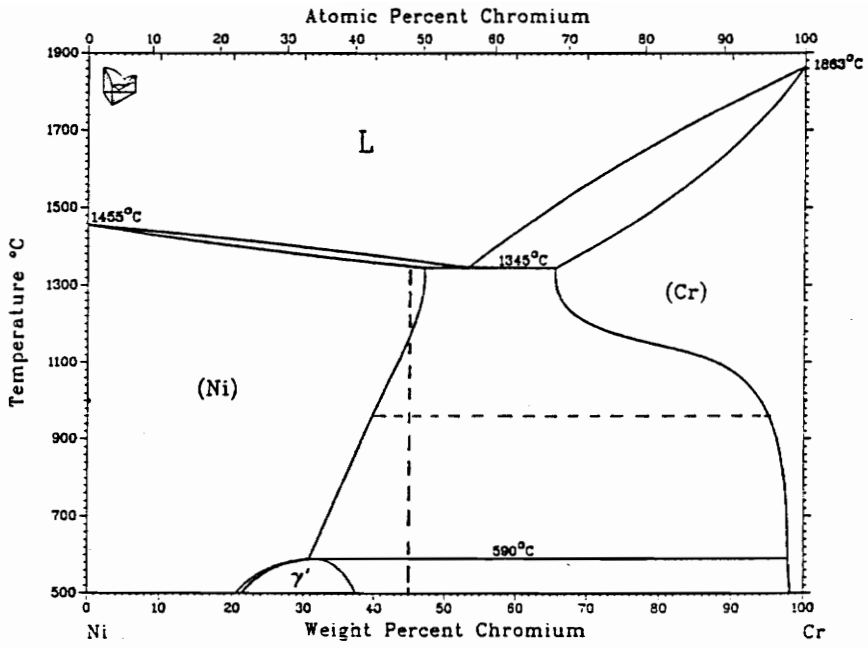


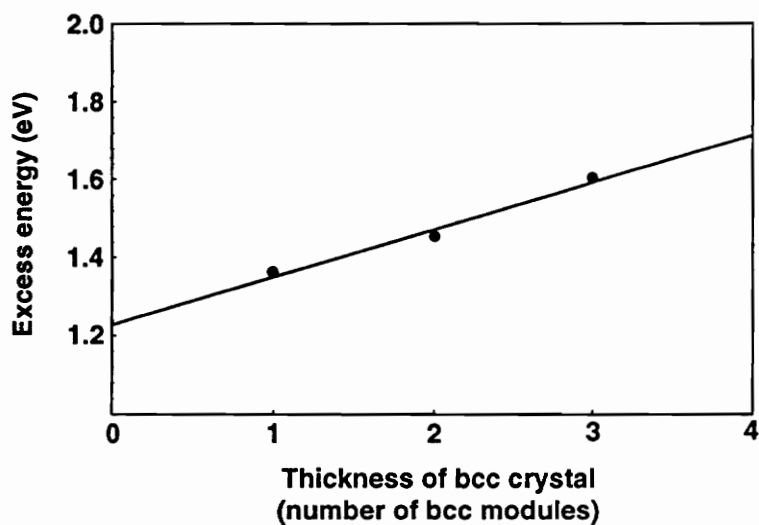
Figure 3.5: Ni-Cr phase diagram [3].

therefore the excess energy increases linearly with the thickness of the bcc crystal for a constant interface area. The slope of this linear relationship gives the strain energy [83]. The interface energy can be obtained by extrapolating the excess energy to zero bcc thickness, i.e., to a infinitely thin layer of the bcc phase with two interfaces.

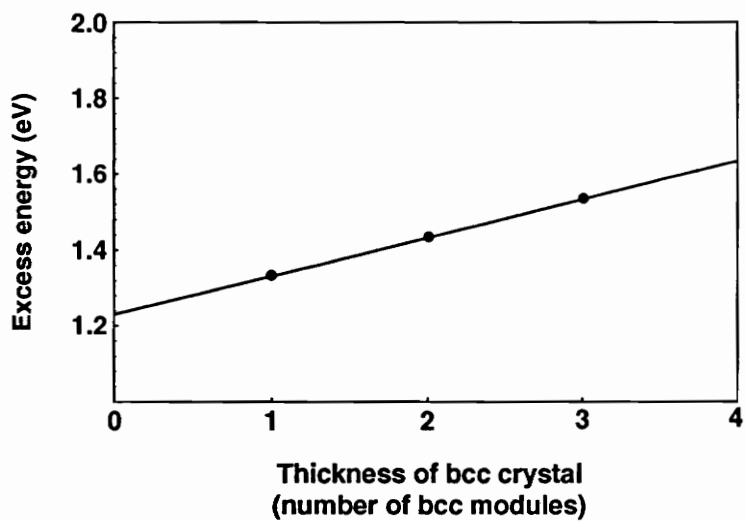
Since the smallest bcc crystal that can be simulated with the present approach contains 42 atoms, one or more bcc modules of this size could be extended in the  $y$ -direction and sandwiched between two fcc crystals of 72 atoms each. The number of bcc atoms included in the simulation blocks were thus 0, 42, 84, or 126. These simulations with different bcc crystal sizes were used to obtain the linear relationship between excess energy and bcc crystal thickness and to evaluate the interface energy and strain energy.

Ten simulations were carried out for each fcc composition except 0 at% Cr, so each linear relationship between excess energy and bcc crystal thickness included 40 different simulations using 4 different bcc crystal sizes. The linear fit of excess energy to the number of bcc modules (i.e. bcc thickness) gave a correlation coefficient of 0.99 or better, and in most cases as high as 0.9996, indicating the size of the simulation block was sufficient to represent the energy of the fcc solid solution accurately. Figure 3.6 compares the excess energy versus bcc crystal size for two different fcc crystal compositions: 0 at%Cr (Figure 3.6(a)) and 25 at%Cr (Figure 3.6(b)). The interface energy obtained by extrapolating the lines to zero bcc module is 216 mJ/m<sup>2</sup> for the case of 0 at% Cr and 211 mJ/m<sup>2</sup> for 25 at%Cr. The strain energies obtained from the slopes of the lines are  $3.9 \times 10^7$  J/m<sup>3</sup> and  $3.2 \times 10^7$  J/m<sup>3</sup>, respectively.

Figure 3.7 shows how the strain energy changes with fcc composition. The dashed line in the figure is the strain energy calculated analytically for a homogeneous strain with the elastic constants obtained by Cr potential (Table 3.1). The solid line represents a fit for strain energy obtained from the linear relation of excess energy versus thickness of bcc



(a)



(b)

Figure 3.6: The linear relationships between excess energy and the thickness of bcc crystal (expressed as the number of 42 atom modules) in the simulation block for (a) fcc crystals containing 0 at% Cr; the intercept of the line at zero bcc thickness corresponds to interface energy of  $216 \text{ mJ/m}^2$  and the slope corresponds to a strain energy of  $3.9 \times 10^7 \text{ J/m}^3$ , and (b) fcc crystals containing 25 at% Cr, the interface energy and strain energy are  $211 \text{ mJ/m}^2$  and  $3.2 \times 10^7 \text{ J/m}^3$ , respectively.

crystal. Although there are differences between the two curves, the trends are similar. Figure 3.8 shows the dependence of the interface energy on Cr concentration of the fcc crystals. The interface energy is essentially constant, decreasing only slightly from 216 to 200 mJ/m<sup>2</sup> as the Cr concentration increases from 0 to 50 at%.

The relaxed configuration of two sample simulations, one of pure Ni fcc/pure Cr bcc and the other of 25 at% Cr in fcc/pure Cr bcc, are shown in Figure 3.9 (a) and (b), respectively. The relaxation in pure Ni fcc/pure Cr bcc block (Figure 3.9 (a)) shows that the atomic relaxations are limited mostly to the two atomic layers in the vicinity of interface. These relaxations are on the order of 0.015 nm, whereas relaxations at locations away from the interface are less than 0.002 nm. The small relaxations away from the interface are indicative of a stable structure.

In the simulation block shown in Figure 3.9(b), comparatively larger relaxations are present. The larger relaxations are associated with Cr atoms in the fcc portions of the simulation block. The relaxations in the bulk crystals are still small ( $\sim 0.005$  nm) and the relaxations close to the interfaces are on the order of 0.02 nm.

### 3.3 Discussion

The interfacial energy curve for fcc composition less than 50 at% Cr is almost independent of the Cr concentration; it decreases only slightly from 216 mJ/m<sup>2</sup> at 0 at% Cr (pure Ni) to 200 mJ/m<sup>2</sup> at 48 at% Cr. In a study by Hopkins and Kossowsky [93], the fcc:bcc interface energy was measured experimentally in eutectic Ni–Cr alloy to be approximately 300 mJ/m<sup>2</sup>. The value calculated is somewhat less than this measured value, but the interface orientation and the orientation relationship are not the same as those used in this study. On the other hand, the  $(\bar{1}\bar{2}1)_f$  interfacial energy is considerably less than

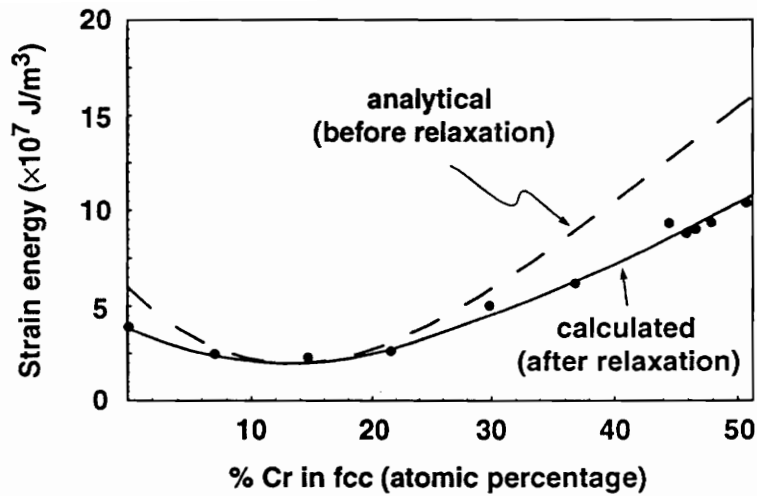


Figure 3.7: The strain energy of the bcc crystal as a function of the Cr concentration in the fcc crystals. The solid line represents a fitted curve for strain energy determined from the simulations. The dashed line represents the analytical strain energy calculated from elasticity using homogeneous coherency strains in the initial simulation block.

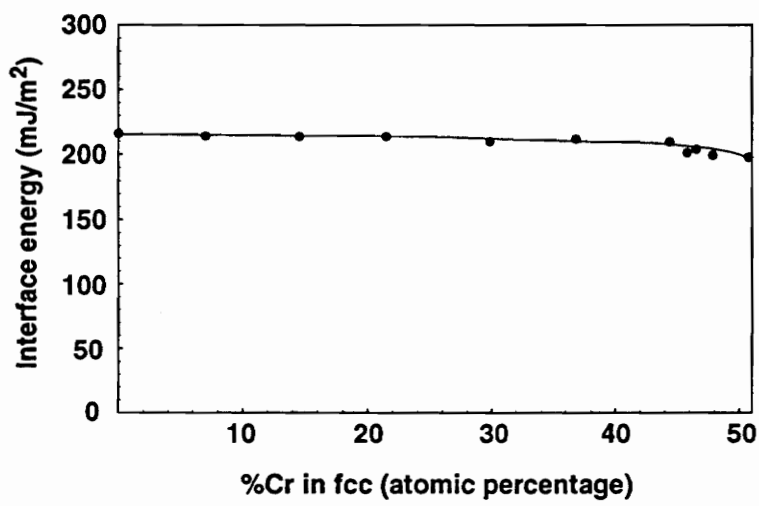
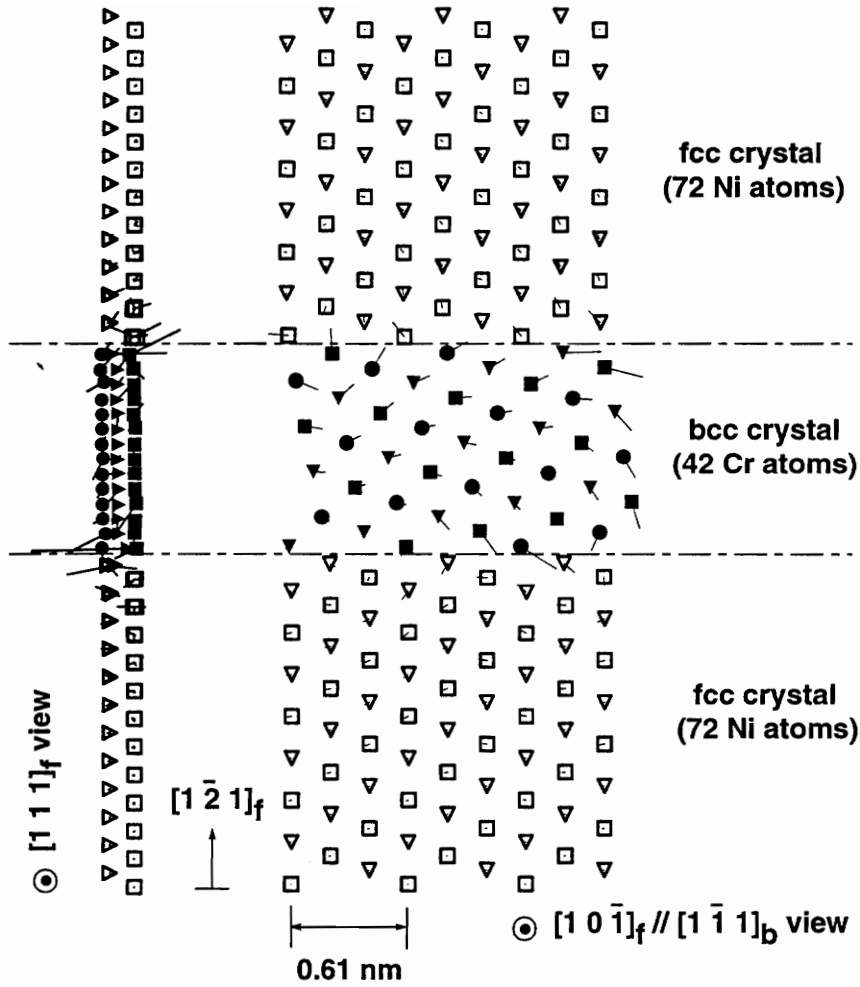


Figure 3.8: The change of interface energy with the compositions of fcc crystals.



(a)

Figure 3.9: Two views of: (a) the relaxed structure of a simulation block with pure Ni fcc crystals and pure Cr bcc crystals, and (b) the relaxation structure of a simulation block when the composition of the fcc crystals is 25 at% Cr. Different shapes (square, triangle, and circles) are used to represent atoms on different planes parallel to the paper ( $(20\bar{2})_f$  and  $(22\bar{2})_b$ ). The final positions of Ni and Cr atoms are represented by empty and filled shapes, respectively. The relative relaxations (represented by lines attached to the atoms) are enlarged 10 times to show their directions.

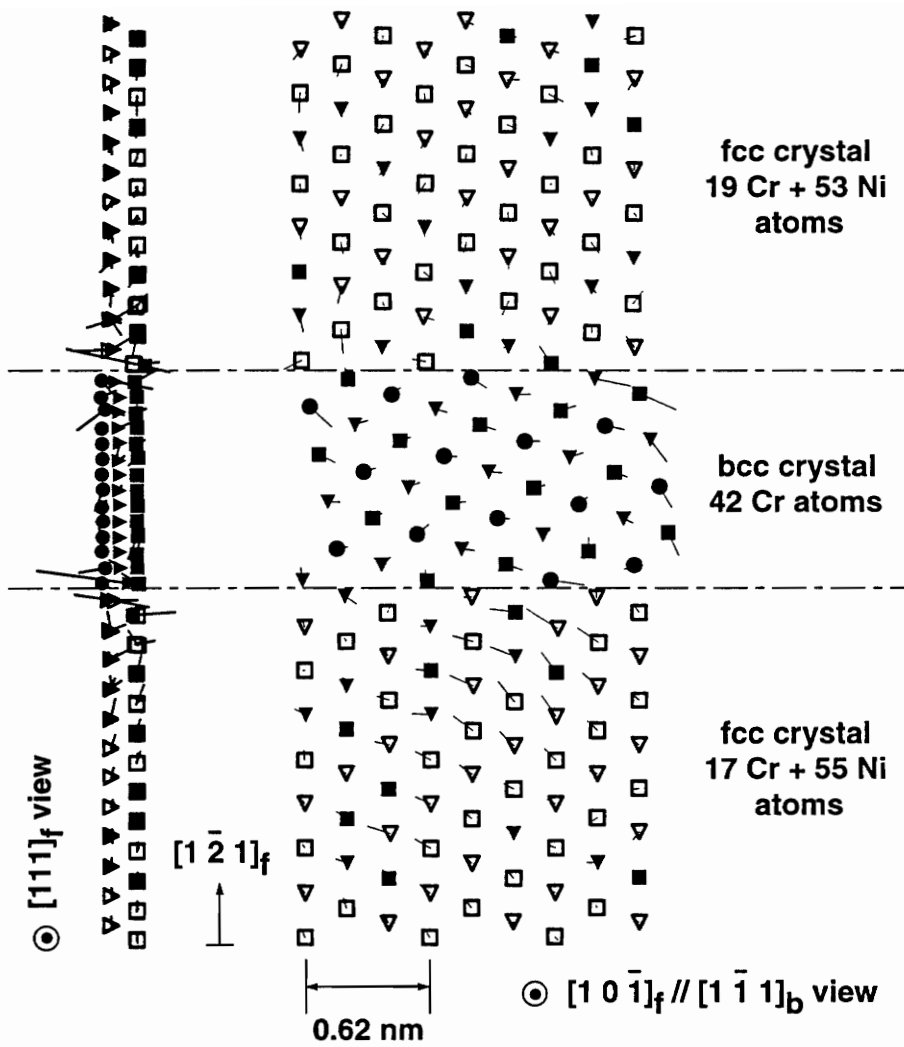


Figure 3.9(b) cont.

the measured grain boundary energies (presumably high angle boundaries) in pure Ni (866 mJ/m<sup>2</sup>) [94] and in a Ni-20 wt% Cr alloy (Ni-22 at% Cr, 756 mJ/m<sup>2</sup>) [80]. This indicates that the good atom matching and coherency across the  $(\bar{1}\bar{2}1)_f$  habit plane results in a low energy boundary.

The small change of interface energy with fcc composition (Figure 3.8) suggests that the chemical contribution in the interface energy is probably small. It is partly due to the small heat of mixing over the range of fcc composition considered (<0.07 eV). In a recent study by Farkas et al. [83], the energy of the coherent {100} interface between fcc Ni and L1<sub>2</sub> Ni<sub>3</sub>Al was calculated to be 22 mJ/m<sup>2</sup> which is close to the experimental values of 14–21 mJ/m<sup>2</sup> [95]. The energy of this fcc:L1<sub>2</sub> interface is attributed dominantly to the chemical difference on either side of the interface, and this energy is one order of magnitude lower than the interface energy currently studied. In another simulation of  $(\bar{1}\bar{2}1)_f$  fcc:bcc pure Fe interface [92], the energy was calculated to be 179 mJ/m<sup>2</sup> which contains only structure contribution and does not include chemical contribution. Since this interface energy is in the similar order of magnitude as the interface energy simulated in the current study (200–216 mJ/m<sup>2</sup>), the chemical contribution probably accounts for only 10–20% of the simulated interface energy. Most of the contribution should attribute to the structural difference between the two crystals on either side of the interface.

The change of interface structure is due to the change of fcc lattice parameters with composition. For fcc crystal containing Cr concentration from 0 to 50 at%, the lattice parameter ratio ( $a_f/a_b$ ) increases from 1.226 to 1.251. Similar lattice parameter ratios are found in several other alloys. These alloys include Fe-Cu [7], Cu-Cr [15], and dual phase stainless steels [55]. The presence of  $(\bar{1}\bar{2}1)_f$  habit plane in the bcc precipitates of these alloys indicates that these  $(\bar{1}\bar{2}1)_f$  habit planes probably all have similar matching and low interface energy.

Although the interface energy was evaluated on a forced coherent interface, the fcc:bcc interphase boundary is generally thought to be partially coherent [32]. However, TEM and HREM observations of the  $(1\bar{2}1)_f$  habit plane [45] reveal an absence of regular misfit-compensating defects other than the structural ledges included in the current simulations (Figure 3.4). Thus, the simulated interface is representative of a significant portion of the actual  $(1\bar{2}1)_f$  habit plane, and the interface energy evaluated could represent for the actual interface.

As for the difference found between the strain energy calculated from the simulations and the strain energy calculated analytically using elasticity theory (Figure 3.7). A portion of this difference may be a result of the atom relaxations at the interface. The analytical strain energy is calculated based on the homogeneous strain present in the initial simulation block. The strain energy derived from the linear relation between excess energy and the thickness of the bcc crystal represents the strain energy in the bcc crystal after the atoms in the simulation block relax. The presence of the interface and the neighboring fcc crystals may relieve the strain in the bcc crystal, since the fcc crystals are elastically softer than the bcc crystal and relatively large displacements occur at the interface between the crystals.

### 3.4 Conclusions

The interface energy of a  $(1\bar{2}1)_f$  interface between Kurdjumov-Sachs oriented fcc and bcc crystals and the coherency strain energy was calculated for Ni-Cr as a function of the Cr concentration in the fcc phase. The calculated strain energy is similar to that calculated analytically using elasticity theory. The interface energy appears to be mostly attributed to the structural difference between the fcc and bcc crystals on the interface rather than chemical contribution, therefore the  $(1\bar{2}1)_f$  interface energy varies only slightly with Cr

concentration in the fcc phase decreasing from 216 to 200 mJ/m<sup>2</sup> as the fcc composition increases from 0 to 50 at% Cr. This range of values is close to the calculated energy of the same interface in pure Fe (179 mJ/m<sup>2</sup>). It is, however, much lower than the reported grain boundary energy in some Ni–Cr alloys. Since HREM observations confirm the simulations represent a major portion of the precipitate habit plane in Ni–Cr, the actual  $(1\bar{2}1)_f$  habit plane should be a low energy interphase boundary.

## Chapter 4

# Determination of the Best-Matching Direction and Plane in Partially-Coherent Interfaces

### 4.1 Introduction

The matching of two lattices at an interphase boundary has a strong influence on the type of interfacial structure that develops, the interfacial energy, and the migration mechanism of the boundary. A number of geometric theories have been developed to treat different aspects of the lattice matching problem. The Phenomenological Theory of Martensite Crystallography (PTMC) [25] identifies an invariant (perfect matching) plane between the parent and product phases of a martensitic transformation given a lattice correspondence and lattice invariant deformation; O-lattice theory [16] determines the displacements in any interface between arbitrarily oriented phases; and the invariant line theory [17, 96], an offshoot of the PTMC, relates precipitate growth direction and habit planes to a direction of perfect matching.

When the matching of planes or directions is not perfect, it can be difficult to characterize the extent of matching. The approach described here is developed to identify the best-matching directions and plane between two arbitrarily oriented crystals.

## 4.2 Procedure

The procedure employed follows the O-lattice construction of Bollmann [16]. The crystal structures, lattice parameters and the orientation relationship between the parent and product phases must be specified. Throughout this paper, the subscripts 1 and 2 are used to represent matrices or vectors in the parent and product phases, respectively.

The orientation relationship is expressed by a pair of conjugate planes and a pair of parallel directions lying in the conjugate planes [96]. The rotation matrix,  $\mathbf{R}$ , is defined as the matrix which rotates an arbitrary direction in the product coordinates,  $\tilde{\mathbf{x}}$ , to its conjugate direction in the parent coordinates,  $\mathbf{x}$ , under the specified orientation relationship, i.e.,  $\mathbf{x} = \mathbf{R}\tilde{\mathbf{x}}$ .

The transformation matrix,  $\mathbf{A}$ , which converts the parent structure to the product with the smallest possible atomic displacements [25], is composed of the rotation matrix and the two matrices,  $\mathbf{S}_1$  and  $\mathbf{S}_2$ , whose columns are the primitive basis vectors of the parent and product phases,

$$\mathbf{x}_2 = \mathbf{A}\mathbf{x}_1 \quad \text{where} \quad \mathbf{A} = \mathbf{R}\mathbf{S}_2\mathbf{S}_1^{-1} \quad (4.1)$$

$\mathbf{S}_1$  and  $\mathbf{S}_2$  are chosen such that the transformation matrix  $\mathbf{A}$  is close to the identity matrix [51]. This meets the criterion of lattice deformation involving the smallest possible atomic displacements [25].

The misfit between the two lattices is given by the displacement the parent phase undergoes during the transformation, or:

$$\text{Misfit} = \mathbf{x}_2 - \mathbf{x}_1 = (\mathbf{A} - \mathbf{I}) \mathbf{x}_1 = \mathbf{e}_{ij} \mathbf{x}_1$$

where  $\mathbf{e}_{ij} = \mathbf{A} - \mathbf{I}$  is a displacement tensor.

Since displacements can be positive or negative depending upon whether the parent phase is stretched or compressed, the best-matching direction is found by locating the direction whose misfit is smallest in magnitude. This is done by squaring the norm of the displacement:

$$\begin{aligned} |\text{displacement of } \mathbf{x}|^2 &= (\mathbf{e}_{ij} \mathbf{x})^T (\mathbf{e}_{ij} \mathbf{x}) \\ &= \mathbf{x}^T \mathbf{M} \mathbf{x} \quad \text{where } \mathbf{M} = \mathbf{e}_{ij}^T \mathbf{e}_{ij} \end{aligned} \quad (4.2)$$

The matrix,  $\mathbf{M}$ , is symmetric. Since the square of the misfit is greater than or equal to zero for all  $\mathbf{x} \neq \mathbf{0}$ , the matrix  $\mathbf{M}$  is positive semi-definite [97].

Because  $\mathbf{M}$  is semi-definite, all three of its eigenvalues ( $\lambda_1 \leq \lambda_2 \leq \lambda_3$ ) must be larger or equal to zero [97]. It can be represented graphically by a representation quadric:  $\hat{\mathbf{x}}^T \mathbf{M} \hat{\mathbf{x}} = 1$  [98] (Figure 4.1). This ellipsoid has the property that, in any direction with unit vector  $\hat{\mathbf{x}}$ , the distance from the origin to a point on the surface is equal to  $\frac{1}{\sqrt{\hat{\mathbf{x}}^T \mathbf{M} \hat{\mathbf{x}}}}$  or the reciprocal of the misfit along  $\hat{\mathbf{x}}$ . The three eigenvectors are then the principal axes of the representation quadric each with radius equal to the reciprocal of square root of their corresponding eigenvalues.

The best-matching direction is thus the eigenvector with the smallest eigenvalue ( $\lambda_1$ ) or the least misfit. This direction corresponds to the largest radius vector of the representation ellipsoid. The best-matching plane contains the two best-matching directions and is thus the plane intersecting the representation ellipsoid with the largest cross sectional area. This plane contains the eigenvectors with eigenvalues  $\lambda_1$  and  $\lambda_2$ . Since three eigenvectors of any symmetric matrix are perpendicular to each other [98, 97], the plane normal of the best-matching plane is equal to the worst matching direction or eigenvector bearing the largest eigenvalue.

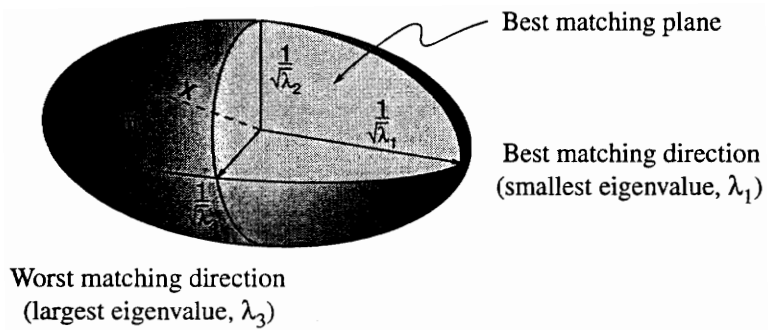


Figure 4.1: Representation quadric for the matrix  $M$ .

### 4.3 Bcc/9R interfaces

This method can be applied to arbitrary alloy systems and orientation relationships. As an example, the best-matching interface between a bcc parent and 9R product is considered. BCC/9R interfaces are found in Cr–Ni [10, 51], Cu–Zn and Cu–Al alloys [99, 100, 101, 102]. Using data applicable to a Cr–32wt%Ni alloy, the lattice parameter ratio  $a_{9R}/a_b = 0.8874$  and  $c_{9R}/a_{9R} = 7.330$  [103] where the metastable 9R Ni-rich phase precipitates from the Cr-rich bcc matrix.

The typical orientation relationship found in the bcc/9R systems [100, 99] is observed in the Cr–Ni system [10, 51]:  $(\bar{1}14)_{9R} \parallel (1\bar{1}0)_b$ , and  $[110]_{9R} \parallel [111]_b$ . To derive the rotation matrix,  $\mathbf{R}$ , the 9R structure is first expressed in a new Cartesian coordinate system. Since the 9R and fcc structures differ only in the stacking sequence of their closed-packed planes, a convenient Cartesian coordinate system is chosen such that the close-packed plane normal  $[001]_{9R}$  and the close-packed direction  $[100]_{9R}$  are expressed as  $\frac{c_{9R}}{\sqrt{6}a_{9R}}[111]_{9R,c}$  and  $\frac{1}{2}[0\bar{1}1]_{9R,c}$  in the new 9R Cartesian coordinate system (the subscript “9R,c” indicates that the vectors are expressed in the 9R Cartesian coordinate system and “9R” indicates the orthorhombic coordinate system). The rotation matrix  $\mathbf{R}$  relates the bcc and the 9R Cartesian coordinates by  $\mathbf{x}_b = \mathbf{R}\mathbf{x}_{9R,c}$  under the observed orientation relationship:

$$\mathbf{R} = \begin{bmatrix} 0.9856 & 0.1691 & 0.0072 \\ 0.1152 & -0.7013 & 0.7035 \\ 0.1240 & -0.6925 & -0.7107 \end{bmatrix}$$

The 9R primitive cell and the corresponding bcc cell require careful selection to ensure  $\mathbf{S}_1$  is close to  $\mathbf{R}\mathbf{S}_2$ . The two 9R close-packed directions,  $\frac{1}{2}[110]_{9R}$  and  $[100]_{9R}$ , are chosen as basis vectors that correspond to  $\frac{1}{2}[111]_b$  and  $[010]_b$  in bcc. The third 9R basis vector must span at least three close-packed planes to produce the correct stacking sequence [51].

The inclusion of three close-packed planes requires the inclusion of two more atoms into the primitive cell, so a 9R primitive cell contains a total of three atoms. The bcc cell must accordingly be increased in size to include the same number of atoms as the 9R cell. This is done by stacking three of the bcc primitive cells. The third 9R basis vector is thus  $[\frac{3}{2} \frac{1}{6} \frac{1}{3}]_{9R}$  and it corresponds to  $\frac{3}{2}[11\bar{1}]_b$ . By expressing  $S_2$  in the 9R Cartesian coordinate system and substituting the lattice parameters, the misfit matrix  $M$  can be found:

$$M = \begin{bmatrix} 0.0305 & -0.0269 & 0.0034 \\ -0.0269 & 0.0245 & -0.0033 \\ 0.0034 & -0.0033 & 0.0005 \end{bmatrix}$$

The eigenvectors and eigenvalues of the matrix  $M$  are:  $[0.2179 \ 0.3559 \ 0.8689]_b$  with  $\lambda_1 = 5.0 \times 10^{-6}$ ,  $[\overline{0.6521} \ \overline{0.6714} \ 0.4385]_b$  with  $\lambda_2 = 4.7 \times 10^{-4}$ , and  $[\overline{0.7450} \ 0.6671 \ \overline{0.0864}]_b$  with  $\lambda_3 = 0.055$ . Therefore, the best-matching direction is  $\sim [1 \ 1.63 \ 3.99]_b$ , and the best-matching plane is  $\sim (8.62 \ \overline{7.72} \ 1)_b$ . It is noted that both  $\lambda_1$  and  $\lambda_2$  are lower than  $10^{-3}$  and the misfit in the corresponding directions are  $\sim 0.2\%$  and  $2\%$ , respectively. This indicates that the best-matching plane is almost invariant.

#### 4.4 Discussion

Chen et al. [51] used this result to demonstrate that the best-matching plane is quite similar to the habit plane derived from the PTMC, since the required lattice invariant deformation (shear) of that theory is smaller than  $2\%$  in the Cr-32wt%Ni system. That is, a precipitate formed by a diffusion controlled mechanism can have a habit plane predicted by the PTMC if the best-matching plane is a near-invariant plane.

Similar behavior may also be applicable to other systems shown in Table 4.1. The bcc/hcp interfaces of Ti-7.15 wt%Cr [104, 106] and Zr-2.5 wt% Nb [107], and the bcc/9R

Table 4.1: Calculation and experimental results on different interfaces

	fcc/bcc in KS O.R. Ni-45 wt% Cr	bcc/hcp in Burgers O.R. Ti-7.15 wt% Cr
Best-Matching Direction Observed Growth Direction	$[\overline{1.16} \ 0.08 \ 1]_f$ $[\overline{1.16} \ 0.09 \ 1]_f$ [49]	$[4.96 \ 3 \ 3]_b$ $\sim [533]_b$ [104]
Best-Matching Plane Observed Habit Plane	$(\overline{3.4} \ 1 \ \overline{3.9})_f$ $(\overline{12}1)_f$ and $(313)_f$ to $(414)_f$ [49]	$(\overline{1} \ \overline{1} \ 1.21)_b$ $(\overline{1} \ \overline{1} \ 1.16)_b$ [105, 106]
Minimal Misfit ( $\sqrt{\lambda_1}$ )	$6.9 \times 10^{-4}$	$9.1 \times 10^{-3}$
$\sqrt{\lambda_2}$	0.148	0.021
$\sqrt{\lambda_3}$	0.352	0.19

	bcc/hcp in Potter O.R. Zr-2.5 wt% Nb	bcc/9R Cr-32 wt% Ni
Best-Matching Direction Observed Growth Direction	$[\overline{2.89} \ 1 \ \overline{2.98}]_b$ $\sim [\overline{2}12]_b$ [107]	$[1 \ 1.63 \ 3.99]_b$ —
Best-Matching Plane Observed Habit Plane	$(10 \ \overline{9} \ 13)_b$ $\sim \{111\}_b$ (Facet Plane [107])	$(8.6 \ \overline{7.7} \ 1)_b$ $(4.9 \ \overline{4.3} \ 1)_b$ [103]
Minimal Misfit ( $\sqrt{\lambda_1}$ )	$5.2 \times 10^{-4}$	$2.2 \times 10^{-3}$
$\sqrt{\lambda_2}$	0.034	0.022
$\sqrt{\lambda_3}$	0.195	0.235

interfaces of Cr-32 wt% Ni [103, 51] and Cu-Al [51] all appear to have a  $\sqrt{\lambda_2}$  no higher than 3.5%. Misfit on the best-matching planes of these systems are so small such that these interfaces are almost invariant planes. It leads these systems to form plate- or lath-like precipitates [37].

On the other hand,  $\sqrt{\lambda_2}$  in the fcc/bcc interface of the Ni-Cr alloy (Table 4.1) is as high as 15%. If in this case, factors such as the ease of misfit dislocation acquisition may determine the orientation of the habit plane rather than simply the amount of misfit. This may explain why the best-matching plane is not always the observed habit plane. Nevertheless, in recent work in Ni-Cr [60] and in Cu-Cr [15] alloys, both of which have large  $\lambda_2$ , some facets adopt the best-matching plane although these facets are not the dominant habit planes.

To apply the invariant line theory [17], the determinant of  $\mathbf{e}_{ij}$  in Equation 4.2 needs to be equal to zero. However, for a specific orientation relationship, there are only a limited number of lattice parameter ratios which fulfill this condition ( $\det |\mathbf{e}_{ij}| = 0$ ), so “near-invariant” lines are often used [55]. In these cases, the determination of the best-matching direction is a convenient way to find the near-invariant line.

## 4.5 Summary

1. An analytical method for determining the best-matching direction and the best-matching plane for arbitrary partially coherent interfaces is described. This technique provides a quantitative measure of interface matching through the intersection area of the interface and a representation quadric.

2. Whether or not the best-matching plane becomes the habit plane appears to be related to the magnitude of  $\lambda_2$ . A small  $\lambda_2$  indicates the best-matching plane is nearly

invariant and thus often agrees with the prediction of PTMC. When  $\lambda_2$  is large, factors other than interface matching, such as misfit dislocation acquisition, may have an effect on habit plane selection.

3. Determination of the best-matching direction provides an alternative method to finding the invariant line or the near-invariant line. This is particularly useful when the considered system does not have a true invariant line.

## Chapter 5

# The Role of Atomic Matching and Lattice Correspondences in the Selection of Habit Planes

### 5.1 Introduction

Precipitate habit planes and facet planes generally correspond to low energy boundaries [32, 33]. The energy of these boundaries is related to the extent to which atoms at the boundary are displaced from their normal sites in a bulk crystal [108]. Two different approaches have been used to investigate the degree of matching at interphase boundaries: a geometric matching method in which atoms of a precipitate crystal and its parent matrix crystal are superimposed on a boundary plane [36, 70, 109, 110, 111, 112], and a lattice correspondence approach in which the matrix crystal is homogeneously deformed to create the precipitate crystal [16, 17, 21, 22, 23, 24].

The geometric matching method, commonly called coincident site lattice (CSL) [113, 114] theory, has been used extensively to model grain boundary structure [115, 116]. The grains (or phases) on either side of the boundary are treated as crystals that are cleaved along the boundary plane and glued together. The extent of matching is characterized by the proportion of atoms that occupy atomic sites with respect to both crystals (coincident sites). The second method originates from the phenomenological theory of martensitic crystallography (PTMC) [21, 22, 23, 24]. The PTMC predicts the orientation of a boundary between a parent and product phase which is “invariant” or perfect matching. Under the

PTMC, the two structures intersecting at the boundary are related by a lattice correspondence or a homogeneous deformation. Each site in the parent crystal has a specific site in the product to which it is mapped by the lattice correspondence. The geometric matching method, on the other hand, places no restrictions on how atoms in the parent are displaced to become the product.

Although the atomic mechanisms associated with the two approaches are different, there are difficulties distinguishing between them experimentally. Interfaces generated with and without a lattice correspondence both have regular interfacial structure [16, 117]. In addition, both geometric matching and lattice correspondence descriptions of the interfaces can explain the growth direction of precipitates. For example, the lattice correspondence-based invariant line theory [7, 17] identifies the perfect or nearly perfect matching direction between the precipitate and matrix crystals. The kinetics of precipitate growth appear to be higher along this direction, and precipitates often elongate in this direction [7, 13, 15, 38, 55]. However, the same perfect matching direction can also be found by simply putting two crystal structures together in proper orientation relationship without using a lattice correspondence.

There appear to be cases in which the habit plane of a precipitate cannot be explained by a lattice correspondence approach, even though the plane is a good matching interface. The  $(\bar{1}\bar{2}1)_f$  habit plane of a bcc precipitate in an fcc matrix is one such example. This habit plane is found on precipitates in Ni-Cr [13], Cu-Cr [15], and dual-phase stainless steel [55]. The atomic structure of this interphase boundary has been investigated extensively in a Ni - 45 wt% Cr alloy [59, 45], and the geometric matching across the habit plane is found very good. On the other hand, the best-matching plane calculated assuming the Bain correspondence is not a particularly good matching plane and it does not coincide with the experimental habit plane [47].

There are two possible explanations for this discrepancy: (1) the Bain correspondence may not be the operative lattice correspondence, and (2) there may not be a unique lattice correspondence during the transformations. As noted by Bollmann, geometrical matching across an interphase boundary is independent of a lattice correspondence even though matching can sometimes be described by a lattice correspondence [16].

To explore these possibilities, we start by analyzing lattice correspondences other than the commonly assumed Bain correspondence [30]. Jaswon’s method [31] is employed to develop computer-generated lattice correspondences and identify the best-matching plane under each correspondence. These results are then compared with the results of the geometric matching or CSL theory.

## 5.2 Procedure and Results

The crystallographic data used in the calculations are taken from the formation of Cr-rich bcc precipitates in Ni-45 wt% Cr alloy. The fcc and the bcc crystals have a Kurdjumov-Sachs orientation relationship (K-S OR) [56]. In order to index the precipitate and matrix planes uniquely, the variant of the K-S OR selected by Luo and Weatherly [13] is employed here:

$$(1\bar{1}1)_f // (101)_b \quad \text{and} \quad [\bar{1}01]_f // [\bar{1}\bar{1}1]_b$$

The subscripts “*f*” and “*b*” represent indices for the fcc and bcc structures, respectively. The precipitate habit plane under this indexing system is  $(1\bar{2}1)_f$ . The lattice parameter ratio ( $a_f/a_b$ ) for Ni-45 wt% Cr at 1373°K is 1.255 [57, 58].

### 5.2.1 Derivation of the Transformation Matrix

Theories [25, 16] based upon a lattice correspondence define a matrix that represents the phase transformation. Following Bollmann [16], a vector expressed in the coordinates of lattice 1,  $\mathbf{X}_1$ , is transformed into a vector expressed in the coordinates of lattice 2,  $\mathbf{X}_2$ , by the relationship:

$$\mathbf{X}_2 = \mathbf{A}\mathbf{X}_1 = \mathbf{R}\mathbf{S}_2\mathbf{S}_1^{-1}\mathbf{X}_1 \quad (5.1)$$

The transformation matrix,  $\mathbf{A}$ , is described in terms of three components: a rotation matrix,  $\mathbf{R}$ , that gives rise to the orientation relationship, and  $\mathbf{S}_1$  and  $\mathbf{S}_2$  whose columns are the basis vectors of lattice 1 and 2, respectively, expressed in a common Cartesian coordinate system.

To ensure the homogeneous deformation associated with  $\mathbf{A}$  is physically realistic, the basis vectors of  $\mathbf{S}_1$  and  $\mathbf{S}_2$  must be chosen to be similar in size and orientation. Following Jaswon and Wheeler [31], this can be done by arbitrarily selecting  $\mathbf{S}_1$  and identifying an  $\mathbf{S}_2$  which, when pre-multiplied by  $\mathbf{R}$ , has column vectors close to  $\mathbf{S}_1$ . The matrix,  $\mathbf{A}$ , is then close to the identity matrix,  $\mathbf{I}$ , and the transformation involves a “least deformation” [25]. The quantity  $\mathbf{S}_2\mathbf{S}_1^{-1}$  is referred to as the “lattice correspondence”.

The least deformation constraint on the transformation matrix,  $\mathbf{A}$ , is still insufficient to lead to unique choices of  $\mathbf{S}_1$  and  $\mathbf{S}_2$ . There are infinite number of ways to choose  $\mathbf{S}_1$  and  $\mathbf{S}_2$ . In addition, the volume of the unit cells described by  $\mathbf{S}_1$  and  $\mathbf{S}_2$  need not be restricted to that of primitive unit cells. However, if there is more than one lattice point (or atom) in the unit cells of  $\mathbf{S}_1$  and  $\mathbf{S}_2$ , the excess lattice points or atoms may “shuffle” during the transformation. That is, the homogeneous deformation applies to the unit cells but not necessarily to the contents of the cells [18]. For example, transformations with a lattice correspondence between bcc and hcp require shuffling of at least one atom per unit cell,

because the smallest hcp unit cell contains two atoms.

The many possible choices of unit cells leads to many possible lattice correspondences. A computer algorithm was devised to identify all the possible correspondences associated with least deformations of unit cells smaller than  $(6 a_f^3)$  in size. The computer generates  $\mathbf{S}_1$  using all the possible combinations of non-coplanar basis vectors  $[x y z]_f$  with  $x$ ,  $y$ , and  $z$  ranging from  $-6$  to  $6$ . The corresponding  $\mathbf{S}_2$  is then chosen following the least deformation procedure described by Jaswon and Wheeler [31]. Two correspondences are derived as examples in Appendix B; the first is the well-known Bain correspondence [30, 25].

A total number of  $2 \times 10^7$  sets of  $\mathbf{S}_1$  and  $\mathbf{S}_2$  were explored. Of these correspondences,  $\sim 2000$  different lattice correspondences were identified, the Bain correspondence accounted for approximately 20% of the  $2 \times 10^7$  sets of  $\mathbf{S}_1$  and  $\mathbf{S}_2$ . That is, the computer generated  $\mathbf{S}_1$  and  $\mathbf{S}_2$  obtained by the procedure in Appendix B produced the Bain correspondence approximately four million times. However, there are 18 other correspondences that account for more than 1% of the sets of  $\mathbf{S}_1$  and  $\mathbf{S}_2$ . Moreover, the O-cell volume, which is a measure of the extent of matching in 3-dimensions [16, 51], is the same for these 19 primary lattice correspondences. Since all of these lattice correspondences are developed following Jaswon and Wheeler's procedure [31], they all meet the least deformation [25] criterion. This means that if matching in 3-dimensions is used as a criterion for choosing a lattice correspondence, the Bain correspondence is not favored over other lattice correspondences.

### 5.2.2 Best-Matching Direction and Best-Matching Plane

The best-matching direction and the best-matching plane can be identified for each lattice correspondence using a procedure described in either Reference [47] or [118]. The displacement of an atom located at  $\mathbf{X}$  undergoes during transformation from the parent to product phases is given by  $(\mathbf{A} - \mathbf{I})\mathbf{X}$ . The magnitude of this displacement is  $\sqrt{\mathbf{X}^T \mathbf{M} \mathbf{X}}$ ,

where

$$\mathbf{M} = (\mathbf{A} - \mathbf{I})^T (\mathbf{A} - \mathbf{I}) \quad (5.2)$$

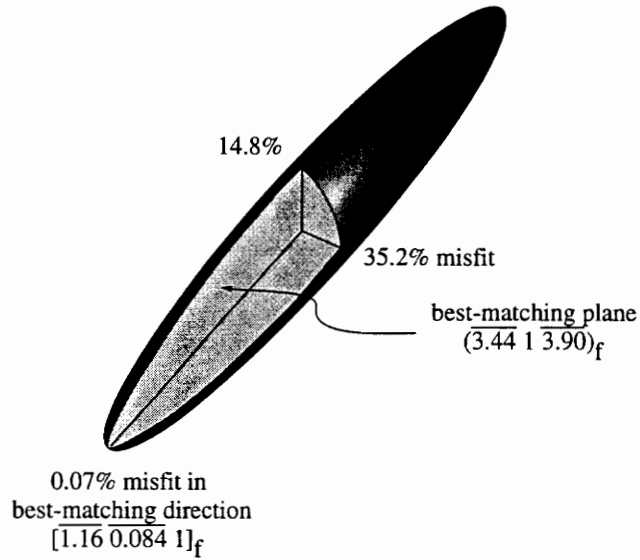
The matrix  $\mathbf{M}$  can be described visually with a “representation quadric” or ellipsoid [98]. The three eigenvectors of  $\mathbf{M}$  correspond to the three principal radius of the ellipsoid. Any radius on the ellipsoid surface is equal to  $\frac{1}{\sqrt{\hat{\mathbf{x}}^T \mathbf{M} \hat{\mathbf{x}}}}$  or the reciprocal of misfit in the radius direction (where  $\hat{\mathbf{x}}$  is the unit vector of the radius direction). For the three eigenvalues,  $0 \leq \lambda_1 \leq \lambda_2 \leq \lambda_3$ , the direction with the largest radius ( $\frac{1}{\sqrt{\lambda_1}}$ ) corresponds to the *least* misfit direction or the best-matching direction. The direction with the shortest radius ( $\frac{1}{\sqrt{\lambda_3}}$ ) gives the worst misfit direction and is the best-matching plane normal. The eigenvalue ( $\lambda_2$ ) that falls between the largest and smallest eigenvalues corresponds to the direction in the best-matching plane with the highest misfit. Thus,  $\lambda_2$  is a measure of the matching in the best-matching plane.

The best-matching directions and planes for the Bain correspondences and correspondence II (Appendix B) in Ni–Cr are shown Table 5.1. Figure 5.1(a) shows the representative ellipsoid corresponding to Bain correspondence. The ellipsoid is elongated in a single direction (a near-invariant line) since only one of the three eigenvalues is close to zero. The best-matching direction for the Bain correspondence is  $[\overline{1.16} \ \overline{0.084} \ 1.00]_f$ , which is  $\sim 5.27^\circ$  from  $[\overline{101}]_f$ . This best-matching direction agrees very well with the growth direction found experimentally and the predicted invariant line direction [49]. On the other hand, the best-matching plane (perpendicular to eigenvector 3) is approximately the  $(\overline{3.4} \ 1 \ \overline{3.9})_f$  plane which is not near to the observed  $(\overline{121})_f$  habit plane.

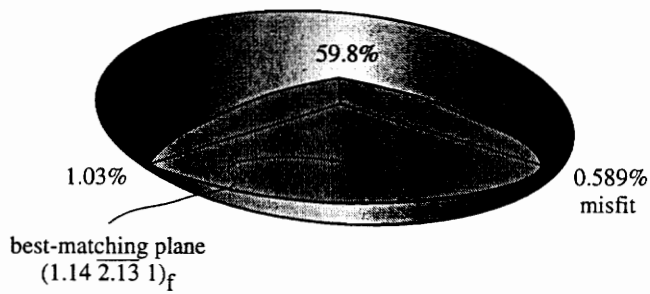
The best-matching direction for correspondence II is  $[\overline{5.03} \ \overline{2.22} \ 1]_f$ , and the best-matching plane is  $(1.14 \ \overline{2.13} \ 1)_f$ . It can be seen immediately that the best-matching direction is not close to the growth direction of the precipitate (a direction  $\sim 5.5^\circ$  from

Table 5.1: Comparison of eigenvalues and eigenvectors for Bain correspondence and lattice correspondence II. Eigenvector 1 represents the best-matching direction, and eigenvector 3 is the best-matching plane normal in each correspondence.

	Bain correspondence	Correspondence II
eigenvalue $\lambda_1$	$4.81 \times 10^{-7}$	$3.47 \times 10^{-5}$
misfit, $\sqrt{\lambda_1}$	0.069%	0.590%
eigenvector 1	$[1.16 \ 0.084 \ 1]_f$	$[5.03 \ 2.22 \ 1]_f$
eigenvalue $\lambda_2$	0.022	$1.060 \times 10^{-4}$
misfit, $\sqrt{\lambda_2}$	14.8%	1.03%
eigenvector 2	$[1 \ 11.8 \ 2.15]_f$	$[0.015 \ 1 \ 2.15]_f$
eigenvalue $\lambda_3$	0.124	0.358
misfit, $\sqrt{\lambda_3}$	35.2%	59.8%
eigenvector 3	$[3.44 \ \bar{1} \ 3.90]_f$	$[1.14 \ \bar{2.13} \ 1]_f$



(a)



(b)

Figure 5.1: The representative ellipsoids for (a) the Bain correspondence and (b) correspondence II (neither ellipsoid is drawn to scale.)

$[\bar{1}01]_f$ ), but the best-matching plane  $(1.14 \overline{2.13} 1)_f$  is within  $2^\circ$  of the experimentally observed  $(\bar{1}\bar{2}1)_f$  habit plane. The  $\sim 2^\circ$  deviation is within the experimental scatter of the habit plane, so the best-matching plane of correspondence II agrees with the experimentally observed habit plane.

It should be noted that even though the smallest misfit for correspondence II (0.59%) is not as low as that for the Bain correspondence (0.069%), the  $\lambda_2$  misfit for correspondence II (1.03%) is much lower than that for Bain correspondence (14.8%). Since the misfit corresponding to  $\lambda_2$  represents the largest misfit of the best-matching plane, correspondence II results in significantly better planar matching than the Bain correspondence. Of the 19 correspondences identified by the computer with the same O-cell volume, correspondence II had the smallest  $\lambda_2$  or the greatest degree of planar matching. The high degree of matching in the best-matching plane of correspondence II is evident from the flat appearance of the representative ellipsoid of Figure 5.1(b). The disc-shape results from two small eigenvalues (Table 5.1). This implies that the misfit in any direction contained in the best-matching plane is small.

## 5.3 Discussion

### 5.3.1 Comparison of the Bain Correspondence and Correspondence II

The Bain correspondence leads to only one good matching direction, and the observed  $(\bar{1}\bar{2}1)_f$  habit plane is not the best-matching plane. Although the  $(\bar{1}\bar{2}1)_f$  interface is one of the O-lattice facets [13, 69], the largest misfit on this plane is no smaller than 15% under this correspondence, since even the best-matching plane bears this amount of misfit. The predicted best-matching plane of the Bain correspondence does occasionally appear as a facet on the bcc precipitates in Ni-Cr [60] and Cu-Cr [15], but it is never observed to be

the major precipitate facet.

According to O-lattice theory calculations [16], the  $(\bar{1}\bar{2}1)_f$  interface should give rise to a regular network of misfit dislocations with spacing of  $\sim 1$  nm [69] if the Bain correspondence is assumed. Such misfit dislocations have not been observed by either TEM or HREM. Despite attempts to image misfit dislocations in the habit plane with the weak-beam dark field technique and HREM observations [49, 45, 59], the interface structure on  $(\bar{1}\bar{2}1)_f$  actually have revealed very few defects except occasional growth ledges and the structural ledges that generate the average habit plane.

As for correspondence II, two of the principal misfits are close to zero (0.59 % and 1.03 %) indicating the best-matching plane is almost invariant [47], or the best-matching plane is nearly an O-plane [16]. The nearly-invariant plane accounts for the fact that there are few misfit compensating defects observed on the  $(\bar{1}\bar{2}1)_f$  habit plane.

The descriptions of matching under the two correspondences are clearly different. The origin of the difference is in the choice of  $\mathbf{S}_1$  and  $\mathbf{S}_2$ . Comparing the  $\mathbf{S}_1$  used for the Bain correspondence (Equation B.2) and for correspondence II (Equation B.5), the only difference is the choice of the third basis vector:  $\frac{1}{2}[101]_f$  for the Bain correspondence and  $[333]_f$  for correspondence II. The other two basis vectors are identical.

The choice of the fcc unit cell,  $\mathbf{S}_1$ , for correspondence II includes basis vectors  $[3\ 3\ 3]_f$ ,  $[\frac{1}{2}\ \frac{1}{2}\ 0]_f$ , and  $[\bar{1}\ 0\ \frac{1}{2}]_f$  (see Appendix B). This unit cell contains three atoms. Thus when it is converted to the bcc cell ( $\mathbf{S}_2$ ), the matching of the two atoms within the cell is ignored. The homogeneous deformation implicit in lattice correspondence theories is only required of the atoms or lattice points on the corners of the unit cells. The other two atoms may shuffle independently (although the shuffles are the same in each unit cell) [18].

The two shuffling atoms in the  $\mathbf{S}_1$  cell are located at  $[111]_f$  and  $[222]_f$ . Using the K-S OR, their corresponding coordinates in bcc are  $[\overline{0.32}\ 1.67\ 1.35]_b$  and  $[\overline{0.65}\ 3.35\ 2.70]_b$ ,

respectively. These atoms in fcc shuffle to the nearest bcc atom sites:  $[\overline{0.5} \ 1.5 \ 1.5]_b$  and  $[\overline{0.5} \ 3.5 \ 2.5]_b$ . The shuffle vectors are thus  $[\overline{0.18} \ \overline{0.17} \ 0.15]_b$  and  $[0.15 \ 0.15 \ \overline{0.20}]_b$ , respectively. It can be seen in Figure 5.2 that these shuffles are almost parallel but in opposite directions. The shuffle vectors demonstrate the basic difference between the geometric matching and lattice correspondence approaches. The good geometric matching in the  $(\overline{1}\overline{2}1)_f$  plane cannot be described in terms of a lattice correspondence without including shuffles and the homogeneous deformation of the conventional Bain correspondence cannot include these shuffles.

The same procedure can be used to evaluate the misfit for the three basis vectors in  $\mathbf{S}_1$  using correspondence II. For the  $[333]_f$  atom located on the corner of the  $\mathbf{S}_1$  cell (Equation B.5), its corresponding bcc coordinates are  $[\overline{0.97} \ 5.02 \ 4.05]_b$  and the nearest bcc atom is  $[\overline{1} \ 5 \ 4]_b$ . The misfit along this direction is thus  $[0.03 \ 0.02 \ 0.05]_b$  or  $[0.04 \ \overline{0.01} \ 0.04]_f$ . The homogeneous deformation strain along this direction is  $\sim 3.3\%$ . Deformation for other basis vectors in  $\mathbf{S}_1$  is 3.03% for  $[\overline{\frac{1}{2}}0\frac{1}{2}]_f$  direction and 20.08% for  $[\frac{1}{2}\frac{1}{2}0]_f$  direction. Atoms along the  $[333]_f$  direction and the  $[\overline{\frac{1}{2}}0\frac{1}{2}]_f$  direction apparently match well. Both of these directions lie in the  $(\overline{1}\overline{2}1)_f$  plane, i.e. the  $(\overline{1}\overline{2}1)_f$  plane contains at least two directions that match well between the precipitate and matrix crystals. It can thus be considered a near coincident site lattice (near-CSL) interphase boundary. Each near-CSL cell contains three atoms since the two shuffling atoms also lie in this plane (Figure 5.2). The small number of atoms in the interface per near-CSL site, or alternatively, the high density of coincident sites is another way of describing good matching in the  $(\overline{1}\overline{2}1)_f$  habit plane.

Because the Bain correspondence implies a homogeneous deformation for all the atoms (no shuffles), the near coincidence of every third atom in the  $[111]_f$  is lost. For example, the bcc site corresponding to  $[333]_f$  is  $[063]_b$  (or  $[3.94 \ 3.01 \ 1.99]_f$  in fcc coordinates). The misfit in the  $[333]_f$  direction under the Bain correspondence is thus 26.6%, and the  $[333]_f$

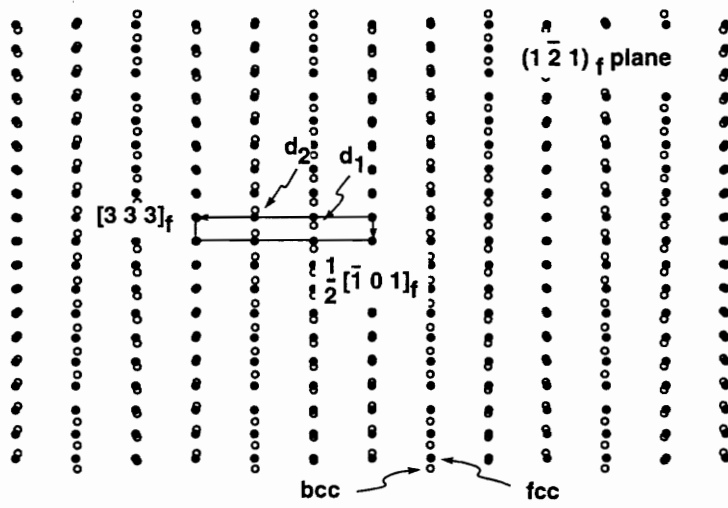


Figure 5.2: The sketch is a top view of one atomic layer of  $(1\bar{2}1)_f$ , and the outlined rectangle describes the  $\Sigma 3$  near-CSL. The filled circles represent fcc atoms and the open ones are bcc atoms. The vectors  $d_1$  and  $d_2$  (not drawn but connecting the indicated pairs of atoms) are the shuffle vectors required for the two atoms inside the unit cell of correspondence II. Their magnitudes are  $[0.18 \ 0.17 \ 0.15]_f$  and  $[0.15 \ 0.15 \ 0.20]_f$ , respectively.

direction appears to be a poor matching direction. As a consequence, the  $(\bar{1}\bar{2}1)_f$  plane becomes a poor matching plane.

The identification of a near-CSL boundary with a lattice correspondence theory can only be made if the basis vectors of the CSL are included as basis vectors of the lattice correspondence. Since the  $\mathbf{S}_1$  used in correspondence II contains two good matching basis vectors of the near-CSL, this correspondence successfully predicts the  $(\bar{1}\bar{2}1)_f$  near-CSL boundary. The Bain correspondence includes only one good matching basis vector of the near-CSL so the matching information in the  $(\bar{1}\bar{2}1)_f$  plane is lost. On the other hand, correspondence II does not yield an invariant line. The extension of the  $\mathbf{S}_1$  basis vector in the  $[333]_f$  direction results in a homogeneous deformation different from that of the Bain correspondence. It should be noted, however, that lattice correspondence II would predict an invariant line if the matching along any of the basis vectors in  $\mathbf{S}_1$  were perfect.

The objection may be raised at this point that the Bain correspondence can adequately describe precipitation in Ni-Cr if a lattice invariant shear is included to relieve misfit in the  $(\bar{1}\bar{2}1)_f$  habit plane. If such a shear were present, however, it would be manifested either by twins in the bcc precipitate or by the presence of a periodic array of glissile dislocations lying in the  $(\bar{1}\bar{2}1)_f$  habit plane. Neither are present.

It seems clear that the various crystallographic traits of precipitation in Ni-Cr cannot be accounted for by a single lattice correspondence. The Bain correspondence identifies the predominant growth direction, correspondence II “predicts” the  $(\bar{1}\bar{2}1)_f$  habit plane, and the other computer generated correspondences identify other good-matching directions and planes (none of which are as good as the best-matching direction of the Bain correspondence or the best-matching plane of correspondence II.)

What does this imply about the atomic mechanisms of precipitation in Ni-Cr? We suggest that the predominant growth direction (the elongated direction of the precipitate)

and the  $(1\bar{2}1)_f$  habit plane result from the good geometric matching in this direction and plane respectively and not from the operation of a unique lattice correspondence. As Bollmann has noted, the geometric matching of the overlapping crystal lattices determines the near-CSL independent of the existence of a lattice correspondence [16]. In other word, the good matching criterion is sufficient to determine the growth direction and the facet planes during precipitation and a lattice correspondence may not exist.

There are certainly cases of precipitation reactions whose atomic transformation mechanisms produce a lattice correspondence. The precipitation of  $\gamma'$  plates in Al–Ag [11] (an fcc–hcp transformation) or  $\Omega$  plates in Al–Cu–Mg(–Ag) [119] both have interphase boundaries that are glissile and produce the homogeneous deformation required to maintain a lattice correspondence when they move. The transformation mechanism responsible for the precipitation of bcc laths from an fcc parent matrix in Ni–Cr does not appear to result in a lattice correspondence. The observed interfacial structure of the  $[1\bar{2}1]_f$  habit plane is inconsistent with O-lattice predictions using the Bain correspondence [69, 120, 121], the predominant growth direction is not predicted by correspondence II, and several good-matching planes can be identified on a single precipitate [15, 60] but only by invoking several different correspondences. A lattice correspondence can only be maintained during a precipitation reaction if the interfacial structure contains dislocations that produce the requisite homogeneous deformation.

### 5.3.2 Diffusional and Martensitic Transformations

In martensitic transformations, all atoms follow a homogeneous deformation and a lattice invariant shear that produce an invariant habit plane. Therefore, all of the properties related to the transformations can be rationalized using a single correspondence with the deformation occurring by glissile transformation dislocations in the interphase boundary.

These properties include: the invariant plane, the orientation relationship, and magnitude of the lattice invariant shear.

A recent HREM study by Mahon et al. [73] of the  $\{252\}_f$  (or more accurately,  $\{494\}_f$  [25, 28]) habit plane of martensite in Fe-8Cr-1C provides a useful test of correspondence II. This interface appears similar to HREM interface images of the  $(\bar{1}\bar{2}1)_f$  habit plane in Ni - 45 wt% Cr [59, 45]. Mahon et al. concluded that the  $\{494\}_f$  habit plane of martensite in Fe-8Cr-1C cannot be predicted using PTMC. Similar conclusions were also found by Wayman and coworkers [28, 29]. In Sandvik and Wayman's study [29], it was suggested that two lattice invariant shears are required in order to form the invariant plane. The lattice invariant shear directions proposed were  $\langle 110 \rangle_f$  type and both of these shears are parallel to the conjugate plane or  $(1\bar{1}1)_f$  [28]. These shear directions correspond to  $[\bar{1}01](1\bar{1}1)_f$ ,  $[110](1\bar{1}1)_f$ , or  $[011](1\bar{1}1)_f$  in the current indexing convention.

Correspondence II and the lattice parameters reported by Wayman et al. [28] were employed to calculate the habit plane of martensitic transformation in the Fe-8Cr-1C alloy using the Suzuki version of the PTMC [122, 123]. One shear rather than two [29] was considered, and all three possible shear directions were tested. It is found that for the  $[110](1\bar{1}1)_f$  shear system, a 2.7% shear is needed to generate a  $(1.11 \bar{1}.95 1)_f$  habit plane; for the  $[011](1\bar{1}1)_f$  shear system, a 1.7%  $[\bar{1}12]$  shear is required to generate a  $(1.12 \bar{2}.00 1)_f$  habit plane; for the  $[\bar{1}01](1\bar{1}1)_f$  shear system, a 5.2%  $[\bar{1}12]$  shear is required to generate a  $(1.13 \bar{2}.13 1)_f$  habit plane. These predicted habit planes are within  $5.6^\circ$ ,  $5.1^\circ$ , and  $3.7^\circ$  from the observed  $(4\bar{9}4)_f$  martensitic habit plane [25, 28]. (The dilatation parameter,  $\delta$ , was not included in the calculation. If it had been, the agreement would have been even better [22, 23, 24, 28]). The orientation relationships predicted from these shear directions are all within  $0.8^\circ$  of the observed K-S OR [73]. The predicted habit planes and the predicted orientation relationships appear to coincide with the observations reasonably well.

Mahon et al. [73] proposed a lattice variant shear of  $\mathbf{b} = 1/12 [\bar{1}12]$  or  $\mathbf{b} = 1/12 [21\bar{1}]$  for each  $(1\bar{1}1)_f$  parallel atomic plane. To obtain the invariant shear component included in the transformation dislocations, one would compare the difference in the structure that contains invariant shear and that does not contain invariant shear. A simple comparison can be performed using Mahon's observation (Figure 4 in Reference [73]) and another HREM observations in Ni-45wt%Cr (Figure 3 in Reference [59].) The two transformations have similar lattice parameter ratios ( $a_f/a_b=1.255$  compared to 1.263 in Fe-8Cr-1C) and tetragonal ratios ( $c_b/a_b=1$  compared to 1.034 in Fe-8Cr-1C). Although the precipitate in Ni-45wt%Cr does not maintain a lattice correspondence, its interface matching has been shown to mimic that of correspondence II on the  $(1\bar{2}1)_f$ , therefore the comparison is proper. It was found that the two images are very similar, i.e., the magnitude of the lattice invariant shear included in Fe-8Cr-1C should not be large.

Since the calculations based upon lattice correspondence II appear to predict the crystallographic characteristics of martensitic transformation in the Fe-8Cr-1C alloy very well, it is proposed here that lattice correspondences other than the Bain correspondence can be operative in some fcc/bct martensitic reactions. The change in correspondence may also be responsible for the drastic change in the habit plane selection that occurs with small changes in the alloy compositions [25].

### 5.3.3 Summarized Procedure for the Derivation of the Smallest Near-Coincident Site Lattice Interface

Lattice correspondences can help identify directions and planes with a high density of near-coincident sites even when transformation mechanism does not produce a lattice correspondence, because different correspondences represent different aspects of geometric matching and locate the true best-matching directions and planes. The purpose of looking

up  $2 \times 10^7$  sets of  $\mathbf{S}_1$  and  $\mathbf{S}_2$  (Section 5.2.1) using all possible combinations of non-coplanar basis vectors is physically finding the smallest near-CSL boundary and the best-matching line in the considered system. For all computer-generated correspondences, the eigenvalues and eigenvectors of the matrix  $\mathbf{M}$  can be determined (Equation 5.2). The lattice correspondence that gives the lowest  $\lambda_1$  corresponds to a best-matching direction that is the true best-matching line. The true best-matching plane or the smallest near-CSL plane is then the best-matching plane determined by the lattice correspondence that has the smallest of all the  $\lambda_2$ 's. The lattice correspondence that gives rise to the smallest  $\lambda_2$  may or may not be the same as the one that gives rise to the smallest  $\lambda_1$ .

From the authors' experience, the magnitude of the misfit along the best-matching direction is normally smaller than 0.05%, and the lowest  $\sqrt{\lambda_2}$  (or highest misfit on the best-matching plane) is smaller than 3% [47]. The search size of basis vectors for computer-generated lattice correspondences should be greater than or equal to the length of the basis vectors that defines the smallest near-CSL on the habit plane.

## 5.4 Conclusions

1. The selection of the habit plane for bcc precipitate in an fcc matrix depends upon the density of near coincident sites, i.e. the geometric matching in the interface. A smaller CSL leads to better interface matching and is a candidate for a precipitate facet or habit plane.
2. Although the Bain correspondence correctly predicts the elongation direction of bcc precipitates in Ni-Cr, the precipitate habit plane is predicted successfully using a different lattice correspondence (correspondence II). It is because that the lattice correspondences provide different information about matching between the precipitate

and parent crystals in Ni-Cr and they do not represent the atomic transformation mechanism adequately. In particular, a unique lattice correspondence does not appear to be operative.

3. The growth direction and habit plane for the precipitate can be predicted by analyzing the principal misfits associated with numerous sets of lattice correspondences. The least misfit direction of all the possible principal directions identifies the best geometric-matching direction and thus the elongation direction for the precipitate. The geometric best-matching plane or the smallest near-CSL interface is the best-matching plane derived by the lattice correspondence with the least  $\lambda_2$ . The choices of the growth direction and habit plane need not be associated with the same lattice correspondence.
4. Correspondence II predicts both the  $\{494\}$  habit plane and orientation relationship for a martensitic transformation in Fe-8Cr-1C.

# Chapter 6

## Summary

This work summarizes several recent studies on the interface structures of bcc precipitates in a Ni – 45wt% Cr alloy [13, 49, 59, 60] and attempts to search for the role of atomic matching in the formation of the  $(1\bar{2}1)_f$  habit plane and a method that could predict the orientation of precipitate habit plane. The formation of habit plane is considered from defect structure, atomic structure, interface energy, and lattice correspondence points of view.

In Chapter 2, HREM observations show that the  $(1\bar{2}1)_f$  habit plane is coherent and is a good matching plane. The accommodation of structural misfit is accomplished by forming dislocations with Burgers vectors parallel to the  $(1\bar{1}1)_f$  conjugate plane, because the  $(1\bar{1}1)_f$  atomic planes are continuous across the habit plane. The one-to-one matching between  $(1\bar{1}1)_f$  and  $(101)_b$  lasts for a region of larger than 50 nm (Figure 2.7(a)). The d-spacing difference between the  $(1\bar{1}1)_f$  and  $(101)_b$  appears to be compensated by elastic strain on the  $(1\bar{2}1)_f$  habit plane. The defect structures on the habit plane vary with precipitates. No regular array of defects can be found to account for a lattice correspondence.

It is later confirmed in Chapter 5 that both the growth direction and the habit plane of the precipitate in Ni–45% Cr can be selected based upon geometric matching. Although lattice correspondences are used in the transformation theories to derive the growth direction and the habit plane, it is because that these lattice correspondences mimic the matching along the growth direction and in the habit plane. The general procedure of predicting the

precipitate growth direction and the habit plane is listed as follows:

1. Generate unit cells for the matrix and the precipitate,  $\mathbf{S}_1$  and  $\mathbf{S}_2$ , using least deformation method proposed by Jaswon and Wheeler [31].  $\mathbf{S}_1$  can be chosen by combining three arbitrary non-coplanar basis vectors. The search size of the basis vectors depends on the basis vector of the smallest coincident site lattice boundary. The  $\mathbf{S}_2$  is then selected following the procedure described in Appendix B.
2. Use the best-matching direction and plane procedure described in Chapter 4 to determine the best-matching direction and plane for each lattice correspondence considered. The eigenvalues ( $\lambda_1$ ,  $\lambda_2$ , and  $\lambda_3$ ) and eigenvectors of the  $\mathbf{M}$  matrix (Equation 5.2) can also be obtained.
3. Of all the lattice correspondences, the one that has the smallest  $\lambda_1$  gives the true best-matching direction or the precipitate growth direction, because its corresponding eigenvector has the least misfit among all correspondences considered.
4. Of all the lattice correspondences, one that has the smallest  $\lambda_2$  gives the true best-matching plane or the habit plane. If this  $\lambda_2$  is close to zero, the habit plane is a near-coincident site lattice interface.
5. More than one lattice correspondence may be used to determine the precipitate growth direction and the habit plane.

For Ni-45% Cr alloy, the Bain correspondence gives rise to the smallest  $\lambda_1$  of all lattice correspondences and predicts the precipitate growth direction. A lattice correspondence II (with the smallest  $\lambda_2$ ) is proposed in this study to predict the  $(1 \bar{2} 1)_f$  habit plane. Two lattice correspondences are employed, because they represent the matching along the growth direction and in the habit plane, respectively. It is atomic matching that controls

the selections of the growth direction and the habit plane. In the fcc:bcc transformation of Ni-45wt%Cr, a single lattice correspondence does not appear to be operative.

The energy of this  $(\bar{1}\bar{2}1)_f$  habit plane is evaluated to be  $\sim 210 \text{ mJ/m}^2$  using embedded atom method (EAM) (Chapter 3). The small change of the interface energy with fcc composition indicates that the chemical contribution is small compared to the structural contribution. Since the EAM simulated interface structure is found similar to the HREM images, the simulated energy should be representative for the actual interface energy. This energy confirms that  $(\bar{1}\bar{2}1)_f$  habit plane is a low energy interphase boundary.

## REFERENCES

- [1] A. F. Voter and S. P. Chen, in *Characterization of Defects in Materials*, R. W. Siegel, J. R. Weertman, and R. Sinclair, eds., Mat. Res. Soc. Symp. Proc. V. 82, Pittsburgh, PA, 1987, pp. 175–180.
- [2] R. Pasianot, D. Farkas, and E. J. Savino, *Phys. Rev. B*, 1991, vol. 43, pp. 6952–6961.
- [3] T. B. Massalski, *Binary Alloy Phase Diagrams*, ASM, Metals Park, OH, 1986.
- [4] G. C. Weatherly, P. Humble, and D. Borland, *Acta Metall.*, 1979, vol. 27, pp. 1815–1823.
- [5] D. J. Dyson, S. R. Keown, D. Raynor, and J. A. Whiteman, *Acta Metall.*, 1966, vol. 14, p. 867.
- [6] T. Fujii, T. Mori, and M. Kato, *Acta Metall. Mater.*, 1992, vol. 40, pp. 3413–3420.
- [7] U. Dahmen, P. Ferguson, and K. H. Westmacott, *Acta Metall.*, 1984, vol. 32, pp. 803–810.
- [8] G. C. Weatherly, *Acta Metall.*, 1971, vol. 19, pp. 181–192.
- [9] H. Emoto, R. Ni-Ikura, and M. Kikuchi, in *Phase Transformations '87*, G. W. Lorimer, ed., The Institute of Metals, London, 1988, pp. 169–173.
- [10] M. Kikuchi, A. F. Guillermet, M. Hillert, G. Cliff, and G. W. Lorimer, *Acta Metall. Mater.*, 1990, vol. 38, pp. 165–171.
- [11] J. M. Howe, U. Dahmen, and R. Gronsby, *Phil. Mag. A*, 1987, vol. 56, pp. 31–61.
- [12] U. Dahmen and K. H. Westmacott, in *Phase Transformations '87*, G. W. Lorimer, ed., The Institute of Metals, London, 1988, pp. 511–514.
- [13] C. P. Luo and G. C. Weatherly, *Acta Metall.*, 1987, vol. 35, pp. 1963–1972.
- [14] H. Zhao, K. T. Aust, and G. C. Weatherly, *Acta Metall. Mater.*, 1992, vol. 40, pp. 1961–1968.

- [15] C. P. Luo, U. Dahmen, and K. H. Westmacott, *Acta Metall. Mater.*, 1994, vol. 42, pp. 1923–1932.
- [16] W. Bollmann, *Crystal Defects and Crystalline Interfaces*, Springer-Verlag, New York, 1970.
- [17] U. Dahmen, *Scr. Metall.*, 1981, vol. 15, pp. 77–81.
- [18] J. W. Christian, *The Theory of Transformations in Metal and Alloys, Part I: Equilibrium and General Kinetic theory*, volume 15 of *International series on materials science and technology*, 2nd ed., Pergamon Press, Oxford, England, 1975.
- [19] H. I. Aaronson, T. Furuhashi, J. M. Rigsbee, W. T. Reynolds Jr., and J. M. Howe, *Metall. Trans. A*, 1990, vol. 21A, pp. 2369–2409.
- [20] H. I. Aaronson and M. G. Hall, *Metall. Mater. Trans. A*, 1994, vol. 25A, pp. 1797–1819.
- [21] M. S. Wechsler, D. S. Lieberman, and T. A. Read, *Trans. AIME*, 1953, vol. 197, pp. 1503–1515.
- [22] J. S. Bowles and J. K. Mackenzie, *Acta Metall.*, 1954, vol. 2, pp. 129–137.
- [23] J. K. Mackenzie and J. S. Bowles, *Acta Metall.*, 1954, vol. 2, pp. 138–147.
- [24] J. S. Bowles and J. K. Mackenzie, *Acta Metall.*, 1954, vol. 2, pp. 224–234.
- [25] C. M. Wayman, *Introduction to the Crystallography of Martensitic Transformation*, Macmillan Series in Materials Science, Macmillan, NY, 1964.
- [26] B. P. J. Sandvik and C. M. Wayman, *Metall. Trans. A*, 1983, vol. 14A, pp. 809–822.
- [27] B. P. J. Sandvik and C. M. Wayman, *Metall. Trans. A*, 1983, vol. 14A, pp. 823–834.
- [28] C. M. Wayman, J. E. Hanafiee, and T. A. Read, *Acta Metall.*, 1961, vol. 9, pp. 391–402.
- [29] B. P. J. Sandvik and C. M. Wayman, *Metall. Trans. A*, 1983, vol. 14A, pp. 835–844.
- [30] E. C. Bain and N. Y. Dunkirk, *Trans. AIME*, 1924, vol. 70, pp. 25–46.
- [31] M. A. Jaswon and J. A. Wheeler, *Acta Cryst.*, 1948, vol. 1, pp. 216–224.
- [32] H. I. Aaronson, in *The Decomposition of Austenite by Diffusional Processes*, V. F. Zackay and H. I. Aaronson, eds., Interscience, NY, 1962, pp. 387–549.

- [33] H. I. Aaronson, C. Laird, and K. R. Kinsman, in *Phase Transformations*, ASM, Metals Park, OH, 1970, pp. 313–396.
- [34] H. I. Aaronson and C. Laird, *Trans. AIME*, 1968, vol. 242, pp. 1437–1448.
- [35] J. M. Rigsbee and H. I. Aaronson, *Acta Metall.*, 1979, vol. 27, pp. 365–376.
- [36] J. M. Rigsbee and H. I. Aaronson, *Acta Metall.*, 1979, vol. 27, pp. 351–363.
- [37] K. H. Westmacott and U. Dahmen, *Revue Phys. Appl.*, 1986, vol. 21, pp. 757–773.
- [38] K. A. Bywater and D. J. Dyson, *Met. Sci. J.*, 1975, vol. 9, pp. 155–162.
- [39] U. Dahmen and K. H. Westmacott, in *Proceedings of an International Conference on Solid-Solid Phase Transformations*, R. F. Sekerka H. I. Aaronson, D. E. Laughlin and C. M. Wayman, eds., TMS-AIME, Warrendale, PA, 1983, pp. 433–437.
- [40] A. Perio, J. J. Bacmann, M. Suery, and A. Eberhardt, *Rev. Phys. Appl.*, 1977, vol. 78, pp. 1197–1203.
- [41] J. M. Howe, *Metall. Mater. Trans. A*, 1994, vol. 25A, pp. 1917–1922.
- [42] U. Dahmen and K. H. Westmacott, *Acta Metall.*, 1986, vol. 34, pp. 475–482.
- [43] R. C. Ecob and B. Ralph, *Acta Metall.*, 1981, vol. 29, p. 1037.
- [44] J. M. Howe and D. A. Smith, *Acta Metall. Mater.*, 1992, vol. 40, pp. 2343–2350.
- [45] J. K. Chen, G. Chen, and W. T. Reynolds Jr., Virginia Polytechnic Institute and State University, to be submitted to *Acta Metall. Mater.*, 1995.
- [46] J. K. Chen, D. Farkas, and W. T. Reynolds Jr., Virginia Polytechnic Institute and State University, to be submitted to *Acta Metall. Mater.*, 1995.
- [47] J. K. Chen and W. T. Reynolds Jr., in *Proceeding of International Conference on Solid-Solid Phase Transformations in Inorganic Materials '94*, W. C. Johnson, J. M. Howe, D. E. Laughlin, and W. A. Soffa, eds., TMS, Warendale, PA, 1994, pp. 1091–1096.
- [48] J. K. Chen and W. T. Reynolds Jr., Virginia Polytechnic Institute and State University, to be submitted to *Acta Metall. Mater.*, 1995.
- [49] C. P. Luo and G. C. Weatherly, *Phil. Mag. A*, 1988, vol. 58, pp. 445–462.

- [50] S. Wolfram, *Mathematica – A System for Doing Mathematics by Computer*, Addison-Wesley, Redwood City, CA, 1991.
- [51] J. K. Chen, T. W. Ross III, G. Chen, M. Kikuchi, and W. T. Reynolds Jr., *Metall. Mater. Trans. A*, 1994, vol. 25A, pp. 2637–2646.
- [52] J. K. Chen, C. W. Spencer, M. E. Ekstrand, G. Chen, and W. T. Reynolds Jr., accepted by *Metall. Mater. Trans. A*, 1995.
- [53] H. I. Aaronson, W. T. Reynolds Jr., G. J. Shiflet, and G. Spanos, *Metall. Trans. A*, 1990, vol. 21A, pp. 1343–1380.
- [54] H. I. Aaronson, *J. Microscopy*, 1974, vol. 102, pp. 275–300.
- [55] K. Ameyama, G. C. Weatherly, and K. T. Aust, *Acta Metall. Mater.*, 1992, vol. 40, pp. 1835–1846.
- [56] G. V. Kurdjumov and G. Sachs, *Z. Physik*, 1933, vol. 64, pp. 325–345.
- [57] W. C. Wyder and M. Hoch, *Trans. TMS-AIME*, 1963, vol. 227, pp. 588–592.
- [58] D. W. Bare, E. D. Gibson, and O. N. Carlson, *Trans. TMS-AIME*, 1964, vol. 230, pp. 934–936.
- [59] T. Furuhashi, K. Wada, and T. Maki, *Metall. Mater. Trans. A*, 1995, vol. 26A, pp. 1971–1978.
- [60] G. Chen and W. T. Reynolds Jr., to be submitted to *Acta Metall. Mater.*, 1995.
- [61] B. J. Kestel, *Ultramicroscopy*, 1984, vol. 19, pp. 213–216.
- [62] M. H. Loretto and R. E. Smallman, *Defect Analysis in Electron Microscopy*, Chapman and Hall, London, 1975.
- [63] A. K. Head, P. Humble, L. M. Clarebrough, A. J. Morton, and C. T. Forwood, *Computed Electron Micrographs and Defect Identification*, volume 7 of *Defects in Crystalline Solids*, North-Holland, Amsterdam, 1973.
- [64] C. T. Forwood and L. M. Clarebrough, *Electron Microscopy of Interfaces in Metals and alloys*, Electromicroscopy in materials science series, Adam Hilger, Bristol, England, 1991.

- [65] D. J. H. Cockayne, I. L. F. Ray, and M. J. Whelan, *Phil. Mag.*, 1969, vol. 20, Ser.8, pp. 1265–1270.
- [66] D. J. H. Cockayne, *J. Microscopy*, 1973, vol. 98, Pt. 2, pp. 116–134.
- [67] C. P. Luo, *An Electron Microscope Study of the Crystallography and Interfacial Structure of Precipitates in A Ni-45%Cr Alloy*, PhD thesis, University of Toronto, 1986.
- [68] G. Chen, J. M. Howe, and W. T. Reynolds Jr., in *Proceeding of International Conference on Solid-Solid Phase Transformations in Inorganic Materials '94*, W. C. Johnson, J. M. Howe, D. E. Laughlin, and W. A. Soffa, eds., TMS, Warrendale, PA, 1994, pp. 291–296.
- [69] G. C. Weatherly and W.-Z. Zhang, *Metall. Mater. Trans. A*, 1994, vol. 25A, pp. 1865–1874.
- [70] M. G. Hall, J. M. Rigsbee, and H. I. Aaronson, *Acta Metall.*, 1986, vol. 34, pp. 1419–1431.
- [71] M. G. Hall and H. I. Aaronson, *Acta Metall.*, 1986, vol. 34, pp. 1409–1418.
- [72] F. C. Frank and J. H. Van Der Merwe, *Proc. Roy. Soc.*, 1949, vol. A198, pp. 205–216.
- [73] G. J. Mahon, J. M. Howe, and S. Mahajan, *Phil. Mag. Lett.*, 1989, vol. 59, pp. 273–279.
- [74] J. P. Hirth, B. Pieraggi, and R. A. Rapp, *Acta Metall. Mater.*, 1995, vol. 43, pp. 1065–1073.
- [75] S. V. Kamat and J. P. Hirth, *Acta Metall. Mater.*, 1994, vol. 42, pp. 3767–3772.
- [76] C. B. Carter and S. M. Holmes, *Phil. Mag.*, 1977, vol. 35, pp. 1161–1172.
- [77] D. J. H. Cockayne, M. L. Jenkins, and I. L. F. Ray, *Phil. Mag. A*, 1971, vol. 24, Ser.8, pp. 1383–1392.
- [78] G. Chen, J. K. Chen, J. K. Lee, and W. T. Reynolds Jr, *Metall. Mater. Trans. A*, 1994, vol. 25, pp. 2073–2082.
- [79] P. C. J. Gallagher, *Metall. Trans.*, 1970, vol. 1, pp. 2429–2461.
- [80] L. E. Murr, R. J. Horylev, and G. I. Wong, *Surface Sci.*, 1971, vol. 26, pp. 184–196.
- [81] M. S. Daw and M. I. Baskes, *Phys. Rev. B*, 1984, vol. 29, pp. 6443–6453.

- [82] M. J. Mills and M. S. Daw, in *High Resolution Electron Microscopy of Defects in Materials*, R. Sinclair, D. J. Smith, and U. Dahmen, eds., Mat. Res. Soc. Symp. Proc. V. 183, Pittsburgh, PA, 1990, pp. 15–26.
- [83] D. Farkas, M. F. de Campos, R. M. de Souza, and H. Goldenstein, *Scr. Metall. Mater.*, 1994, vol. 30, pp. 367–371.
- [84] M. J. Norgett, R. C. Perrin, and E. J. Savino, *J. Phys. F. Met. Phys.*, 1972, vol. 2, pp. L73–L75.
- [85] G. Simmons and H. Wang, *Single Crystal Elastic Constants and Calculated Aggregate Properties: a Handbook*, M.I.T. Press, Cambridge, MA, 1971.
- [86] R. A. Johnson, in *Many Atom Interactions in Solids*, Springer Proc. in Phys., vol. 48, 1990, pp. 85–90.
- [87] D. Farkas, B. Mutasa, C. Vaill e, and K. Ternes, *Modelling and Simulation in Materials Science and Engineering*, 1994, vol. 3, pp. 201–214.
- [88] R. R. Hultgren, P. P. Desai, P. T. Hawkins, M. Gleiser, and K. K. Kelley, *Selected Values of the Thermodynamic Properties of Binary Alloys*, American Society for Metals, Metals Park, OH, USA, 1973.
- [89] A. Taylor and K. G. Hinton, *J. Inst. Metals.*, 1952–53, vol. 81, pp. 169–180.
- [90] B. W. Roberts and R. A. Swalin, *Trans. AIME, J. Metals*, 1957, vol. , pp. 845–847.
- [91] Y. Z. Vintaykin, V. P. Itkin, B. M. Mogutnov, and G. G. Urushadze, *Sov. Phys. Doklady*, 1969, vol. 14, pp. 263–265.
- [92] J. K. Chen, D. Farkas, and W. T. Reynolds Jr., in *Proceeding of International Conference on Solid-Solid Phase Transformations in Inorganic Materials '94*, W. C. Johnson, J. M. Howe, D. E. Laughlin, and W. A. Soffa, eds., TMS, Warrendale, PA, 1994, pp. 1097–1102.
- [93] R. H. Hopkins and R. Kossowsky, *Acta Metall.*, 1971, vol. 19, pp. 203–211.
- [94] L. E. Murr, *Interfacial Phenomena in Metals and Alloys*, Addison-Wesley, Reading, MA, 1975.
- [95] A. J. Ardell and R. B. Nicholson, *J. Phys. Chem. Solids*, 1966, vol. 27, p. 1793.
- [96] U. Dahmen, *Acta Metall.*, 1982, vol. 30, pp. 63–73.

- [97] B. N. Parlett, *The Symmetric Eigenvalue Problem*, Prentice-Hall, Englewood Cliffs, 1980.
- [98] J. F. Nye, *Physical Properties of Crystals*, Oxford University Press, London, 1957.
- [99] K. Chattopadhyay and H. I. Aaronson, *Acta Metall.*, 1986, vol. 34, pp. 713–720.
- [100] I. Cornelis and C. M. Wayman, *Acta Metall.*, 1974, vol. 22, pp. 301–311.
- [101] I. Cornelis and C. M. Wayman, *Scr. Metall.*, 1973, vol. 7, pp. 579–590.
- [102] L. Delaey and I. Cornelis, *Acta Metall.*, 1970, vol. 18, pp. 1061–1066.
- [103] M. Kikuchi, presentation on *The Roles of Shear and Diffusion in the Formation of Plate-Shaped Transformation Products* symposium held in Kona, HI, USA, 1992.
- [104] T. Furuhashi, J. M. Howe, and H. I. Aaronson, *Acta Metall. Mater.*, 1991, vol. 39, pp. 2873–2886.
- [105] T. Makino, K. Igarashi, T. Furuhashi, and T. Maki, in *Proceedings of International Conference on Solid-Solid Phase Transformations in Inorganic Materials '94*, W. C. Johnson, J. M. Howe, D. E. Laughlin, and W. A. Soffa, eds., TMS-AIME, Warrendale, PA, 1994, pp. 207–212.
- [106] E. S. K. Menon and H. I. Aaronson, *Acta Metall.*, 1986, vol. 34, pp. 1963–1973.
- [107] V. Perovic and G. C. Weatherly, *Acta Metall.*, 1989, vol. 37, pp. 813–821.
- [108] A. P. Sutton and R. W. Balluffi, *Acta Metall.*, 1987, vol. 35, pp. 2177–2201.
- [109] T. Furuhashi and H. I. Aaronson, *Acta Metall. Mater.*, 1991, vol. 39, pp. 2857–2872.
- [110] J. H. Van Der Merwe, *Phil. Mag. A*, 1982, vol. 45, pp. 127–143.
- [111] J. H. Van Der Merwe, *Phil. Mag. A*, 1982, vol. 45, pp. 145–157.
- [112] J. H. Van Der Merwe, *Phil. Mag. A*, 1982, vol. 45, pp. 159–170.
- [113] W. T. Read and W. Shockley, *Phys. Rev.*, 1950, vol. 78, p. 225.
- [114] N. F. Mott, *Proc. Phys. Soc.*, 1948, vol. 60, p. 391.
- [115] R. W. Balluffi, A. Brokman, and A. H. King, *Acta Metall.*, 1982, vol. 30, pp. 1453–1470.

- [116] V. Vitek, A. P. Sutton, D. A. Smith, and R. C. Pond, in *Grain-Boundary Structure and Kinetics*, R. W. Balluffi, ed., ASM, Milwaukee, WI, 1979, pp. 115–148.
- [117] R. W. Balluffi, *Metall. Trans. A*, 1982, vol. 13A, pp. 2069–2095.
- [118] W. Z. Zhang and G. R. Purdy, *Phil. Mag. A*, 1993, vol. 68, pp. 279–290.
- [119] R. W. Fonda, W. A. Cassada, and G. J. Shiflet, *Acta Metall. Mater.*, 1992, vol. 40, pp. 2539–2546.
- [120] D. A. Smith, K. M. Knowles, H. I. Aaronson, and W. A. T. Clark, in *Proc. Int'l Conf. Solid-Solid Phase Transformations*, H. I. Aaronson, D. E. Laughlin, R. F. Sekerka, and C. M. Wayman, eds., Mat. Res. Soc. Symp. Proc. V. 291, Pittsburgh, PA, 1982, pp. 587–590.
- [121] W. Bollmann, *Phys. Stat. Sol.*, 1974, vol. A21, pp. 543–550.
- [122] H. Suzuki, in *Physical Properties of Metals (in Japanese)*, J. Yamashita and T. Suzuki, eds., Syokabo, Tokyo, 1968, pp. 394–420.
- [123] S. Kajiwara, *Trans. JIM*, 1976, vol. 17, pp. 435–446.
- [124] M. B. Boisen Jr. and G. V. Gibbs, *Mathematical Crystallography*, volume 15 of *Reviews in Mineralogy*, Miner. Soc. Amer., Washington, D.C., 1990.

## Appendix A

### Derivation of Crystallographic Orientation Relation with Double Tilt Holder

In this appendix, an expression is derived to relate the angle readings from a double tilt specimen holder to the crystallographic orientations. The primary application of this tool is for indexing crystallographic orientations especially when unambiguous indexing is required as in the case of trace analysis and orientation relationship analysis.

The double tilt holder can be thought to consist of two perpendicular rotation axes, namely  $x$  and  $y$ . The foil normal or the beam direction corresponding to the untilted condition is assigned  $[0\ 0\ 1]$  relative to a fixed Cartesian coordinate system tied to the specimen holder. A rotation about  $x$  axis by a  $\theta_x$  angle can be represented by:

$$\begin{bmatrix} 1 & 0 & 0 \\ 0 & \cos \theta_x & -\sin \theta_x \\ 0 & \sin \theta_x & \cos \theta_x \end{bmatrix}$$

Similarly, the rotation about the  $y$  axis by an angle,  $\theta_y$ , is represented by

$$\begin{bmatrix} \cos \theta_y & 0 & \sin \theta_y \\ 0 & 1 & 0 \\ -\sin \theta_y & 0 & \cos \theta_y \end{bmatrix}$$

After both rotations about the  $x$  and  $y$  axes, the beam direction is rotated from  $[0\ 0\ 1]$  to  $[\sin \theta_y \ -\cos \theta_y \sin \theta_x \ \cos \theta_y \cos \theta_x]$  direction.

For two specimen orientations with specimen holder angle readings of  $(\theta_{x_1}, \theta_{y_1})$  and  $(\theta_{x_2}, \theta_{y_2})$ , it is possible to obtain beam directions in the holder's coordinate system. The first is at  $[\sin \theta_{y_1} \quad -\cos \theta_{y_1} \sin \theta_{x_1} \quad \cos \theta_{y_1} \cos \theta_{x_1}]$ , and the other is at  $[\sin \theta_{y_2} \quad -\cos \theta_{y_2} \sin \theta_{x_2} \quad \cos \theta_{y_2} \cos \theta_{x_2}]$ . Since both of these are unit vectors, the angle ( $\Phi$ ) between the two directions is conveniently obtained by taking the dot product between them:

$$\Phi = \cos^{-1} (\sin \theta_{y_1} \sin \theta_{y_2} + \cos \theta_{y_1} \cos \theta_{y_2} \cos (\theta_{x_1} - \theta_{x_2})) \quad (\text{A.1})$$

If more than three non-coplanar zones are used, it is possible to derive the coordinate transformation matrix between the crystallographic coordinate system and the specimen holder's coordinate system. Once this transformation is obtained, the foil normal in crystal coordinate can be estimated corresponding to  $[0 \ 0 \ 1]$  in specimen holder's coordinate system. It also helps to determine the orientation relationships, since the rotation between two crystals can be obtained through the coordinate transformation matrix of each individual crystal.

Following is a demonstration of the procedure for determining the coordinate transformation matrix between a cubic crystal and the specimen holder's coordinate system. For at least three non-coplanar crystallographic zones whose unit vectors are  $X_i$ , each has a corresponding  $\tilde{X}_i$  in the holder's coordinate system. The  $\tilde{X}_i$  is  $[\sin \theta_{y,i} \quad -\cos \theta_{y,i} \sin \theta_{x,i} \quad \cos \theta_{y,i} \cos \theta_{x,i}]$  where  $\theta_{x,i}$  and  $\theta_{y,i}$  are the angle readings for  $X_i$  zone. A translation matrix,  $\mathbf{R}$  relates the coordinate systems such that  $X_i = \mathbf{R}\tilde{X}_i$ . If  $\mathbf{X}$  and  $\tilde{\mathbf{X}}$  represent matrices containing three or more  $X_i$ 's and  $\tilde{X}_i$ 's as their column vectors, respectively,  $\mathbf{R}$  is derived as :

$$\mathbf{R} = \mathbf{X}\tilde{\mathbf{X}}^{\mathbf{T}}(\tilde{\mathbf{X}}\tilde{\mathbf{X}}^{\mathbf{T}})^{-1} \quad (\text{A.2})$$

It should be pointed out that this is a regression procedure for an overdetermined condition, i.e. there are more than three zones and their coordinates in tilter's system being used to

derive a  $3 \times 3$   $\mathbf{R}$  matrix which best fits as a coordinate transformation matrix. In other word, both  $\mathbf{X}$  and  $\tilde{\mathbf{X}}$  are matrices of  $3 \times m$ , where  $m > 3$ . In the case of exact three zones are used, both  $\mathbf{X}$  and  $\tilde{\mathbf{X}}$  are  $3 \times 3$  matrices. The derivation of  $\mathbf{R}$  can be simply written as  $\mathbf{X}\tilde{\mathbf{X}}^{-1}$ .

If the procedure is correctly followed, the determinant of  $\mathbf{R}$  matrix should be close to unity, since it is a pure rotation and does not involve a volume change. The transformed crystallographic orientations from holder's coordinate system using the transformation matrix are usually within  $\sim 2^\circ$  error, and the deviation decreases even further with increasing number of crystallographic zones used for calibrating the coordinate transformation. The derivation of coordinate for non-cubic crystal system follows the same procedure except the crystallographic zones,  $X_i$ , are replaced by  $\mathbf{T}X_i$  where the matrix  $\mathbf{T}$  transforms crystal coordinates to a Cartesian coordinate system.

To determine the orientation relationship between crystal A and crystal B, the two rotation matrices  $\mathbf{R}_A$  and  $\mathbf{R}_B$  are first obtained for the two crystals. Since  $\mathbf{X}_A = \mathbf{R}_A \tilde{\mathbf{X}}$  and  $\mathbf{X}_B = \mathbf{R}_B \tilde{\mathbf{X}}$ , the relation between  $\mathbf{X}_A$  and  $\mathbf{X}_B$  can immediately be derived as  $\mathbf{X}_B = \mathbf{R}_B \mathbf{R}_A^{-1} \mathbf{X}_A$ . The matrix  $\mathbf{R}_B \mathbf{R}_A^{-1}$  contains the orientation relationship information relating crystals A and B.

A worked example for unambiguous indexing in current study is given as follows. Suppose a bcc  $\langle 100 \rangle_b$  zone is obtained at a tilting angle of  $(6^\circ, 13^\circ)$ , and an fcc  $\langle 110 \rangle_f$  zone at  $(10^\circ, 16^\circ)$ , the angle between these zones is calculated to be  $5^\circ$  using Equation A.1. According to the K-S OR overlapped fcc/bcc stereographic projections, the only possible indexing for these zones are  $[010]_b$  and  $[110]_f$  or  $[0\bar{1}0]_b$  and  $[\bar{1}\bar{1}0]_f$  which are both  $5.26^\circ$  from each other. These two possibilities can further be distinguished by comparing the relative positions of these zones and their nearby Kikuchi lines of the two phases.

## Appendix B

### Derivation of Lattice Correspondences

The approach of Jaswon and Wheeler [31] is used to choose a set of  $\mathbf{S}_1$  and  $\mathbf{S}_2$  unit cells such that the transformation matrix,  $\mathbf{A} = \mathbf{R}\mathbf{S}_2\mathbf{S}_1^{-1}$  (Equation 5.1), is close to the identity matrix. Mathematically, this requires  $\mathbf{R}^{-1}\mathbf{S}_1$  to be similar to  $\mathbf{S}_2$ .

The matrix,  $\mathbf{R}$ , is derived first; it can be thought of as a coordinate transformation that describes the orientation relationship between fcc and bcc. A unit direction,  $\hat{\mathbf{x}}_f$ , in fcc coordinates is obtained by a rotation from a corresponding unit direction  $\hat{\mathbf{x}}_b$  in bcc coordinates, i.e.,  $\hat{\mathbf{x}}_f = \mathbf{R}\hat{\mathbf{x}}_b$ . Three parallel vectors between the fcc and bcc phases under the K-S OR can be used to find this relation. Since  $[1\bar{1}1]_f \parallel [101]_b$ ,  $[\bar{1}01]_f \parallel [\bar{1}\bar{1}1]_b$ , and  $[\bar{1}2\bar{1}]_f \parallel [\bar{1}2\bar{1}]_b$ , the three equations between the unit vectors in these directions can be written compactly as:

$$\begin{bmatrix} 1/\sqrt{3} & -1/\sqrt{2} & -1/\sqrt{6} \\ -1/\sqrt{3} & 0 & -2/\sqrt{6} \\ 1/\sqrt{3} & 1/\sqrt{2} & -1/\sqrt{6} \end{bmatrix}_f = \mathbf{R} \begin{bmatrix} 1/\sqrt{2} & -1/\sqrt{3} & 1/\sqrt{6} \\ 0 & -1/\sqrt{3} & -2/\sqrt{6} \\ 1/\sqrt{2} & -1/\sqrt{3} & -1/\sqrt{6} \end{bmatrix}_b$$

or

$$\mathbf{R} = \begin{bmatrix} 0.6498 & 0.7416 & 0.1667 \\ -0.7416 & 0.6667 & -0.0749 \\ -0.1667 & -0.0749 & 0.9832 \end{bmatrix} \quad (\text{B.1})$$

Next, a choice is made for  $\mathbf{S}_1$  (the three basis vectors for the fcc unit cell). One choice is three of the 12 nearest neighbors along the  $\frac{1}{2} \langle 110 \rangle_f$  directions. For the three non-

coplanar basis vectors,  $\frac{1}{2}[110]_f$ ,  $\frac{1}{2}[\bar{1}01]_f$ , and  $\frac{1}{2}[101]_f$ ,  $\mathbf{S}_1$  becomes:

$$\mathbf{S}_1 = \mathbf{a}_f \begin{bmatrix} \frac{1}{2} & -\frac{1}{2} & \frac{1}{2} \\ \frac{1}{2} & 0 & 0 \\ 0 & \frac{1}{2} & \frac{1}{2} \end{bmatrix} \quad (\text{B.2})$$

These vectors can be translated into bcc coordinates using  $\mathbf{R}$ :

$$\mathbf{R}^{-1}\mathbf{S}_1 = \mathbf{a}_b \begin{bmatrix} -0.058 & -0.512 & 0.303 \\ 0.884 & -0.512 & 0.418 \\ 0.058 & 0.512 & 0.722 \end{bmatrix}$$

This indicates the vectors  $\frac{1}{2}[110]_f$ ,  $\frac{1}{2}[\bar{1}01]_f$ , and  $\frac{1}{2}[101]_f$  expressed in bcc coordinates are  $[\bar{0}.058 \ 0.884 \ 0.048]_b$ ,  $[\bar{0}.512 \ \bar{0}.512 \ 0.512]_b$ , and  $[0.303 \ 0.418 \ 0.722]_b$  under the K-S OR. The closest atoms in the bcc phase to these fcc atoms are selected for  $\mathbf{S}_2$ . For example,  $[\bar{0}.058 \ 0.884 \ 0.048]_b$  is close to  $[010]_b$ ,  $[\bar{0}.512 \ \bar{0}.512 \ 0.512]_b$  is close to  $[\frac{\bar{1}}{2} \ \frac{\bar{1}}{2} \ \frac{1}{2}]_b$ , and  $[0.303 \ 0.418 \ 0.722]_b$  is close to  $[\frac{1}{2} \ \frac{1}{2} \ \frac{1}{2}]_b$ .  $\mathbf{S}_2$  is thus

$$\mathbf{S}_2 = \mathbf{a}_b \begin{bmatrix} 0 & -\frac{1}{2} & \frac{1}{2} \\ 1 & -\frac{1}{2} & \frac{1}{2} \\ 0 & \frac{1}{2} & \frac{1}{2} \end{bmatrix}$$

In principle, this choice should result in a small atom displacements during transformation of fcc to bcc, or equivalently, a transformation matrix  $\mathbf{A} = \mathbf{R}\mathbf{S}_2\mathbf{S}_1^{-1}$  close to  $\mathbf{I}$ . For this case, the lattice correspondence,  $\mathbf{S}_2\mathbf{S}_1^{-1}$ , is:

$$\text{lattice correspondence} = \mathbf{S}_2\mathbf{S}_1^{-1} = \frac{\mathbf{a}_b}{\mathbf{a}_f} \begin{bmatrix} 1 & -1 & 0 \\ 1 & 1 & 0 \\ 0 & 0 & 1 \end{bmatrix} \quad (\text{B.3})$$

This lattice correspondence is commonly known as Bain correspondence [30, 25].

The lattice parameter ratio ( $a_f/a_b$ ) for Ni-45 wt% Cr at 1373°K is 1.255 [57, 58]. The transformation matrix for this ratio and the Bain correspondence is:

$$\mathbf{A} = \mathbf{R}\mathbf{S}_2\mathbf{S}_1^{-1} = \begin{bmatrix} 1.1087 & 0.0731 & 0.1328 \\ -0.0597 & 1.1221 & -0.0595 \\ -0.1945 & 0.0731 & 0.7834 \end{bmatrix} \quad (\text{B.4})$$

A second possible correspondence can be obtained by selecting basis vectors for  $\mathbf{S}_1$  as  $[\frac{1}{2} \frac{1}{2} 0]_f$ ,  $[\frac{1}{2} 0 \frac{1}{2}]_f$ , and  $[3 3 3]_f$ , i.e.

$$\mathbf{S}_1 = \mathbf{a}_f \begin{bmatrix} \frac{1}{2} & -\frac{1}{2} & 3 \\ \frac{1}{2} & 0 & 3 \\ 0 & \frac{1}{2} & 3 \end{bmatrix} \quad (\text{B.5})$$

Using the same rotation matrix as before,

$$\mathbf{R}^{-1}\mathbf{S}_1 = \mathbf{a}_b \begin{bmatrix} -0.058 & -0.512 & -0.973 \\ 0.883 & -0.512 & 5.02 \\ 0.058 & 0.512 & 4.047 \end{bmatrix}$$

and bcc sites close to these coordinates are chosen for  $\mathbf{S}_2$ :

$$\mathbf{S}_2 = \mathbf{a}_b \begin{bmatrix} 0 & -\frac{1}{2} & -1 \\ 1 & -\frac{1}{2} & 5 \\ 0 & \frac{1}{2} & 4 \end{bmatrix}$$

The lattice correspondence thus obtained becomes

$$\mathbf{S}_2\mathbf{S}_1^{-1} = \frac{\mathbf{a}_b}{\mathbf{a}_f} \begin{bmatrix} \frac{2}{3} & -\frac{2}{3} & -\frac{1}{3} \\ \frac{2}{3} & \frac{4}{3} & -\frac{1}{3} \\ \frac{1}{3} & -\frac{1}{3} & \frac{4}{3} \end{bmatrix} \quad \text{and} \quad \mathbf{A} = \begin{bmatrix} 0.7834 & 0.3984 & -0.1925 \\ -0.0597 & 1.1221 & -0.0597 \\ 0.1328 & -0.2522 & 1.1087 \end{bmatrix} \quad (\text{B.6})$$

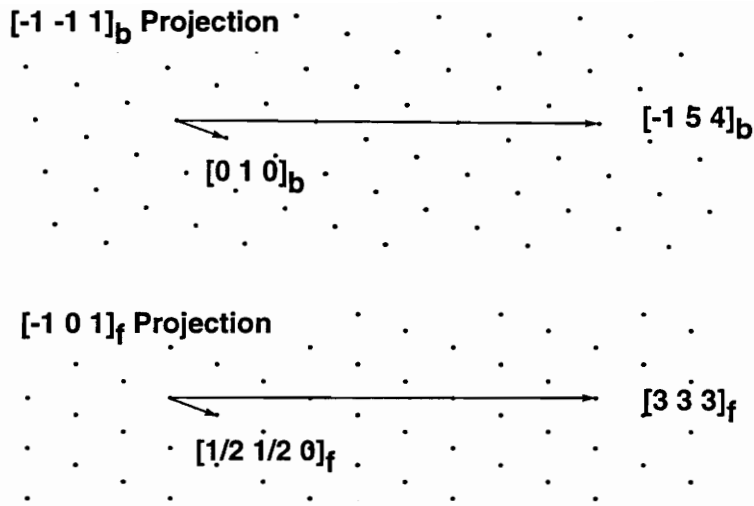


Figure B.1: A schematic of lattice correspondence II. The bcc crystal (top) and fcc crystal (bottom) are in the Kurdjumov-Sachs orientation relationship and the  $[\bar{1}01]_f$  and  $[\bar{1}\bar{1}1]_b$  directions are perpendicular to the plane of the projection. Two of the three sets of correspondence vectors are shown:  $[\bar{1}54]_b$  and  $[333]_f$ ;  $[010]_b$  and  $[\frac{1}{2}\frac{1}{2}0]_f$ ; the third set is perpendicular to the projection:  $[\frac{1}{2}\frac{1}{2}\frac{1}{2}]_b$  and  $[\frac{1}{2}0\frac{1}{2}]_f$ .

Figure B.1 shows the similarity between  $\mathbf{S}_1$  and  $\mathbf{S}_2$  chosen for this lattice correspondence. This lattice correspondence, referred to here as correspondence II, is apparently very different from the Bain correspondence (Equation B.3).

Chen et al. [51] used the volume of O-lattice [16] as a measure for three-dimensional matching. The column vectors of  $(\mathbf{I} - \mathbf{A}^{-1})^{-1}$  gives the basis vectors of the O-lattice [16], and its determinant represents the volume of the O-lattice unit cell. The longer the O-lattice vectors are, the larger the volume of the O-lattice unit cell and the better the precipitate and matrix crystal lattices match each other [16]. The determinant of  $(\mathbf{I} - \mathbf{A}^{-1})^{-1}$  is thus an indicator of how well the two lattices match. For both the Bain correspondence and correspondence II, the volume of the O-lattice unit cell is  $27892 a_f^3$ .

## Appendix C

### Program List and Selected Computer Programs

The following contains a list of programs developed or modified for the current dissertation. Some selected programs are included in the second part of this Appendix. Due to the limited space, the codes included are chosen among those used mostly for general TEM groups and for whom are interested in applying the best-matching direction and the best-matching plane procedures [47, 48].

#### C.1 List of programs

1. *VectorAnalysis.m* is a toolbox required for running most of the other *Mathematica* programs listed in this section. It includes basic vector and crystallography analyses.

The functions include:

`DotProduct[{{a, b, c},{x, y, z}}]`: dot product of  $a \mathbf{i} + b \mathbf{j} + c \mathbf{k}$  and  $x \mathbf{i} + y \mathbf{j} + z \mathbf{k}$  vectors.

`CrossProduct[{{a, b, c},{x, y, z}}]`: cross product of  $a \mathbf{i} + b \mathbf{j} + c \mathbf{k}$  and  $x \mathbf{i} + y \mathbf{j} + z \mathbf{k}$  vectors.

`Norm[{a, b, c}]`: the norm of  $a \mathbf{i} + b \mathbf{j} + c \mathbf{k}$  vector.

`UnitVector[{a, b, c}]`: unit vector of  $a \mathbf{i} + b \mathbf{j} + c \mathbf{k}$ .

`Radian[{{a, b, c},{x, y, z}}]`: the angle (in radian) between  $a \mathbf{i} + b \mathbf{j} + c \mathbf{k}$  and  $x \mathbf{i} + y \mathbf{j} + z \mathbf{k}$  vectors.

Angle[{{a, b, c}, {x, y, z}}]: the angle (in degree) between  $a \mathbf{i} + b \mathbf{j} + c \mathbf{k}$  and  $x \mathbf{i} + y \mathbf{j} + z \mathbf{k}$  vectors.

Volume[{{a, b, c}, {x, y, z}, {p, q, r}}]: triple product of  $a \mathbf{i} + b \mathbf{j} + c \mathbf{k}$ ,  $x \mathbf{i} + y \mathbf{j} + z \mathbf{k}$ , and  $p \mathbf{i} + q \mathbf{j} + r \mathbf{k}$ .

Rotation[{u, v, w}, t] generates matrix for rotation around  $u \mathbf{i} + v \mathbf{j} + w \mathbf{k}$  by a  $t^\circ$ .  $u \mathbf{i} + v \mathbf{j} + w \mathbf{k}$  is not necessarily a unit vector.

Rel[{x, y, z}]: the reciprocal space direction  $x \mathbf{a}^* + y \mathbf{b}^* + z \mathbf{c}^*$  or the plane normal of (x y z) plane. This requires  $\mathbf{a}^*$ ,  $\mathbf{b}^*$ , and  $\mathbf{c}^*$  ( $\mathbf{a}^*$ ,  $\mathbf{b}^*$ , and  $\mathbf{c}^*$ ) being defined before using.

ABC[lpa, lpb, lpc, alpha, beta, gamma] assigns the basis vectors  $\mathbf{a}$ ,  $\mathbf{b}$ , and  $\mathbf{c}$  for entered crystal structures in Cartesian system.  $\mathbf{a}$ ,  $\mathbf{b}$ , and  $\mathbf{c}$  can be extracted correspondingly by taking the first, second, and third row given by ABC[ ] results. Lpa, lpb, and lpc are lattice parameters for  $\mathbf{a}$ ,  $\mathbf{b}$ , and  $\mathbf{c}$ . Alpha, beta, gamma are the three angles  $\alpha$ ,  $\beta$ , and  $\gamma$  in radian as defined by crystallography.

ABCstar[lpa, lpb, lpc, alpha, beta, gamma] gives the basis vectors in reciprocal space or  $\mathbf{a}^*$ ,  $\mathbf{b}^*$ , and  $\mathbf{c}^*$ .  $\mathbf{a}^*$ ,  $\mathbf{b}^*$ , and  $\mathbf{c}^*$  can be extracted correspondingly by taking the first, second, and third row given by ABCstar[ ] results. The parameters lpa, lpb, lpc, alpha, beta, and gamma are the same as those used in ABC function.

Axis[{x, y, z}]: the Cartesian coordinates for crystallographic direction  $x \mathbf{a} + y \mathbf{b} + z \mathbf{c}$ .  $\mathbf{a}$ ,  $\mathbf{b}$ , and  $\mathbf{c}$  are required (see ABC[ ]).

HexAxis[{x, y, z, l}] changes hexagonal 4-index coordinates [x y z l] into 3-index coordinates (in hexagonal coordinate system).

UnHexAxis[{x, y, l}] changes hexagonal 3-index coordinates [x y l] back to 4-index system.

Metric[lpa, lpb, lpc, alpha, beta, gamma] calculates the metrical matrix or metric tensor [124] for a crystal structure with lattice parameter lpa, lpb, and lpc and alpha, beta, and gamma ( $\alpha$ ,  $\beta$ , and  $\gamma$  angles).

Angrel[{{x1, y1, z1},{x2, y2, z2}}] returns the angle between two planes indexed (x1 y1 z1) and (x2 y2 z2). The astar, bstar, and cstar of the corresponding crystal structure are required (see ABCstar[ ]).

Angdir[{{x1, y1, z1},{x2, y2, z2}}] returns the angle between two directions indexed [x1 y1 z1] and [x2 y2 z2]. The a, b, and c of the corresponding crystal structure are required (see ABC[ ]).

permuzone[{a, b, c}]: generates permutations of  $\langle abc \rangle$  direction, for example:  $[abc]$ ,  $[ab\bar{c}]$ ,  $[ba\bar{c}]$ , etc. It does not include both positive and negative directions though, since the negative ones can simply be obtained by taking  $-\text{permuzone}[\{a, b, c\}]$ .

tiltangle[{thetax1, thetay1},{thetax2, thetay2}] finds the angle between two tilted directions: one at (thetax1, thetay1) and the other at (thetax2, thetay2) (Appendix A). All of these angles input or output are expressed in degree.

tiltdir[thetax, thetay] gives the direction of tilting at (thetax, thetay) angles in tilter's Cartesian coordinate system (Appendix A).

reallen[{thetax1, thetay1, l1},{thetax2, thetay2, l2}, {thetax3, thetay3, l3}] finds the real length of a line feature in three dimension using three different tilting positions (thetax1, thetay1), (thetax2, thetay2), and (thetax3, thetay3) degrees. At these tilting angles, the projected line feature is measured to have l1, l2, and l3 lengths, respectively.

`rotang[{{a, b, c},{d, e, f},{g, h, i}}]` gives the rotation angle of

$$\begin{bmatrix} a & b & c \\ d & e & f \\ g & h & i \end{bmatrix}$$

rotation matrix.

`rotaxis[{{a, b, c},{d, e, f},{g, h, i}}]` gives the rotation axis of

$$\begin{bmatrix} a & b & c \\ d & e & f \\ g & h & i \end{bmatrix}$$

rotation matrix.

`TraceAnalyzerf[{{x1, y1, z1}, {x2, y2, z2}, theta1, {x3, y3, z3}, theta2}, {{x1, y1, z1}, ...}, ...]` is to derive a trace from several zones of projection.  $\{x_1, y_1, z_1\}$ s are zone axes.  $\{x_2, y_2, z_2\}$ s and  $\{x_3, y_3, z_3\}$ s are two diffracting vectors on this zone. `theta1` and `theta2` are the angles (in degrees) between projected direction from the  $(x_2, y_2, z_2)$  and  $(x_3, y_3, z_3)$  reflections. At least three zone axes should be used. Error messages will be provided if bad parameters are entered, such as  $(x_2, y_2, z_2)$  and  $(x_3, y_3, z_3)$  reflections are not included in the  $[x_1, y_1, z_1]$  zone axis. This function is currently only good for cubic system.

2. *DiffPtnGnrI.ma* generates diffraction pattern for arbitrary crystal structures by entering the basic parameters of the crystal structures including:

- (1) Number of atoms, their notations, and scattering factors (atomic numbers may be satisfactory).

- (2) Crystal structures including lattice parameters (a, b, and c),  $\alpha$ ,  $\beta$ ,  $\gamma$ , and positions of atoms.
- (3) Wavelength of incident beam and camera length.
- (4) Zone axis (in crystal systems) of which diffraction pattern is to be calculated.

The pattern can be plotted, and the plotting used is contained in “pattpos” variable. All numbers in *pattpos* have unit in meter, therefore the exact size of pattern can be obtained and compared with the SADP negatives directly if the entered wavelength and camera length are calibrated.

3. *ZoneFinder.ma* is partly inherited from *DiffPtnGnrl.ma* program. It is assumed that the crystal structure is known. By entering two least spacing of patterns on the negatives of TEM SADPs and the angles between them, the zone axis of the diffraction patterns can be found and indexed. The application of this program requires accurate calibration of wavelength and camera length of the operating TEM.
4. *2PDiffPtnGnrl.ma* is also inherited from *DiffPtnGnrl.ma* program. It has ability to calculate diffraction patterns for two structures overlapping according to the entered orientation relationship.

The input requires not only the atomic structures of the matrix and precipitate crystals, but it also needs the information of the orientation relationship (in the crystal coordinate systems), i.e. the conjugate planes (conjuplane) and conjugate directions (conjudir).

The program aligns the two sets of the diffraction patterns in a proper direction following the OR. The pattern of the matrix is shown in darker color and with a larger size (controlled by *dotsize*). The precipitate pattern is lighter and smaller. The

relative sizes of the spots indicate the intensity of the spots.

Tolerance angle is allowed to permit a looser condition for parallel zones. In most of the orientation relationship, there are only a limited sets of zone axes where the precipitate and matrix patterns can be perfectly parallel. However, in TEM operation, two diffraction patterns are frequently found present together, even if the zone axes are not exactly parallel, e.g.  $[\bar{1}\bar{2}1]_f$  vs.  $[3\bar{1}2]_b$  under K-S OR. The angle between them is around  $0.5^\circ$  numerically.

The variable “tang” is to define how loose to have this parallel condition set. If zero is set, two zone axes must be exactly parallel in order to show simultaneously on the calculated patterns. If larger than 0 is set, as long as two zone axes are within this degree off from each other, the nearby precipitate zone can still be evaluated and shown. This angle should not be larger than  $1^\circ$ . This information is also printed out in the result.

5. *GnrlStereoProj.ma* plots the standard stereo-projection for general crystal structures by entering a, b, c,  $\alpha$ ,  $\beta$ , and  $\gamma$ .
6. *ORZoneCorr.ma*: Given the orientation relationship, there are limited zones axes to have the diffraction patterns of the precipitates and matrix overlapped or close to each other. This program is to look into the low indexed zone axes and find the nearby low indexed zones in the other phase.
7. *ORZoneCorrPerm.ma* is revised for finding a close direction in precipitate given an interested matrix direction, or enter the family of a zone axis, the program finds the nearby directions within the given families.

8. *FoilNormal.ma* is to rotate the double tilter's coordinate system into the crystallographic system. Once the coordinate translation matrix is built, it can be used to evaluate foil normal by translating [001] direction (foil normal direction in double tilter's coordinate) into the crystallographic direction of the foil normal (Appendix A).
9. *TiltIDXer.ma* combines tiltangle[ ] in *VectorAnalysis.ma* and *GnrlStereoProj.ma* to give a plot of tilted zones on angular stereo-projection. The projection can be compared with the crystallographic stereo-projection as long as the foil normal is known (see *FoilNormal.ma*). The center pole of this stereo-projection plot is the foil normal, i.e. the direction where foil is not tilted. It is also possible to compare more than one indexing job on one single foil. By this, the indexing work can be combined to index the zones consistently even in a different job.
10. *KSNiCrAtomhkl.ma* generates atomic structure in the vicinity of the (h k l) interface using specified orientation relationship. It can be modified for different crystal structures, orientation relationships, or (h k l) planes. The calculated structures are comparable with the HREM observations.
11. *BMDBMP.ma*: procedure for evaluating the best-matching direction/best matching plane.
12. *CORRfinder.c*: procedure for evaluating lattice correspondences knowing orientation relationship following procedures described by Jaswon and Wheeler [31]. The O-Lattice size is used as a criterion to find all the possible correspondence. This program is employed in Chapter 5. The current version is for fcc:bcc under K-S OR only. It is revisable for other crystal structures.

13. *biginter.f* is modified from DEVIL codes [84] for binary EAM simulations used in Chapter 3.
14. *runbg2.c* iteratively generates simulation blocks of different configurations (Chapter 3) for *biginter.f* executions. The programming is limited for fcc:bcc transformation with K-S OR.
15. Other programs:
  - Grow.c* grows precipitates based on the criterion of nearest neighbor. The programming is limited for fcc:bcc transformation with K-S OR.
  - PlanarFaultLedge.c* estimates the average misfit for a plane specified. The programming is limited for fcc:bcc transformation with K-S OR.
  - MatrixOperation.h*: Matrix operation library for C.
  - VectorOperation.h*: Vector operation library for C.
  - NCSL.c* calculates near coincident sites for fcc:bcc in K-S OR.
  - WSExt.c* evaluates the dislocation network using O-lattice theory [16]. The programming is limited for fcc:bcc transformation with K-S OR, and the lattice correspondence used is Bain correspondence.
  - SUZUKImart.ma* is a Suzuki version of PTMC [122].
  - phbndry.c* is a modified version of TEM dislocation contrast simulation [64, 63] (in C language).

## C.2 Codes

Programs included are *VectorAnalysis.m*, *CORRfinder.c*, *BMDBMP.ma*, and *ZoneFinder.ma*.

```
(* VectorAnalysis.m *)
(* File created by Jhewn-Kuang Chen, T_Group, MSE, Virginia Tech, c1991 *)
(* usages of functions added by JKC, February 17, 1995 *)
(* Please read ./aReadMe.First while using/modifying these codes. *)
```

```
Unprotect[DotProduct,CrossProduct,Norm,UnitVector,Radian,Angle,Volume,Rotation,Axi
s,HexAxis,UnHexAxis,Rel,Angdir,Angrel,ABC,ABCstar,Metric,Permuzone,tiltangle,realle
n,TraceAnalyzerf,tiltdir,rotang,rotaxis];
```

```
DotProduct::usage="DotProduct[{{a,b,c},{x,y,z}}] gives the dot product of {a,b,c} and
{x,y,z}."
```

```
CrossProduct::usage="CrossProduct[{{a,b,c},{x,y,z}}] gives the cross product of {a,b,c}
and {x,y,z}."
```

```
Norm::usage="Norm[{a,b,c}] gives the norm of {a,b,c}."
```

```
UnitVector::usage="UnitVector[{a,b,c}] gives the unit vector of {a,b,c}."
```

```
Radian::usage="Radian[{{a,b,c},{x,y,z}}] gives the angle between directions {a,b,c} and
{x,y,z} in radian."
```

```
Angle::usage="Angle[{{a,b,c},{x,y,z}}] gives the angle between directions {a,b,c} and
{x,y,z} in degree."
```

```
Rotation::usage="Rotation[{a,b,c},theta] gives a matrix rotating around {a,b,c} by theta
Degree"
```

```
Axis::usage="Axis[{x,y,z}] gives the cartesian vector for crystal vector [x,y,z]. (a, b, c,
astar, bstar, and cstar is required in this functon, see ABC and ABCstar usage)"
```

```
HexAxis::usage="HexAxis[{x,y,z,l}] convert [x,y,z,l] direction in HCP into [a,b,l] indices."
```

```
UnHexAxis::usage="UnHexAxis[{a,b,l}] converts [a,b,l] into 4 indices of [x,y,z,l] in HCP
system."
```

```
Rel::usage="Rel[{x,y,z}] gives the rel space vecotr of (x,y,z)."
```

```
Angdir::usage="Angdir[{{x1,y1,z1},{x2,y2,z2}}] returns the angle between two directions
indexed [x1,y1,z1] and [x2,y2,z2]. (a, b, c, astar, bstar, and cstar is required in this
functon, see ABC and ABCstar usage)"
```

**Angrel::usage="Angrel[{{x1,y1,z1},{x2,y2,z2}}]** returns the angle between two planes indexed (x1,y1,z1) and (x2,y2,z2). (a, b, c, astar, bstar, and cstar is required in this function, see ABC and ABCstar usage)"

**ABC::usage="ABC[a,b,c,alpha,beta,gamma]** gives the basis vectors a, b, and c in Cartesian coordinates."

**ABCstar::usage="ABCstar[lpa,lpb,lpc,alpha,beta,gamma]** gives the basis vectors astar, bstar, and cstar in the reciprocal space."

**permuzone::usage="permuzone[{x,y,z}]** gives the permutative zones of {x,y,z}"

**tiltdir::usage="tiltdir[thetax,thetay]** is to give the direction of tilting at (thetax,thetay) angles in tilter's coordinate system."

**tiltangle::usage="tiltangle[{thetax1,thetay1},{thetax2,thetay2}]** gives the angle between two tilting directions."

**reallen::usage="reallen[{thetax1,thetay1,l1},{thetax2,thetay2,l2},{thetax3,thetay3,l3}]** gives the real length of a trace given the tilting angles and their projected lengths."

**TraceAnalyzerf::usage="TraceAnalyzerf[{{x1,y1,z1},{x2,y2,z2},theta1,{x3,y3,z3},theta2}, ...]** is to derive a trace from several zones of projections."

**Metric::usage="Metric[lpa,lpb,lpc,alpha,beta,gamma]** is to give the metrical matrix or metric tensor for a crystal structure with lattice parameter lpa, lpb, and lpc and alpha, beta, and gamma angles."

**rotang::usage="rotang[{{a,b,c},{d,e,f},{g,h,i}}]** gives the rotation angle of {{a,b,c},{d,e,f},{g,h,i}} rotation matrix."

**rotaxis::usage="rotaxis[{{a,b,c},{d,e,f},{g,h,i}}]** gives the rotation axis of {{a,b,c},{d,e,f},{g,h,i}} rotation matrix."

**DotProduct[{{a\_,b\_,c\_},{x\_,y\_,z\_}}]:=a x + b y + c z**

**CrossProduct[{{a\_,b\_,c\_},{x\_,y\_,z\_}}]:={b z - c y, c x - a z, a y - b x}**

```
Norm[{a_,b_,c_}]:=Chop[Sqrt[a^2+b^2+c^2]]//N
```

```
UnitVector[{a_,b_,c_}]:={a,b,c}/Norm[{a,b,c}]
```

```
Radian[{a_,b_,c_},{x_,y_,z_}]:=ArcCos[DotProduct[{a,b,c},{x,y,z}]/Norm[{a,b,c}]/Norm[{x,y,z}]] //N
```

```
Angle[{a_,b_,c_},{x_,y_,z_}]:=Chop[ArcCos[DotProduct[{a,b,c},{x,y,z}]/Norm[{a,b,c}]/Norm[{x,y,z}]]/Degree] //N
```

```
Volume[{a_,b_,c_},{x_,y_,z_},{p_,q_,r_}]:=Chop[Det[{a,b,c},{x,y,z},{p,q,r}]]//N
```

```
(* Matrix for rotation around {u,v,w} by t degree. *)
```

```
Rotation[{u_,v_,w_},t_]:=Block[{c,s,i},  
  c=1-Cos[t Degree]//N; s=Sin[t Degree]//N;  
  i=UnitVector[{u,v,w}];  
  Return[{{i[[1]]^2 c + 1 - c, i[[1]] i[[2]] c - i[[3]] s,i[[1]] i[[3]] c + i[[2]] s},  
    {i[[1]] i[[2]] c + i[[3]] s, i[[2]]^2 c + 1 - c, i[[2]] i[[3]] c - i[[1]] s},  
    {i[[1]] i[[3]] c - i[[2]] s, i[[3]] i[[2]] c + i[[1]] s, i[[3]]^2 c + 1 - c}}];
```

```
]
```

```
(* Position of (x,y,z) in the Cartesian *)
```

```
Axis[{x_,y_,z_}]:=x a+y b+z c
```

```
HexAxis[{x_,y_,z_,l_}]:={2x+y,2y+x,l}
```

```
UnHexAxis[{x_,y_,l_}]:={(2y-x)/3,(2x-y)/3,(-x-y)/3,l}
```

```
(* Normal of (x,y,z) plane in Cartesian *)
```

```
Rel[{x_,y_,z_}]:=x astar+y bstar+z cstar
```

```
(* angle between two zones *)
```

```
Angdir[{{x1_,y1_,z1_},{x2_,y2_,z2_}}]:=Angle[Axis[{x1,y1,z1}],Axis[{x2,y2,z2}]]
```

```
(* angle between two planes *)
```

```
Angrel[{{x1_,y1_,z1_},{x2_,y2_,z2_}}]:=Angle[Rel[{x1,y1,z1}],Rel[{x2,y2,z2}]]
```

```
(* input a,b,c,alpha,beta,gamma to obtain the axes for a,b,and c ,
```

```
  a, b, and c are in Angstrom.
```

```
  alpha, beta, and gamma in radian. *)
```

```
ABC[pa_,lpb_,lpc_,alpha_,beta_,gamma_]:=
```

```
  Block[{aa,bb,cc},
```

```

aa={lpa,0,0};
bb={lpb Cos[gamma],lpb Sin[gamma],0}//N;
cc={Cos[beta], Cos[alpha] Csc[gamma], 1-Cos[beta]^2-
      (Cos[alpha]*Csc[gamma]- Cos[beta]*Cot[gamma])^2}*lpc//N;
Return[{{aa,bb,cc}}];
]
(* unit cell - 3 main axis expressed in Cartesian
   ABCstar give 3 rel space basis vector
*)
ABCstar[lpa_,lpb_,lpc_,alpha_,beta_,gamma_]:=
  Inverse[Transpose[ABC[lpa,lpb,lpc,alpha,beta,gamma]]];
(* obsolete version of ABC[] *)
(*
ABC[lpa_,lpb_,lpc_,alpha_,beta_,gamma_]:=
  Block[{{aa,bb,cc,eqn1,eqn2,eqn3,csolu,c1,c2,c3},
    aa={lpa,0,0};
    bb={lpb Cos[gamma],lpb Sin[gamma],0}//N;
    cc={c1,c2,c3};
    det=Det[{{aa,bb,cc}}];
    eqn1=UnitVector[aa].cc;
    eqn2=UnitVector[bb].cc;
    csolu=Solve[{{eqn1==Cos[beta],eqn2==Cos[alpha]},{c1,c2}}][[1]]//N;
    c1=c1/.csolu;
    c2=c2/.csolu;
    c3=Sqrt[1-c1^2-c2^2]/.csolu;
    Return[{{aa,bb,{c1,c2,c3}*lpc}}];
]
*)

(* Metric matrix of a crystal structure 3/7/95 *)
Metric[lpa_,lpb_,lpc_,alpha_,beta_,gamma_]:=
  {{lpa lpa,lpa lpb Cos[gamma], lpa lpc Cos[beta]},
   {lpb lpa Cos[gamma], lpb lpb, lpb lpc Cos[alpha]},
   {lpc lpa Cos[beta],lpc lpc Cos[alpha], lpc lpc}}//N

(* permuzone[{{a,b,c}}] is to generate permutations of <a,b,c> directions. *)
permuzone[{{x_,y_,z_}}]:=
Block[{{i,l,ll,addzone,newzone,checkzone},
  addzone={};
  checkzone={{x,y,z},{x,y,-z},{x,-y,z},{-x,y,z},
    {y,z,x},{y,z,-x},{y,-z,x},{-y,z,x},

```

```

        {z,x,y},{z,x,-y},{z,-x,y},{-z,x,y},
        {z,y,x},{z,y,-x},{z,-y,x},{-z,y,x},
        {y,x,z},{y,x,-z},{y,-x,z},{-y,x,z},
        {x,z,y},{x,z,-y},{x,-z,y},{-x,z,y}
    };
    For[i=1,i<=24,i++,
        ll=Length[addzone];
        newzone=checkzone[[i]];
    For[l=1,l<=ll,l++,
        If[addzone[[l]]==newzone ||
            addzone[[l]]==newzone,l=ll+2];
    ];
    If[l==ll+1 || l==0,
        addzone=Join[addzone,{newzone}];
    ];
];
Return[addzone];
]

```

```

tiltdir[thetax_,thetay_]:={-Cos[thetax Degree] Sin[thetay Degree],Sin[thetax
Degree],Cos[thetax Degree] Cos[thetay Degree]}/N

```

(\* tiltangle[thetax1,thetay1,thetax2,thetay2] is to find the angle between two tilted directions: one at (thetax1,thetay1) and the other at (thetax2,thetay2).

```

*)
tiltangle[{thetax1_,thetay1_},{thetax2_,thetay2_}]:=Block[{s,t,n,o},
    s=thetax1 Degree;
    t=thetay1 Degree;
    n=thetax2 Degree;
    o=thetay2 Degree;
    Return[ArcCos[Cos[n] Cos[o] Cos[s] Cos[t] +
        Cos[o] Cos[t] Sin[n] Sin[s] + Sin[o] Sin[t]]/Degree]/N;
];

```

```

(* 7/10/95 rotang::usage=
"rotang[{{a,b,c},{d,e,f},{g,h,i}}] gives the rotation
angle of {{a,b,c},{d,e,f},{g,h,i}} rotation matrix." *)
rotang[{{a_,b_,c_},{d_,e_,f_},{g_,h_,i_}}]:=
    ArcCos[(a+e+i-1)/2]/Degree//N

```

```

(* 7/10/95 rotaxis::usage=
"rotaxis[{{a,b,c},{d,e,f},{g,h,i}}] gives the rotation

```

```

axis of {{a,b,c},{d,e,f},{g,h,i}} rotation matrix." *)
rotaxis[{{a_,b_,c_},{d_,e_,f_},{g_,h_,i_}}]:=
  NullSpace[{{a,b,c},{d,e,f},{g,h,i}}-IdentiMatrix[3]][[1]] //N

(* reallen[{thetax1,thetay1,l1},{thetax2,thetay2,l2},{thetax3,thetay3,l3}] is to find the real
lengths of a feature in 3-D using 3 different viewing conditions. These viewing directions
must be non-coplanar.
*)
reallen[{thetax1_,thetay1_,l1_},{thetax2_,thetay2_,l2_},
  {thetax3_,thetay3_,l3_}]:=
  Block[{tx1,ty1,tx2,ty2,tx3,ty3,x1,x2,x3,y1,y2,y3,z1,z2,z3,dv3,J,iJ,
    p1,p2,p3,maxiter,v,errsqr,time,dijv,iJv,pv,dv,x,y,z},
    tx1=thetax1 Degree; ty1=thetay1 Degree;
    tx2=thetax2 Degree; ty2=thetay2 Degree;
    tx3=thetax3 Degree; ty3=thetay3 Degree;

    x1=Sin[ty1];      x2=Sin[ty2];      x3=Sin[ty3];
    y1=-Sin[tx1] Cos[ty1];      y2=-Sin[tx2] Cos[ty2]; y3=-Sin[tx3] Cos[ty3];
    z1=Cos[tx1] Cos[ty1]; z2=Cos[tx2] Cos[ty2]; z3=Cos[tx3] Cos[ty3];

    dv3=Det[{{x1,x2,x3},{y1,y2,y3},{z1,z2,z3}}]//N;
    p1=(1-x1^2) x^2+(1-y1^2) y^2 + (1-z1^2) z^2-2 x1 y1 x y -
      2 y1 z1 y z -2 x1 z1 x z - l1^2//N;
    p2=(1-x2^2) x^2+(1-y2^2) y^2 + (1-z2^2) z^2-2 x2 y2 x y -
      2 y2 z2 y z -2 x2 z2 x z - l2^2//N;
    p3=(1-x3^2) x^2+(1-y3^2) y^2 + (1-z3^2) z^2-2 x3 y3 x y -
      2 y3 z3 y z -2 x3 z3 x z - l3^2//N;

    iJ=Simplify[Together[Inverse[{{D[p1,x],D[p1,y],D[p1,z]},
      {D[p2,x],D[p2,y],D[p2,z]}, {D[p3,x],D[p3,y],D[p3,z]}]}]//N;

    maxiter=200;
    v=Max[{l1,l2,l3}]/3//N; v={{v},{v},{v}};
    errsqr=1;      time=dijv=0;
    While[errsqr>1.0 10^-10 && time<=maxiter,
      iJv=iJ/.{x->v[[1,1]],y->v[[2,1]],z->v[[3,1]]}//N;
      pv={{p1},{p2},{p3}}/.{x->v[[1,1]],y->v[[2,1]],
        z->v[[3,1]]}//N;
      dv=iJv.pv;
      errsqr=dv[[1,1]]^2+dv[[2,1]]^2+dv[[3,1]]^2;
      v=v-dv;

```

```

        time++;
    ];
    Print["Iteration time = ",time];
    Print["Square of error = ",errsqr];
    If[time>=maxiter,
        Print["The iteration time is larger than ",maxiter,". "];
        Print[" the program is terminated abnormally."];
        Print["Solouction can not be obtained."];
    ];
    Print[" "];
    If[errsqr<=1.0 10^-10,
        Print["Length at (" ,thetax1," ,",thetay1,") is ",l1,"."];
        Print["Length at (" ,thetax2," ,",thetay2,") is ",l2,"."];
        Print["Length at (" ,thetax3," ,",thetay3,") is ",l3,"."];
        Print[Transpose[v][[1]]];
        Print["Real Length = ",
            Sqrt[v[[1,1]]^2+v[[2,1]]^2+v[[3,1]]^2//N];
    ]
]
]

```

(\* TraceAnalyzerf[{{x1,y1,z1},{x2,y2,z2},theta1,{x3,y3,z3},theta2}, ...]

to derive a trace from several zones of projection.

{x1,y1,z1}s are zone axes. {x2,y2,z2} and {x3,y3,z3} are reflections on this zone.

theta1 and theta2 are the angle between projected direction from the corresponding reflections.

\*)

```
TraceAnalyzerf[data_]:=Block[{len,zones,ang,i,j,accBcirc,ang1,ang2,ang3,m,proj,Bcirc,le
nBc,realdir,ii,jj,lenreal,mang,accang,time,nowang,finaldir,bigang,sumang},
```

```
len=Length[data]; (* no. of zone *)
```

```
zones={};
```

```
ang={};
```

```
For[i=1,i<=len,i++,
```

```
    If[Length[data[[i]]]!=5,
```

```
        Print["[Error]", "Format incorrect in zone ",i,"."];
```

```
        Return[]; ];
```

```
    AppendTo[zones,{data[[i,1]]/Norm[data[[i,1]]],
```

```
        data[[i,2]]/Norm[data[[i,2]]],
```

```
        data[[i,4]]/Norm[data[[i,4]]]};
```

```
    AppendTo[ang,{data[[i,3]] Degree ,
```

```

        data[[i,5]] Degree//N];
];
zones;
ang; (* sorting zones and angles from the input data *)

accBcirc={};
For[i=1,i<=len,i++,
ang1=Radian[{zones[[i,2]],zones[[i,3]]}];
ang2=Abs[ang[[i,1]]+ang[[i,2]]-ang1]/N;
ang3=Abs[Abs[ang[[i,1]]-ang[[i,2]]]-ang1]/N;
If[!(ang2<=0.025 || ang3<=0.025),
    Print["Error", "The angles entered in zone ",i,
    " are not consistent with the reflection."];
    Return[];
];
For[j=1,j<=3,j++,
    If[Length[zones[[i,j]]]!=3,
        Print["Error", "Format incorrect in zone ",i,"/",j,
        "position"];
        Return[];];
];
For[j=1,j<=2,j++,
    If[Length[ang[[i,j]]]!=1,
        Print["Error", "Format incorrect in angle of zone ",i,"/",j,
        "position"];
        Return[]; ];
];
If[Abs[zones[[i,1]].zones[[i,2]]]>1. 10^-6 ||
    Abs[zones[[i,1]].zones[[i,3]]]>1. 10^-6,
    Print["Error",
        "At least one of the reflection is not on zone ",
        i, "."];
    Return[];
];
m=Inverse[{zones[[i,1]],zones[[i,2]], zones[[i,3]]}];
proj=Transpose[m.{0},{Cos[ang[[i,1]]],
    {Cos[ang[[i,2]]]}][[1]]/N;
Bcirc=CrossProduct[{zones[[i,1]],proj};
AppendTo[accBcirc,Bcirc];
];

```

```

accBcirc; (* Big circles obtained from each zone *)

realdir={};
lenBc=Length[accBcirc];
For[j=1,i<=lenBc-1,i++,
  For[j=i+1,j<=lenBc,j++,
    m=UnitVector[CrossProduct[
      {accBcirc[[i]], accBcirc[[j]]} ] ];
    If[Length[Position[m,-Max[Abs[m]]]]!=0,m/=-1 ];
    AppendTo[realdir, m ];
  ];
];
realdir; (* Real direction obtained by intersection of big circles. *)

lenreal=Length[realdir];
mang=Table[Angle[{realdir[[ii]],realdir[[jj]}],
  {jj,1,lenreal-1}, {ii,jj+1,lenreal}];
accang=Table[0,{ii,lenreal}];
For[j=1,i<=lenreal,i++,
  For[j=1,j<=lenreal,j++,
    If[j<i,
      If[mang[[j,i-j]]>=165 || mang[[j,i-j]]<=15 ,
        accang[[i]]++; accang[[j]]++ ],
      If[i<j,
        If[mang[[i,j-i]]>=165 || mang[[i,j-i]]<=15 ,
          accang[[i]]++; accang[[j]]++ ];
      ];
    ];
];
m=Max[accang] ; (* the best fit direction *)
If[(* m>=15*lenreal *) m<1,
  Print["[Error]",
    "Obtained directions are not in a reasonable small",
    "range. ",m,
    " pairs of vectors are available."];
  Print["The current traces (may contain significant error) are : ",realdir];
  Return[];
];
If[(* m>=15*lenreal *) m<3,
  Print["[Warning]",

```

```

        "There may contain errors in the calculated results.");
];
m=Position[accang,m][[1,1]];

finaldir={0,0,0};
time=bigang=sumang=0;
For[i=1,i<=lenreal,i++,
  nowang=0;
  If[m<i,nowang=mang[[m,i-m]],
    If[m>i,nowang=mang[[i,m-i]]];
  ];
  If[nowang<=10,finaldir+=realdir[[i]];
    If[nowang>bigang,bigang=nowang];
    sumang+=nowang;
    time++];
  If[nowang>=170,finaldir-=realdir[[i]]; nowang=180-nowang;
    If[nowang>bigang,bigang=nowang];
    sumang+=nowang;
    time++];
  (* adding all nearby direction *)
];
If[time<=1, Print[realdir];
  Print["[Error]",
    " Triangles are all too big and cannot be used."];
  Return[Null];
];
finaldir=UnitVector[finaldir];
  (* average out finaldir *)
For[i=1,i<=lenreal,i++,
  For[j=1,j<=lenreal-i,j++,
    If[mang[[i,j]]>=90, mang[[i,j]]=180-mang[[i,j]]];
  ];
];
Print["The worst direction to direction angle is ", Max[mang],
  "."];
Print["The largest direction to direction angle used is ",
  N[bigang,3],"."];
Print["The average direction to direction angle is ",
  N[sumang/(time-1),3],"."];
Print[time," out of ", lenreal," lines are being used",
  " to obtain the following result."];
Print[" "];

```

```
Return[finaldir];
```

```
];
```

```
Protect[DotProduct,CrossProduct,Norm,UnitVector,Radian,Angle,Volume,Rotation,Axis,  
HexAxis,UnHexAxis,Rel,Angdir,Angrel,ABC,ABCstar,Metric,Permuzone,tiltangle,realen,  
TraceAnalyzerf,tiltdir,rotang,rotaxis];
```

```

/*
CORRfinder.c
    inherited from ORS12optimizer.c
    inherited from RotEvaluation.c
    inherited from PlanarFaultLedg.c

J.K.Chen, T_Group, MSE, VA Tech, USA
May 25, c1995

Evaluation of correspondences: knowing the orientation relationship,
using O-Lattice size as criterion and find all the possible
correspondence.

*/

#include <stdio.h>
#include <stdlib.h>
#include <math.h>
#include </usr/users/jkchen/Program/MatrixOperation/MatrixOperation.h>
        /* matrix operation utility */

float  *nearbcc(float *fcc);
        /* nearby bcc atom of fcc[3] in fcc coordinates */
void   creatCorres();

float  lratio=1.255,          /* lattice parameter ratio a(fcc)/a(bcc) */
R[3][3]={{0.6498299143, -0.7415816238, -0.1666666667},
        {0.7415816238, 0.6666666667, -0.07491495713},
        {0.1666666667, -0.07491495713, 0.9831632476}};
        /* R.Xf=Xb in bcc coordinate system under K-S OR */

int    MAXsize=10;
struct corres
{
    float  S1[3][3],B[3][3],l[3],Osize;
    long   count;
    struct corres *next;
};

struct corres *firstCorres, *thisCorres, *newCorres;
        /* structure that records the information of lattice correspondences */

```

```

main()
{
    float **S1,**S2,**S1i,**S0,
          **A,**B,**tR,
          **temp,**temp2,
          detpvector,**p,
          l[3]={0.},templ,
          *bcc,Osize=0.0,total=0.0 ,ds1,ds2 ;
    int   prime[15]={2,3,5,7,11,13,17,19,23,29,31,37,41,43,47},
          /* all prime numbers < 50 */
          primeQ[51][15]={0},
          /* primeQ[x][y]: x is a multiplier of prime[y]?
                                0=yes, 1=no */
          pvector[3][3]={0},
          i,j,k, now,continu=1,count=0,
          FLAG=0;
    FILE*fi,*fo;

    /* initializing matrices */
    S1=DMatrix(3,3); /* fcc unit cell */
    S2=DMatrix(3,3); /* bcc unit cell */
    S1i=DMatrix(3,3); /* inverse of S1 */
    A=DMatrix(3,3); /* transformation matrix */
    B=DMatrix(3,3); /* lattice correspondence */
    S0=DMatrix(3,3); /* the most basic fcc primitive cell */
    tR=DMatrix(3,3); /* transpose of R */
    temp=DMatrix(3,3); /* following are temporary 3 by 3 matrices */
    temp2=DMatrix(3,3);
    p=DMatrix(3,3);

    for (i=0;i<3;i++)
        for (j=0;j<3;j++)
            S0[i][j]=0.5;
    S0[0][2]=S0[1][0]=S0[2][1]=0.0;

    creatCorres(); /* new chain */
    firstCorres=thisCorres=newCorres; /* set chain pointer */

    printf("Please enter the lattice parameter ratio of fcc to bcc : ");
    scanf("%f",&lratio);

```

```

if (lratio==0)lratio=1.255;
printf("The lattice parameter ratio is %f\n",lratio);

printf("Please enter the maximum basis vector length : ");
scanf("%d",&MAXsize);
if ((MAXsize==0) || (MAXsize>50))      MAXsize=10;
printf("The maximum basis vector length = %d\n",MAXsize);

/* set up multipliers */
for (i=1;i<=50;i++)
{
    for(j=0;j<15;j++)
    {
        if (((i%prime[j])==0) && (i>=prime[j]))
            primeQ[i][j]=0;
            /* i is a multiplier of prime[j] */
        else primeQ[i][j]=1;      /* is not */
    }
}

for(i=0;i<3;i++)
    for(j=0;j<3;j++)
        tR[i][j]=R[j][i];

/* iterations for all possible choices of S1 */
for (pvector[0][0]=-MAXsize;pvector[0][0]<=0;pvector[0][0]++)
{
    for (pvector[0][1]=-MAXsize;pvector[0][1]<=MAXsize;pvector[0][1]++)
    {
        for (pvector[0][2]=-MAXsize;pvector[0][2]<=MAXsize;pvector[0][2]++)
        {
            for (pvector[1][0]=-MAXsize;pvector[1][0]<=MAXsize;pvector[1][0]++)
            {
                for (pvector[1][1]=-MAXsize;pvector[1][1]<=MAXsize;pvector[1][1]++)
                {
                    for (pvector[1][2]=-MAXsize;pvector[1][2]<=MAXsize;pvector[1][2]++)
                    {
                        if (!(((pvector[0][1]*pvector[1][2]-pvector[1][1]*pvector[0][2]==0) &&
                            (pvector[0][0]*pvector[1][2]-pvector[1][0]*pvector[0][2]==0) &&
                            (pvector[0][1]*pvector[1][0]-pvector[1][1]*pvector[0][0]==0))))

```



```

/* continu==1 meaning that all 9 numbers in the matrix are
   devidable by a prime number, i.e. there exists a GCF larger
   than 1 and should not coninue, since this is a repeat of
   other smaller cells. */
}
}

/* getting fcc unit cell S1 */
MatrixMult(3,3,S0,3,3,p,S1);
ds1=Det(3,S1);

/* looking for the nearest bcc unit cell S2 */
if ((continu==0) && (fabs(ds1)<=1.25))
{
  Transpose(3,3,S1,p);

  for(i=0;i<3;i++)
  {
    bcc=nearbcc(p[i]);
    for(j=0;j<3;j++)
      S2[j][i]=bcc[j];      /* row to column */
    free(bcc);
  }
  ds2=Det(3,S2);

  /* finding A = transformation matrix = R.S2.S1^-1 */
  InMatrix(3,S1,S1i);
  MatrixMult(3,3,tR,3,3,S2,A);      /* A=R.S2 */
  MatrixMult(3,3,S2,3,3,S1i,B);      /* B=S2.S1^-1 */
  MatrixMult(3,3,A,3,3,S1i,temp);      /* temp=R.S2.S1^-1 */
  ScalMult(1/lratio,3,3,temp,A);

  InMatrix(3,A,temp); /* temp=A^-1 */
  for (i=0;i<3;i++)
    for(j=0;j<3;j++)
      temp2[i][j]=-temp[i][j];

  for(i=0;i<3;i++)
    temp2[i][i]++;

  InMatrix(3,temp2,temp); /* (I-A^-1)^-1 */
  Osize=Det(3,temp);      /* determinant = O-cell size */
}
}

```

```

if ((Osize>=20000) && (ds2/ds1==2.))
{
    for(i=0;i<3;i++)
        l[i]=(S1[0][i]*S1[0][i]+S1[1][i]*S1[1][i]+
            S1[2][i]*S1[2][i]);

    for(i=0;i<2;i++)
        for(j=i+1;j<3;j++)
            if (l[j]<l[i])
                {    templ=l[i];    l[i]=l[j]; l[j]=templ;}

    total++;
    thisCorres=firstCorres;
    FLAG=0;
    while ((thisCorres->next!=NULL) && (FLAG==0))
    {
        FLAG=1;
        for (i=0;i<3;i++)
        {
            for (j=0;j<3;j++)
            {
                if (fabs(thisCorres->B[i][j]-B[i][j])>0.001)
                {    i=3;    j=3;    FLAG=0;    }
                    /* different correspondence */
            }
        }
    }

    if (FLAG==1)    /* the same correspondence */
    {
        continu=1;
        for(i=0;i<3;i++)
        {
            if ((l[i]-thisCorres->l[i])<0.0001) continu*=1;
            else {    continu*=0;    i=3;}
        }

        if (continu==1)
        {
            /* keep the smallest basis vectors for S1 */
            for (i=0;i<3;i++)

```

```

        {
            thisCorres->l[i]=l[i];
            for (j=0;j<3;j++)
                thisCorres->S1[i][j]=S1[i][j];
        }
    }

    /* lattice correspondence counter */
    thisCorres->count++;
}
else /* FLAG==0 */
{
    thisCorres=thisCorres->next; }
}

if (FLAG==0) /* have not found this correspondence before */
{
    /* cread a new chain member */
    creatCorres();
    thisCorres->next=newCorres;
    thisCorres->count=1; /* counter */
    thisCorres->Osize=Osize;
    for(i=0;i<3;i++)
        thisCorres->l[i]=l[i]; /* basis vector lengths */

    for (i=0;i<3;i++)
    {
        for (j=0;j<3;j++)
        {
            thisCorres->B[i][j]=B[i][j];
            thisCorres->S1[i][j]=S1[i][j];
        }
    }

    printf("\n%d. The primitive cell of the matrix is :",
        ++count);
    printMatrix(3,3,S1);
    printf("\nThe size of primitive cell is %4.1f fcc atoms",
        4.0*ds1);

    printf("\nThe primitive cell of the precipitate is :");
    printMatrix(3,3,S2);

```

```

        printf("\nThe correspondence is :");
        printMatrix(3,3,B);

        printf("\nThe O-lattice matrix is :");
        printMatrix(3,3,temp);

        printf("\nThe O-lattice size is %e fcc primitive cell \n\n",
                Osize);
    }
}
/* if continu=0 */
}}}
} /* if ! (... */
}}} }}}

fo=fopen("correspondence.dat","w");
thisCorres=firstCorres;
printf("\n\n===== ");
printf("\nSummarized results start here: ");
printf("\n\nTotal number of considered correspondences=%-5.0f",total);
FLAG=1;
while (thisCorres->next!=NULL) /* while the chain has not ended */
{
    for(i=0;i<3;i++)
        for (j=0;j<3;j++)
            fprintf(fo,"%5.2f ",thisCorres->S1[i][j]);

    fprintf(fo,"\n",thisCorres->S1[i][j]);
    for(i=0;i<3;i++)
        for (j=0;j<3;j++)
            fprintf(fo,"%f ",thisCorres->B[i][j]);
    fprintf(fo,"\n%d\n",thisCorres->count);

    printf("\n#%d --- \n\nThe primitive cell of the matrix is :\n",FLAG);
    for(i=0;i<3;i++)
    {
        for(j=0;j<3;j++)
            printf("%f ",thisCorres->S1[i][j]);
    }
}

```

```

    printf("\n");
}
ds1=thisCorres->S1[0][0]*thisCorres->S1[1][1]*thisCorres->S1[2][2]+
    thisCorres->S1[0][1]*thisCorres->S1[1][2]*thisCorres->S1[2][0]+
    thisCorres->S1[0][2]*thisCorres->S1[1][0]*thisCorres->S1[2][1]-
    thisCorres->S1[0][2]*thisCorres->S1[1][1]*thisCorres->S1[2][0]-
    thisCorres->S1[0][1]*thisCorres->S1[1][0]*thisCorres->S1[2][2]-
    thisCorres->S1[0][0]*thisCorres->S1[1][2]*thisCorres->S1[2][1];
printf("\nThe size of primitive cell is %.1f fcc atoms",
        4*ds1);

printf("\nThe correspondence is :\n");
for(i=0;i<3;i++)
{
    for(j=0;j<3;j++)
        printf("%f ",thisCorres->B[i][j]);
    printf("\n");
}

printf("\nThe count for this correspondence is %ld (%.2.0f%%)",
        thisCorres->count,thisCorres->count/total*100);
printf("\nThe O-lattice size is %e fcc primitive cell \n",
        thisCorres->Osize);

FLAG++;
thisCorres=thisCorres->next;
}
}

void creatCorres() /* allocate memory for a new chain member */
{
    extern struct corres *newCorres;

    newCorres= (struct corres *) malloc(sizeof(struct corres));
    newCorres->next=NULL;
    newCorres->count=0;
    newCorres->Osize=0.0;
}

```

```

float  *nearbcc(fcc) /* find the nearest bcc site for a fcc site */
float *fcc;
{
  extern float lratio;
  float      *bcc,
             displace1=0.,displace2=0.,
             x,y,z,
             tmpx,tmpy,tmpz,
             dx,dy,dz,
             adx,ady,adz;

  bcc=(float *) malloc(sizeof(float)*3);

  /* coordinate transformation */
  x=lratio*(R[0][0]*fcc[0]+R[0][1]*fcc[1]+R[0][2]*fcc[2]);
  y=lratio*(R[1][0]*fcc[0]+R[1][1]*fcc[1]+R[1][2]*fcc[2]);
  z=lratio*(R[2][0]*fcc[0]+R[2][1]*fcc[1]+R[2][2]*fcc[2]);

  tmpx=floor(x+0.5);
  tmpy=floor(y+0.5);
  tmpz=floor(z+0.5);

  dx=x-tmpx;
  if (fabs(dx)<=1.0E-6) adx=0.5;   else adx=dx/fabs(dx)*0.5;
  dy=y-tmpy;
  if (fabs(dy)<=1.0E-6) ady=0.5;   else ady=dy/fabs(dy)*0.5;
  dz=z-tmpz;
  if (fabs(dz)<=1.0E-6) adz=0.5;   else adz=dz/fabs(dz)*0.5;
  displace1=dx*dx+dy*dy+dz*dz;

  dx=tmpx+adx-x;
  dy=tmpy+ady-y;
  dz=tmpz+adz-z;
  displace2=dx*dx+dy*dy+dz*dz;

  if (displace1<displace2) /* take the one with shorter displacement */
  {  bcc[0]=tmpx;          bcc[1]=tmpy;          bcc[2]=tmpz;  }
  else
  {  bcc[0]=adx+tmpx;     bcc[1]=tmpy+ady;     bcc[2]=tmpz+adz;  }

  return(bcc);
}

```

## BMDBMP.ma

**Procedures for deriving 2 lattice correspondences and  
the best matching direction/plane in fcc:bcc oriented  
with a Kurdjumov-Sachs orientation relationship.**

**J.K.Chen, T, MSE, Virginia Tech, Blacksburg, VA, USA  
c1994**

```
<<~/Program/VectorAnalysis.m
```

### ■ Rotation matrix derivation for K-S OR

```
(* lattice parameter = a(fcc) / a(bcc) *)  
r=1.255;  
  
(* bc and fc gives the K-S OR *)  
bc=N[{{1,0,1}/2^.5,{-1,-1,1}/3^.5,{1,-2,-1}/6^.5},10];  
bcc=Transpose[bc];  
  
fc=N[{{1,-1,1}/3^.5,{-1,0,1}/2^.5,{-1,-2,-1}/6^.5},10];  
fcc=Transpose[fc];  
  
(* R= rotation matrix to give K-S OR *)  
R=N[fcc.Inverse[bcc]]  
{0.64983, 0.741582, 0.166667},  
{-0.741582, 0.666667, -0.074915},  
{-0.166667, -0.074915, 0.983163}}  
  
(* iR = inverse of R matrix *)  
iR=Inverse[R];
```

## ■ Derivation of Bain correspondence

```

(* list all possible corresponding directions of the
   basis vectors of bcc in fcc coordinate system.
   These are used to choose the lattice
   correspondence. *)
1/1.255 Transpose[R.Transpose[{{.5,.5,.5},{.5,.5,-.5},
   {.5,-.5,.5},{-.5,.5,.5},{1,0,0},{0,1,0},{0,0,1}}]]
{{0.620748, -0.0596932, 0.295451},
  {0.487946, 2.2116 10-17, -0.487946},
  {0.0298466, -0.590902, 0.355144},
  {0.102956, 0.531208, 0.428253},
  {0.517793, -0.590902, -0.132802},
  {0.590902, 0.531208, -0.0596932},
  {0.132802, -0.0596932, 0.783397}}

(* choose primitive cells by matching closely related
   primitive cells in previous evaluation.
   Note that this set gives a Bain correspondence. *)
(* S2 = Sb *)
Sb=Transpose[{{0,1,0},{.5,.5,.5},{0.5,0.5,-0.5}}];
(* S1 = Sf *)
Sf=r Transpose[{{0.5,0.5,0},{0.5,0,0.5},{0.5,0,-0.5}}]
Sfi=Inverse[Sf];
(* lattice correspondence = S2. (S1)^-1 *)
B=N[Sb.Sfi,10];
MatrixForm[B r]//N
1.    -1.    0.
1.     1.    0.
0.     0.    1.

(* Original primitive cells: both have 1 atom.*)
2*Det[Sb]
4*Det[Sf]/r^3
1.
1.

```

```

(* transformation matrix A *)
A=N[R.B];

(* determinant of (I - A^-1)^-1 *)
OL=Inverse[IdentityMatrix[3]-Inverse[A]];
Det[OL]
27892.4

(* displacement matrix A-I *)
RBI=N[A-IdentityMatrix[3]];
(* representation ellipsoid= (A-I)^T (A-I) *)
misflen=Transpose[RBI].RBI;
(* get the eigenvalues/vectors of the ellipsoid *)
es1=Eigensystem[misflen]

{{0.124119, 0.0220298, 4.81257 10-7},
  {-0.649012, 0.188739, -0.736995},
  {0.0827806, 0.980506, 0.178203},
  {0.756261, 0.0546466, -0.651983}}

(* lambda1 and the misfit of eigenvector
   corresponding to lambda1. *)
lambda1=es1[[1,3]];
Sqrt[lambda1]
0.000693727

(* lambda2 and the misfit of eigenvector
   corresponding to lambda2 or the highest
   misfit the best matching plane suffers. *)
lambda2=es1[[1,2]];
Sqrt[lambda2]
0.148425

(* lambda3 and the misfit of eigenvector
   corresponding to lambda3 *)
lambda3=es1[[1,1]];
Sqrt[lambda3]
0.352305

```

```

(* pick the habit plane normal corresponding to
   the highest eigenvalue (lambda3). *)
BMP=es1[[2,1]];
BMP/=BMP[[2]]
{-3.43867, 1., -3.90483}

(* pick the best matching direction corresponding to
   the lowest eigenvalue (lambda1). *)
BMD=es1[[2,3]];
BMD/=BMD[[3]]
{-1.15994, -0.083816, 1.}

(* the angle between the best matching direction and
   [-1,0,1] direction. The observed growth direction
   is around 5.5 degree from [-1,0,1].*)
Angle[{BMD,{-1,0,1}}]
5.26591

```

## ■ Lattice correspondence II

```

(* The corresponding fcc coordinates of some bcc
   coordinates under K-S OR. *)
1/r Transpose[R.Transpose[{{-1,5,4},
  {3,-1,2}, {.5,.5,.5},{.5,.5,-.5}, {.5,-.5,.5},
  {-.5,.5,.5},{1,0,0},{0,1,0},{0,0,1}}] ]
{{2.96792, 3.00817, 2.96792},
 {1.22808, -2.4233, 1.22808},
 {0.620748, -0.0596932, 0.295451},
 {0.487946, 2.2116 10-17, -0.487946},
 {0.0298466, -0.590902, 0.355144},
 {0.102956, 0.531208, 0.428253},
 {0.517793, -0.590902, -0.132802},
 {0.590902, 0.531208, -0.0596932},
 {0.132802, -0.0596932, 0.783397}}

```

```

(* A different set of unit cells is chosen
   including the possible good matching direction of
   [3,3,3]f vs. [-1,5,4]b. *)

Sb2=Transpose[{{0,1,0},{-0.5,-0.5,0.5},{-1,5,4}}];
Sf2=r Transpose[{{0.5,0.5,0},{-0.5,0,0.5},{3,3,3}}];
Sfi2=Inverse[Sf2];
(* new lattice correspondence II*)
B2=N[Sb2.Sfi2];
MatrixForm[B2*r]
0.666667    -0.666667    -0.333333
0.666667    1.33333    -0.333333
0.333333    -0.333333    1.33333

(* In new unit cells, each contains 3 atoms
   1.5 * 2 atom/bcc cubic cell
   and 0.75*4 atom/fcc cubic cell. *)

2*Det[Sb2]
4*Det[Sf2]/r^3
3.
3.

(* new transformation matrix A2 *)
A2=R.B2;
A2I=A2-IdentityMatrix[3];
(* representation ellipsoid= (A-I)^T (A-I) *)
misf=Transpose[A2I].A2I;
es2=Eigensystem[misf]
{{0.357646, 0.000106069, 0.0000346886},
 {{0.436325, -0.81441, 0.382566},
 {-0.00645645, 0.422329, 0.90642},
 {-0.899766, -0.397964, 0.179014}}}

```

```

(* determinant of (I - A^-1)^-1 *)
OL2=Inverse[IdentityMatrix[3]-Inverse[A2]];
Det[OL2]
27892.4

(* lambda1 and the misfit of eigenvector
   corresponding to lambda1. *)
lambda21=es2[[1,3]];
Sqrt[lambda21]
0.0058897

(* lambda2 and the misfit of eigenvector
   corresponding to lambda2 or the highest
   misfit the best matching plane suffers. *)
lambda22=es2[[1,2]];
Sqrt[lambda22]
0.010299

(* lambda3 and the misfit of eigenvector
   corresponding to lambda3 *)
lambda23=es2[[1,1]];
Sqrt[lambda23]
0.598035

(* pick the habit plane normal corresponding to
   the highest eigenvalue (lambda3). *)
BMP2=es2[[2,1]];
BMP2/=BMP2[[3]]
{1.14052, -2.12881, 1.}

(* angle between the predicted best matching plane
   and the observed (1,-2,1) plane *)
Angle[{BMP2,{1,-2,1}}]
2.18357

```

```
(* pick the best matching direction corresponding to
   the lowest eigenvalue (lambda1).
   This best matching direction is apparently not as
   close to the observed growth direction. *)
BMD2=es2[[2,3]];
BMD2/BMD2[[3]]
{-5.02622, -2.22308, 1.}
```

## ZoneFinder.ma

Inherited from DiffPttGnrl.ma program:

By inputting two least spacing of patterns on the micrograph and the angles between them, the zone axis of the diffraction patterns can be found.

October 28 1993, J. K. Chen, T Group, MSE, Virginia Tech  
Blacksburg, VA, USA, c1993

```
(* Import the facility for vector analysis *)  
<< ~/Program/VectorAnalysis.m
```

### ■ Basic crystal structure input

```
Structure="Beta' - hP* structure";
```

#### □ Atom sites of the crystal structure.

Atom positions follow those used in Pearson's tables  
( CHANGE HERE)

```
(* IMPORTANT ---  
atom point in the unit cell. Note:  
t={ { {x,y,z},{...},... } -> for 1st atom  
  , { {a,b,c},{...}, ... } -> for 2nd atom  
  , { {...},... } , ... }  
*)  
  
t={{ {0,0,0},{2/3,1/3,1/4},{1/3,2/3,0.75}},  
  { {0.65,0.968,0.25},{0.032,0.682,0.25},  
    {0.318,0.35,0.25}, {0.35,0.032,0.75},  
    {0.968,0.318,0.75},{0.682,0.650,0.75}}};  
  
(* If using 4-index hcp system, hex=1, otherwise  
  hex=0. *)  
hex=0;
```

```

(* number of atom type in the current crystal
   structures *)
diffatmno=Dimensions[t][[1]]
2

(* atom= Name of atoms *)
atom={"Ga", "Ag"};

(* Scattering factors for these atoms -
   1. The no. of elements in f should be the same as
      "diffatmno".
   2. The atomic no. of the atoms can be tentatively
      used as their scattering factors, f.
*)
f={31,47};

```

□ The coordinate systems of Bravais unit cells in Cartesian basis.

(CHANGE HERE)

```

(* lattice parameter in Catesian      CHANGE HERE *)
aCart=7.7677 10^-10;
covera=0.28778/0.77677;

(* Input the parameters of crystal structure here:

   lpa, lpb, lpc = lattice parameter of a, b, & c.
   alpha, beta, & gamma in Radian are the angles
   between b & c, a & c, & a & b, respectively.

   lpa, lpb, & lpc are in meter.
*)
lpa=lpb=aCart;
lpc=lpa covera;
alpha=90 Degree;
beta=90 Degree;
gamma=120 Degree;
(* to get coordinates in crystal system from the
   Cartesian coordinates by X(cell) = R.X(Cart) *)
R=ABC[lpa, lpb, lpc, alpha, beta, gamma];

```

```

a=R[[1]];
b=R[[2]];
c=R[[3]];
v=DotProduct[{a,CrossProduct[{b,c}]}];

astar=CrossProduct[{b,c}]/v;
bstar=CrossProduct[{c,a}]/v;
cstar=CrossProduct[{a,b}]/v;

```

□ wavelength = lambda (in m)                      camera length = cameral (in m)

```

(* for Philip EM420 in Virginia Tech
   calibrated with CL reading 660,
   at 120 KV, lambda=0.0396A, cameral=680 mm *)

```

```

lambda=0.0396 10^-10;
cameral=680 10^-3;

```

```

(* Magnification from 1/d to spot spacing *)
cameracnst=cameral lambda ;

```

□ This 'n' is to find all points in one unit cell. 'n' should be larger while the primitive cells are small compared to the unit cells. If the entered crystal structure include all atoms, n=1 is proper. (CHANGE HERE)

```

n=1;

```

□ Find the atoms in one unit cell

```

(* No of translation vectors for different atomic
   types*)
not={};
For[i=1,i<=diffatmno,i++,
  not=Join[not,{Dimensions[t[[i]]][[1]]}]
]
not
{3, 6}

```

```

(* Preparing all lattice points in one unit cell -
   All coordinates have to be smaller than 1. *)
lp=Table[{} , {ii,diffatmno}];
For[i=-n,i<=n,i++,
For[j=-n,j<=n,j++,
For[k=-n,k<=n,k++,
  obase={i,j,k};
  For[l=1,l<=diffatmno,l++,
    base={};
    tmp1p={};
    For[m=1,m<=not[[l]],m++,
      base=Join[base,{obase+t[[l,m]]}];
    ];
    For[m=1,m<=Dimensions[base][[l]],m++,
      If[base[[m,1]]<1. && base[[m,1]]>=0. &&
        base[[m,2]]<1. && base[[m,2]]>=0. &&
        base[[m,3]]<1. && base[[m,3]]>=0.,
        tmp1p=Join[tmp1p,{base[[m]]}];
      ];
    ];
    If[Dimensions[tmp1p][[l]]!=0,
      lp[[l]]=Join[lp[[l]],tmp1p] ];
  ];
];
];
]
(* lp : atoms in one unit cell*)
lp
{{{0, 0, 0}, { $\frac{2}{3}$ ,  $\frac{1}{3}$ ,  $\frac{1}{4}$ }, { $\frac{1}{3}$ ,  $\frac{2}{3}$ , 0.75}},
 {{0.65, 0.968, 0.25}, {0.032, 0.682, 0.25},
 {0.318, 0.35, 0.25}, {0.35, 0.032, 0.75},
 {0.968, 0.318, 0.75}, {0.682, 0.65, 0.75}}}

```

```
(* No. of atoms in one unit cell *)
nop={};
For[i=1,i<=diffatmno,i++,
  nop=Join[nop,{Dimensions[lp[[i]][[1]]}];
]
nop
{3, 6}
```

- Making reciprocal space lattice points within range of  
{{-n1,n1},{-n2,n2},{-n3,n3}}  
( CHANGE HERE )

```
n1=5;
n2=5;
n3=5;
```

- Calculating the scattering of some plane, or the intensity proportion of each reciprocal lattice point.

$$S = \text{Re}(S) + \text{Im}(S) i \quad \text{--} \quad \text{intensity} = S S^* = \text{Re}(S)^2 + \text{Im}(S)^2$$

```

S=0;
diff={};
pi2=2 Pi//N;
For[h=-n1,h<=n1,h++,
  For[k=-n2,k<=n2,k++,
    For[l=-n3,l<=n3,l++,
      Sr=Si=0;
      For[m=1,m<=diffatmno,m++,
        For[p=1,p<=nop[[m]],p++,
          ang=pi2*(h lp[[m,p,1]] + k lp[[m,p,2]] +
            l lp[[m,p,3]])//N;
          Sr+=(f[[m]] Cos[ang])//N;
          Si+=(f[[m]] Sin[ang])//N;
        ];
      ];
      If[Abs[Sr]>1 10^-12 || Abs[Si]>1 10^-12,
        diff=Join[diff,{{h,k,l},Sr^2+Si^2//N}]] ];
    ];
  ];
diff1=diff;

(* No. of rel-points considered *)

```

```

nopatt=Dimensions[diff][[1]]

```

1331

## ■ Data from diffraction pattern and tentative zones

### □ Entering the information from diffraction pattern

1. search1 and search2 have unit in "cm"
2. degree is the angle between search1 and search2
3. degree must be smaller than 180
4. To prevent ambiguity, from search1 to search2 must be in clockwise direction.
5. lenerr is the error allowed for both search1 and search2
6. degerr is the error allowed for the angle.

```
search1=1.2;  
search2=1.15;  
degree=90;  
lenerr=0.10;  
degerr=1;
```

```
General::spell1:
```

```
Possible spelling error: new symbol name "degree"  
is similar to existing symbol "Degree".
```

```
(* spaing between (0,0,0) and (x,y,z) diffraction  
spot *)  
len[{x_,y_,z_}]:=Block[{relx,normpatt},  
relx=Rel[{x,y,z}];  
normpatt=Norm[relx] cameracnst*100;  
Return[normpatt];  
];
```

```

tendir1={};
tendir2={};
low1=search1*(1-lenerr);
high1=search1*(1+lenerr);
low2=search2*(1-lenerr);
high2=search2*(1+lenerr);
(* pick out those directions that match the entered
   spot spacing. *)
For[i=1,i<=nopatt,i++,
  tenlen=len[diff[[i,1]]];
  If[tenlen < high1 && tenlen>low1,
    tendir1=Join[tendir1,{Rel[diff[[i,1]]]}];
  If[tenlen < high2 && tenlen>low2,
    tendir2=Join[tendir2,{Rel[diff[[i,1]]]}];
]
nodir1=Length[tendir1]
nodir2=Length[tendir2]
30
42

lowang=degree-degerr;
highang=degree+degerr;
tenzone={};
(* From those spots that have the right distances,
   the ones that have correct angles are found. *)
For[i=1,i<=nodir1,i++,
  For[j=1,j<=nodir2,j++,
    angle=Angle[{tendir1[[i]],tendir2[[j]]}]/N;
    If[Abs[Im[angle]]<10^-4, angle=Re[angle]];
    If[angle>lowang && angle<highang,
      tenzone=Join[tenzone,
        {CrossProduct[{tendir1[[i]],tendir2[[j]]}]}];
  ];
];
] ;
coord=Transpose[{a,b,c}];
icoord=Inverse[coord];
(* New tenzone will be suitable for input as zonaxis.
  *)

```

```

tenzone2={};
  nozone=Length[tenzone];
If[nozone==0,Print["No zones fit"],
  tenzone=Transpose[icoord.Transpose[tenzone]];
If[hex==1,
  For[i =1, i<=nozone,i++,
    tenzone2=Join[tenzone2,
      {UnHexAxis[tenzone[[i]]}]]; ],
  tenzone2={};
  For[i=1,i<=nozone, i++,
    scale=Floor[Log[10,Max[Abs[tenzone[[i]]]]]];
    AppendTo[ tenzone2,tenzone[[i]]/10^scale]
  ]
];
(* Tentative Zone Axes
  Note:
  the zone axes may be floating points numbers.
  You can try to devide them by the largest common
  factor. *)
Print[tenzone2]//N
];

```

```

-16
{{2.8314 10-16, -1.99501, -3.99002},
{-1.99501, -1.99501, 3.99002},
{1.99501, 1.99501, 3.99002},
{-1.99501, -1.99501, -3.99002},
{1.99501, 1.99501, -3.99002},

-32
{-1.99501, 2.10285 10-32, 3.99002},

-32
{1.99501, -2.10285 10-32, -3.99002},

-32
{1.99501, 2.10285 10-32, 3.99002},

-32
{-1.99501, -2.10285 10-32, -3.99002},

.....

```

**NOTE:** some other solutions have been truncated. Most of them are equivalent which is inevitable due to the symmetry of the crystal structures. A simple observation can find that the indexed zones are [0,-1,-2], [1,1,2], [1,0,2], etc. They are actually all equivalent since the structure is hexagonal.

In some cases, if “No zones fit” were given as the answer, it would indicate that there are no zones that fit into the entered parameters. The tolerance angle or spot distances may need some changes, or the considered crystal structure does not give such diffraction pattern.

■ Check a specific zone

(do not require to run the “Data from diffraction pattern and tentative zones” first.)

- Diffraction pattern of zone axis to be calculated. (in Bravais coord. system)  
(CHANGE HERE)

```
(* If hexagonal structure. Note:
```

```
  zoneaxis={h,k,l,m}
```

```
  zone=Axis[HexAxis[zoneaxis]]
```

```
Otherwise:
```

```
  zoneaxis={x,y,z}
```

```
  zone=Axis[zoneaxis]
```

```
*)
```

```
If[hex==1,
```

```
  zoneaxis={4,-2,-2,-3};
```

```
  zone=Axis[HexAxis[zoneaxis]] ;,
```

```
(* Enter the zone axis here    CHANGE HERE*)
```

```
  zoneaxis={1,0,2};
```

```
  zone=Axis[zoneaxis];
```

```
]
```

```
zoneaxis
```

```
{1, 0, 2}
```

- Pull out all those possible plane to be diffracted by the assumption that the angles between zone axis and rel-points are 90 degree.

```

maxdiff=0;
showpatt={};
For[i=1,i<=nopatt,i++,
  relpatt=Rel[diff[[i,1]]];
  OnEwalk=DotProduct[{relpatt,zone}]/N;
  (* Print[OnEwalk//N]; *)
  If[Abs[OnEwalk]<1.0 10^-8,
    If[maxdiff<diff[[i,2]],maxdiff=diff[[i,2]];
    showpatt=Join[showpatt,{{diff[[i,1]],
      diff[[i,2]]}}] ]
]

(* No. of shown pattern spots. *)
noshpatt=Dimensions[showpatt][[1]]
55

```

- Projecting patterns into two-dimension by using the first rel-point listed after the transmitted beam as X-axis.

```

x=showpatt[[Floor[(noshpatt+1)/2]+1]];
xstar=UnitVector[Rel[x[[1]]]]/N
{0, 1., -7.07027 10^-17}

ystar=CrossProduct[{UnitVector[zone],xstar}]/N
{-0.595344, 5.68075 10^-17, 0.803471}

```

□ Mapping the diffraction into 2D plots

```

dotsize=0.03;
pattpos={};
nomidpatt=Floor[(noshpatt+1)/2]+1;
For[i=1,i<=noshpatt,i++,
  patt=showpatt[[i,1]];
  pattstar=Rel[patt];
  normpatt=Norm[pattstar];
  (* 1/d(hkl) *)
  theta=ArcSin[normpatt lambda/2] //N;
  If[theta==0,
    pattpos=Join[pattpos,
      {GrayLevel[0],
      PointSize[0.01+dotsize*
        Abs[showpatt[[i,2]]/maxdiff]],
      Point[{0,0}],
      GrayLevel[1.0],
      PointSize[0.8 dotsize],
      Point[{0,0}], GrayLevel[0.0]}],
    projdir=UnitVector[CrossProduct[{zone,
      CrossProduct[{pattstar,zone}]}]] //N;
    ptcoord=normpatt cameracnst projdir//N;
    (* projection of x and y on the relative
      patterns *)
    xproj=DotProduct[{ptcoord,xstar}]/N;
    yproj=DotProduct[{ptcoord,ystar}]/N;
    pattpos=Join[pattpos,
      {
        (*GrayLevel[
          0.8(1.0-Abs[showpatt[[i,2]]/maxdiff))],*)
        PointSize[0.01+dotsize*Abs[showpatt[[i,2]]/
          maxdiff]],
        Point[{xproj,yproj}] ,
        Text[FontForm[
          StringForm["(\\`\\`\\`\\`)",
            patt[[1]],patt[[2]],patt[[3]]],
          { "Plain",8} ],
          {xproj,yproj},{0,3}]]];
  ];

```

```

    If[i==nomidpatt,midpatt={StringForm["(\\ \\ \\ \\ \\ \\)",
      patt[[1]],patt[[2]],patt[[3]]],100 xproj}}];
]

Print[StringForm[
  "Lambda = ``m      camera Length = `` m",
  lambda,cameral//N]];
Print[Structure, StringForm[" : `` Pattern ",
  zoneaxis]]
Print[StringForm[
  "Lattice Parameters (a, b, & c) = ``, ``,
  and `` A", 10^10 lpa,10^10 lpb,10^10 lpc]];
Print[StringForm[
  "Alpha, Beta, and Gamma = ``, ``, and `` Degree",
  alpha/Degree,beta/Degree,gamma/Degree]];
Print[StringForm["Spacing at `` = `` cm",
  midpatt[[1]],midpatt[[2]]]];
Print[" "];
For[i=1, i<=diffatmno, i++,
  Print[StringForm["Atom#`` - ``, f = ``",
    i,atom[[i]],f[[i]]]];
  Print["      at ", lp[[i]]];
  Print["      "];
]
pattern=Show[Graphics[patttpos],
  Frame->False,AspectRatio->Automatic];

```

-12

Lambda = 3.96 10 m camera Length = 0.68 m  
Beta' - hP\* structure : {1, 0, 2} Pattern  
Lattice Parameters (a, b, & c) = 7.7677, 7.7677, and  
2.8778 A  
Alpha, Beta, and Gamma = 90, 90, and 120 Degree  
Spacing at (010) = 0.400296 cm

Atom#1 - Ga, f = 31

	2	1	1	1	2
at	{0, 0, 0},	{-, -, -},	{-, -, 0.75}}		
	3	3	4	3	3

Atom#2 - Ag, f = 47

at {{0.65, 0.968, 0.25}, {0.032, 0.682, 0.25},  
{0.318, 0.35, 0.25}, {0.35, 0.032, 0.75},  
{0.968, 0.318, 0.75}, {0.682, 0.65, 0.75}}

• • • • •  
-4-520-4-420-4-320-4-220-4-120-402)(-412)(-422)(-432)(-442)(-452)

• • • • •  
(-2-510-2-410-2-310-2-210-2-110-201)(-211)(-221)(-231)(-241)(-251)

• • • • •  
(0-50)(0-40)(0-30)(0-20)(0-10) (010) (020) (030) (040) (050)

• • • • •  
(2-5-102-4-102-3-102-2-102-1-1020-1)(21-1)(22-1)(23-1)(24-1)(25-1)

• • • • •  
2 3 4 5 6 7 8 9 10 11 12 13 14 15 16 17 18 19 20 21 22 23 24 25 26 27 28 29 30 31 32 33 34 35 36 37 38 39 40 41 42 43 44 45 46 47 48 49 50

## ■ Final checks

(\* Here is the entered data:

```
search1=1.2;
search2=1.15;
degree=90;
```

By comparing with the SADP, search1 is corresponding to (0,3,0), search2 is to (-2,1,1), and degree corresponds to the angle between search1 and search2.

\*)

```
len[{0,3,0}]
```

(\* gives the spot distance of (0,3,0) and should compare with search1. \*)

1.20089

```
len[{-2,1,1}]
```

(\* gives the spot distance of (-2,1,1) and should compare with search1 \*)

1.16459

```
Angrel[{{0,3,0},{-2,1,1}}]
```

(\* gives the angle between (0,3,0) and (-2,1,1) spots and should compare with degree. \*)

90.

## VITA

Mr. Jhewn-Kuang Chen was born in August, 1967 in Taipei, Taiwan. After graduating from Mining and Metallurgical Engineering Department, National Taipei Institute of Technology in 1987, he passed the National Higher Civil Service Examination held by the government in the same year. He was a project design engineer in the Foundry of Taiwan Machinery Manufacturing Company from 1989 to 1990 after his two-year service in R.O.C. Army where he worked as a computer programmer. He came to Virginia Polytechnic Institute and State University in 1990 and started on his master of science degree in Department of Materials Science and Engineering under direction of Prof. W. T. Reynolds Jr. His M.S. thesis investigated the alloying effects on the kinetics of austenite decomposition in high strength low alloy steels and was finished in October, 1992. He then pursued his doctor of philosophy degree in the same institute with Prof. Reynolds and studied the atomic matching and interfacial structures during solid-solid phase transformations. He finished his PhD dissertation in September, 1995. His research interests include characterization of processing, structures and properties of solid-solid interfaces and mathematical analyses using computer modelling in materials science and engineering.

